NTNU – Trondheim
Norwegian University of
Science and Technology

Aeroelastic stability of a suspension bridge crossing the Sognefjord

Håvard Røe Maurset

Civil and Environmental Engineering
Submission date: June 2012
Supervisor: Ole Andre Øiseth, KT
Co-supervisor: Kristian berntsen, Statens vegvesen
Anders Rönnquist, KT
Ragnar Sigbjörnsson, KT

Norwegian University of Science and Technology
Department of Structural Engineering

Department of Structural Engineering
Faculty of Engineering Science and Technology
NTNU- Norwegian University of Science and Technology

ACCESSIBILITY

MASTER THESIS 2012

SUBJECT AREA: Bridge dynamics, Aeroelastic stability	DATE: 11.06.2012	NO. OF PAGES: 116

TITLE:

Aeroelastic stability of a suspension bridge crossing the Sognefjord

Aeroelastisk stabilitet av en hengebro over Sognefjorden

BY:

Håvard Røe Maurset

SUMMARY:
This thesis discusses the possibility of constructing a suspension bridge crossing the Sognefjord in light of the aeroelastic stability. A preliminary design has been carried out and a finite element model created in order to extract natural frequencies and mode shapes. The stability limit has been assessed by the use of a multimodal approach and a simplified solution using well-known flutter equations.
The multimodal eigenvalue solution shows that the shape-wise similarity is a clear indicator of which modes contributing most to the stability limit, when the governing instability is multimodal flutter. Multimodal effects have also shown to have both a stabilizing and destabilizing effect, and are related to the shape-wise similarity. In this thesis the stability limit is assessed using different cross sectional configurations, consisting of separated box-girders. It is concluded that central barriers and guide vanes provides critical velocities well above the design critical velocity. It is also shown that the stability limit increases significantly when increasing the distance between the girders. One configuration has shown a static instability phenomenon called static divergence. It is found that one torsional mode contributes significantly to this instability, but where other torsional modes also contribute.
In this thesis the aerodynamics of the different cross sectional configurations are accounted for by modelling the self-exited forces with the use of aerodynamic derivatives. Uncertainties in curve fitting have been discussed, and it is concluded that in the vicinity of the critical design velocity chosen polynomials can be used with adequate accuracy. From this it has been concluded that any instability below the critical design velocity are of no concern for the tested configurations.
In this thesis well-known flutter equations are used to assess the flutter stability limit as a function of the shape-wise similarity and the frequency ratio and results show that a high shape-wise similarity combined with a low frequency ratio gives the lowest critical velocity. The flutter solution has also been compared to the multimode solution and it is concluded that the flutter solution provides an engineering approximation of the flutter stability by providing conservative results.

RESPONSIBLE TEACHER: Ole Andre Øiseth

SUPERVISOR(S): Ragnar Sigjörnsson (NTNU), Anders Rönnquist (NTNU), Kristian Berntsen (SVV)

CARRIED OUT AT: Department of Structural Engeneering

NTNU
Institutt for konstruksjonsteknikk

Masteroppgave våren 2012 for stud. techn. Håvard Maurset:

Aeroelastisk stabilitet av hengebro over Sognefjorden

Aeroelastic stability of a suspension bridge crossing Sognefjorden

Statens vegvesen planlegger en ombygning av E39 slik at det blir mulig å reise fra Trondheim til Kristiansand ferjefritt. Dette innebærer at det skal bygges en rekke brokonstruksjoner. En av disse bruene vil krysse Sognefjorden. Denne oppgaven dreier seg om hengebroalternativet.

Oppgavens formål er å:

- Utføre overslagsdimensjonering av en hengebro over Sognefjorden
- Bestemme den aeroelastiske stabilitetsgrensen.

Løsningen av oppgaven bør inneholde følgende

- Valg av tverrsnittsform og søk i litteraturen etter lastkoeffisienter og aerodynamiske deriverte.
- Overslagsdimensjonering av konstruksjonen.
- Etablering av en Abaqus modell
- Bestemmelse av egenfrekvenser og svingeformer
- Beregning av aeroelastisk stabilitetsgrense

Oppgaven skal utføres i henhold til retningslinjer for utførelse av prosjektoppgave ved Institutt for konstruksjonsteknikk (se Instituttets hjemmeside).

Faglærer: Ole Andre Øiseth (NTNU)

Veiledere: Ragnar Sigbjörnsson (NTNU), Anders Rönnquist (NTNU) og Kristian Berntsen (SVV)

Besvarelsen skal leveres til Institutt for konstruksjonsteknikk innen 11. juni 2012.

Ole Andre Øiseth
Faglærer

Preface

This master thesis is the final part of the Master degree at the Norwegian University of Science and technology (NTNU), Trondheim, Norway. The thesis has been carried out at the Faculty of Engineering Science and Technology, Department of Structural Engineering. The thesis is written in cooperation with the Norwegian Public Roads Administration under supervision of Kristian Berntsen. The supervisors at NTNU have been Associate Professor Ole Øiseth, Associate Professor Anders Rönnquist and Professor Ragnar Sigbjörnsson.

The thesis has consisted in collecting knowledge about the design process of suspension bridges, searching literature for the relevant theory for calculating the aeroelastic stability limit of suspension bridges and a great amount of finite element simulations as well as numerical calculations.

The thesis consists of the following objectives;

- A literature search to find a cross section where aerodynamic derivatives are experimentally obtained.
- Carry out a preliminary design for a suspension bridge crossing the Sognefjord
- Creating a finite element model of the bridge based on the preliminary design
- Finding undamped natural frequencies and corresponding mode shapes
- Calculation of the aeroelastic stability limit

The author wishes to express sincere thanks and appreciation to all supervisors for all guidance and information during this work. They have provided me with relevant and helpful information when problems have occurred. I wish to thank my head supervisor Ole Øiseth for all help with the simulations, and for providing the relevant numerical routines for solving the relevant problems. I also wish to thank Kristian Berntsen for answering all the questions regarding relevant Handbooks and the Eurocode.

Trondheim, June 11, 2012

Håvard Maurset

Abstract

This thesis discusses the possibility of constructing a suspension bridge crossing the Sognefjord in light of the aeroelastic stability. The bridge will have a main span of 3,700 m and must withstand a critical design wind speed of 63.3 m/s. A preliminary design has been carried out, and constitutes the foundation for creating a finite element model of the bridge. Based on natural frequencies and mode shapes the stability limit has been assessed by the use of a multimodal approach and a simplified solution using well-known flutter equations.

A few investigations have been carried out, changing the boundary conditions and the geometry of the backstay cables. It is concluded that the change in stability limit is insignificant when changing the boundary conditions. Changing the backstay geometry changes the stability limit by a few per cent, but is considered small compared to the importance of changing the aerodynamics of the cross section.

An attempt of solving the complex eigenvalue problem for a multimodal approach has been made. The solution routine has shown good results when few modes are included in the calculations, compared to a solution provided, but need further modifications especially when several modes are included. The eigenvalue solution shows that the shape-wise similarity is a clear indicator of which modes contributing most to the stability limit, when the governing instability is multimodal flutter. When several torsional modes are shape-wise similar to one vertical and the frequencies not well separated, it has been shown that it is not necessarily the torsional mode with the lowest frequency that will provide the lowest flutter stability limit. The degree of coupling between torsional and horizontal motion in a mode is suspected to influence the results. Multimodal effects have also shown to have both a stabilizing and destabilizing effect, and are related to the shape-wise similarity.

In this thesis the stability limit is assessed using different cross sectional configurations, consisting of separated box-girders. They are different by the aerodynamic devices mounted to the cross section, and the distance between the girders. It is concluded that central barriers and guide vanes provides critical velocities well above the design critical velocity. It is also shown that the stability limit increases significantly when increasing the distance between the girders. A cross section has been tested for a configuration without guide vanes and compared with the same configuration with guide vanes, and it is concluded that guide vanes has a significantly positive effect on the stability limit. One configuration has shown a static instability phenomenon called static divergence. It is found that one torsional mode contributes significantly to this instability, but where

several other torsional modes also contribute.

Simplified expressions from the quasi-steady theory are sometimes used to model the self-exited forces on the stiffening girder. In this thesis the aerodynamics of the different cross sectional configurations are accounted for by modelling the self-exited forces with the use of aerodynamic derivatives. Polynomials have been fitted to experimental data and the curves show acceptable results within the data range, at least for the most important derivatives. The bridge presented has shown reduced velocities that are high compared to the data range from where the aerodynamic derivatives are given. The aerodynamic derivatives have been extrapolated outside the data range from experiments, giving results of considerably uncertain reliability. These uncertainties have been discussed, and it is concluded that in the vicinity of the critical design velocity the chosen polynomials can be used with adequate accuracy. From this it has been concluded that any instability below the critical design velocity are of no concern for the tested configurations.

This thesis uses the well-known flutter equations in assessing the flutter stability limit as a function of the shape-wise similarity and the frequency ratio between one vertical and one torsional mode, at the same time accounting for aerodynamics by the use of aerodynamic derivatives. The flutter solution are tested on the different cross sectional configurations and results show that a high shape-wise similarity combined with a low frequency ratio gives the lowest critical velocity. The flutter solution has also been compared to the multimode solution and it is concluded that the flutter solution provides an engineering approximation of the flutter stability by providing conservative results.

Sammendrag

Denne oppgaven diskuterer mulighetene for å bygge en hengebru over Sognefjorden i lys av stabiliteten under høye vindhastigheter. Bruen vil få et hovedspenn på 3,700 m og må motstå en dimensjonerende kritisk vindhastighet på 63.3 m/s. En overslagsdimensjonering har blitt utført og utgjør grunnlaget for å lage en modell av bruen i et elementmetode program. Stabilitetsgrensen har blitt vurdert ut ifra svingemoder og tilhørende egenfrekvenser ved bruk av en multimodal løsning og en forenklet løsning som benytter kjente flutter ligninger.

Noen få undersøkelser har blitt utført, der ulike opplagerbetingelser for brubjelken og forskjellig geometri av sidespennet har blitt endret på. Resultatene viser at opplagerbetingelsene har liten effekt på stabilitetsgrensen. På den andre siden viser resultater at ved å øke lengden på sidespennet reduseres den kritiske vindhastigheten med opptil noen få prosent. Disse endringen har blitt vurdert ubetydelige i forhold til å endre de aerodynamiske egenskapene til brubjelken.

Et forsøk på å løse det komplekse egenverdiproblemet har blitt utført. Resultater viser at løsningsrutinen gir samme verdier som en tildelt løsningsrutine, når løsningen inkluderer få svingemode. Når flere svingemoder er inkludert viser løsningsrutinen tydelig instabiliteter og modifiseringer trengs. Egenverdiløsningen viser at formlikheten av svingemodene er en klar indikasjon på hvilke moder som bidrar mest til instabiliteter, når det styrende instabilitetsfenomenet er multimodal flutter. Når flere torsjonsmoder er formlike med en vertikal mode, og frekvensene av torsjonsmodene er lite separert, viser resultatene at det nødvendigvis ikke er torsjonsmoden med den laveste frekvensen som bidrar med den laveste stabilitetsgrensen. Graden av kopling mellom horisontale forskyvninger og torsjonsforskyvninger kan ha en innflytelse på resultatene. Resultater viser at multimodale effekter kan både ha stabiliserende eller destabiliserende innflytelse for den kritiske vindhastigheten, og er relatert til formlikheten av modene.

I denne oppgaven har stabilitetsgrensen blitt vurdert ved bruk av forskjellige tverrsnitt for brubjelken som alle består av to parallelle såkalte boks tverrsnitt. Et tverrsnitt har blitt testet både med og uten såkalte ledeskovler, og det er konkludert med at ledeskovler gir en betydelig økning i stabilitetsgrensen. Økt avstand mellom boks tverrsnittene viser også at stabilitetsgrensen øker ved at de aerodynamiske egenskapene blir forbedret. Et av tverrsnittene har vist et instabilitetsfenomen kalt statisk divergens. Resultater viser at det er spesielt en torsjonsmode som bidrar til denne instabiliteten, men hvor flere torsjonsmoder bidrar til en viss grad.

Forenklede uttrykk fra kvasi-statisk teori er noen ganger brukt til å beskrive de selv-

eksiterende kreftene på brubjelken. I denne oppgaven har disse kreftene blitt beskrevet av såkalte aerodynamiske deriverte. Kurver av polynom har blitt tilpasset eksperimentelle data, og kurvene gir akseptable resultater innenfor rekkevidden av dataene, spesielt for de viktigeste deriverte. Den presenterte bruen har vist høye reduserte vindhastigheter i forhold til de verdier som er gitt av eksperimentene. Verdiene av de deriverte har derfor blitt ekstrapolert utenfor rekkevidden til dataene, og dette reduserer påliteligheten av resultatene. Disse usikkerhetene har blitt diskutert og det er konkludert med at i området rundt den dimensjonerende kritiske vindhastigheten kan de tilpassede kurvene brukes med en tilfredsstillende nøyaktighet. På bakgrunn av dette kan det konkluderes med at instabiliteter under den dimensjonerende kritiske vindhastigheten ikke vil finne sted med de alternativene for brubjelken som har blitt presentert.

I denne oppgaven har de kjente flutterligningene blitt brukt til å estimere stabilitetsgrensen som funksjon av formlikheten og frekvensforholdet mellom en vertikal og en torsjonsmode, og i tillegg har de aerodynamiske egenskapene blitt tatt i betraktning ved bruk av de aerodynamiske deriverte. Flere tverrsnitt har blitt vurdert og resultater viser at en kombinasjon av høy formlikhet og et lavt frekvensforhold gir den laveste kritiske vindhastigheten. Flutterløsningen har også blitt sammenlignet med den multimodale løsningen og det er konkludert med at flutterløsningen gir konservative resultater sett fra et ingeniørmessig perspektiv.

Contents

List of Figures

List of Tables

Chapter 1

Introduction

As part of a project called Costal Highway E39, the Norwegian Public Roads Administration (NPRA) has been commissioned to investigate the possibility for eliminating all ferries along the western corridor (E39). This includes the technological aspects of crossing fjords spanning over large distances. The longest fjord crossing in this project will be the crossing of the Sognefjord. The Sognefjord is considered the most challenging because of the overall vast depths up to 1,300 m, and will be a pilot project in developing new concepts for extreme bridges. Three main alternatives are under evaluation, and one of them is a suspension bridge spanning the entire width of the fjord. The fjord is about 3.7 km wide, indicating that this bridge would be the worlds longest suspension bridge. If the bridge is to be constructed it will span over the fjord somewhere in the area between Lavik and Oppedal where the existing ferry has its route. The 10-min design wind speed for the actual location is found to be 39.6 m/s corresponding to a return period of 50 years. A suspension bridge crossing the Sognefjord has been the subject of this thesis.

Based on the topographical conditions mentioned above a preliminary design of a suspension bridge has been carried out based on a cross section given in the literature, which constitutes the foundation necessary for creating a finite element model of the bridge. The finite element model is used to carry out an eigenvalue analysis for extracting still air natural frequencies and corresponding mode shapes. The natural frequencies are analyzed, and several configurations have been tested in order to understand how parameters change the results.

Recent investigations have shown that aeroelastic considerations, and not only the aerodynamics related to the cross section is of importance in assessing the stability limit. As mentioned in Miyata [16], considerations of bridge response are related to the interaction of aero- and elastic characteristics of the structure. It may be said that the aerodynamics are related to the cross sectional configuration while the aeroelastic stability refers to the whole structure as a 3D problem. In this thesis some aeroelastic investigations have been carried out but the main focus have been on the aerodynamic characteristics of different cross sectional configurations.

One of the most important tasks when designing long-span bridges is to avoid devastating oscillations du to strong wind. Self-exited forces cause these oscillations from interaction between the structure and the wind flow, which affects the structural properties by changing the total stiffness and damping of the structure. Examples of such phenomenon are flutter, static divergence, galloping and dynamic instability in torsion. Flutter is in most cases the most critical where a vertical and torsional vibration mode couples into

one motion with the same oscillating frequency. This phenomenon may cause structural failure, as was the reality of the famous Tacoma Narrow Bridge collapse in 1940. Static divergence, as the name indicates, is a static stability problem where the torsional stiffness equals zero due to interaction with the airflow. Galloping and dynamic stability in torsion are both identified as single mode oscillation in vertical and torsional directions respectively. The flutter phenomenon has been subject to a lot of research resent years, and the understanding of multimodal flutter effects has become more important where several still air vibration modes contributes to the stability limit, see for instance [1, 2, 15, 26]. These multimodal effects may have a stabilizing or destabilizing effect on the stability. Two well-known factors that influencing which modes that couples into a multimodal motion are the shape-wise similarity and the frequency ratio between vertical and torsional modes. Usually it is the fundamental vertical and torsional modes that will couple into a flutter motion, but as it has been mentioned in Mishra et al. [15] this is not always the case , see also [9]. The different aspects mentioned above has been subject for discussion in this thesis, and are analyzed by solving the multimodal complex eigenvalue problem, see for instance [15, 28]

Simplified methods for predicting the flutter stability limit are still considered important today, even if more accurate methods has been developed in the recent years. Selberg's formula [32] is still widely used in preliminary designs as an estimation for the flutter stability of a bimodal system, but the formula is limited to cross sections having a shape similar to that of a thin airfoil. The mode shapes are also assumed perfectly similar. In this thesis the well known flutter equations [8, 35] are used to predict the flutter stability limit for a range of different cross sectional configurations and compared with the multimodal approach mentioned above. This method provides a stability limit of a bimodal system consisting of two still-air vibration modes, as a function of the frequency ratio and the shape-wise similarity of the modes.

The complex eigenvalue solution and the flutter equations are both based on a modal superposition approach where the modes are introduced as generalized degrees of freedom. The structural displacements, representing a 3 degree of freedom system, are represented by the sum of the products between the natural mode shapes $\boldsymbol{\varphi}_i$ and corresponding generalized coordinates η_i. The self-exited forces associated with the structural displacements can be written as follows[29, 35] ;

$$
\begin{aligned}
q_{y,se} &= \frac{1}{2}\rho V^2 B\left(KP_1^*\frac{\dot{r}_y}{V} + KP_2^*\frac{B\dot{r}_\theta}{V} + K^2P_3^*r_\theta + K^2P_4^*\frac{r_y}{B} + KP_5^*\frac{\dot{r}_z}{V} + K^2P_6^*\frac{r_z}{B}\right)\\
q_{z,se} &= \frac{1}{2}\rho V^2 B\left(KH_1^*\frac{\dot{r}_z}{V} + KH_2^*\frac{B\dot{r}_\theta}{V} + K^2H_3^*r_\theta + K^2H_4^*\frac{r_z}{B} + KH_5^*\frac{\dot{r}_y}{V} + K^2H_6^*\frac{r_y}{B}\right)\\
q_{\theta,se} &= \frac{1}{2}\rho V^2 B^2\left(KA_1^*\frac{\dot{r}_z}{V} + KA_2^*\frac{B\dot{r}_\theta}{V} + K^2A_3^*r_\theta + K^2A_4^*\frac{r_z}{B} + KA_5^*\frac{\dot{r}_y}{V} + K^2A_6^*\frac{r_y}{B}\right)
\end{aligned}
\tag{1.1}
$$

Here, $P_n^*, H_n^*, A_n^*, n \in \{1, 2, ..., 6\}$ are dimensionless aerodynamic derivatives dependent on the cross sectional shape and are functions of the reduced velocity. V is the mean wind

velocity, ρ is the density of air, B is the width of the girder, $K = B\omega/V$ is the reduced frequency and r_n, $n \in \{y, z, \theta\}$ are the structural displacements. In most cases the terms associated with the lateral motion, r_y and $\dot{r}_y$, are disregarded or taken from the quasi-steady theory. In this thesis these terms have been neglected, meaning that the system is reduced to a two-dimensional system with vertical displacement r_z and angular rotation r_θ. The importance of the lateral contribution has not been paid attention to in this thesis but indications may suggest that it has a positive effect on the stability limit [1]. Throughout this thesis experimentally obtain values for the aerodynamic derivatives have been used, but one study has been carried out where quasi-steady values for aerodynamic derivatives associated with lateral motion is introduced.

Chapter 2

Suspension bridges

Suspension bridges are part of the family of cables supported bridges, distinguished by their ability to span over long distances. The main difference of cable-supported bridges is the configuration of the cable system. In suspension bridges the cables are suspended with vertical (may be inclined) hangers connecting the stiffening girder to the main cables. Cable-stayed bridges are another type of cable-supported bridge where the cable system contains straight cables connecting the stiffening girder to the pylons. A combination between different types of bridges is also possible. Suspension bridges are the slenderest of all bridges, and dominate the type of bridge used for long spans. From the first suspension bridge that were built and until today, engineers have competed in building the longest bridges with further decreasing slenderness ratio (depth-to-span ratio). The trend of increasing slenderness may be said to reach a limit when the famous Tacoma Narrow Bridge, opened in 1940, collapsed. The bridge experienced a combined torsional and vertical motion, caused by interaction between the girder and the wind flow. After some time the torsional motion became severe with a tilting of the girder up to $\pm 45^o$. Negative damping caused these self-exited oscillations. The bridge had only been accounted for static pressure due to wind, and the dynamics related to interactions between the wind and the girder had not been considered [10]. After this disaster aerodynamics became important in the design process for bridges to be built and for all existing suspension bridges. The construction of the longest and slenderest ever-built suspension bridge in Norway is about to finish within 2013. The bridge will be one of the longest (nr. 9 when completed) and slenderest suspension bridges in the world with a total span of 1,380 m and a main span length of 1,310 m [38]. Figure 2.1 shows the main components of a suspension bridge, and they will be presented shortly in the following.

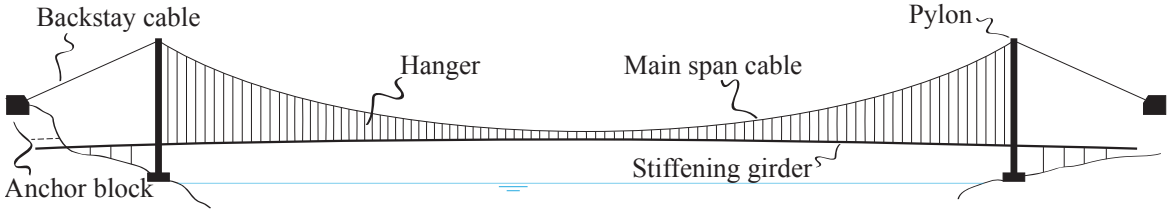

Figure 2.1: Main components of a suspension bridge

2.1 Stiffening girder

The stiffening girder is the structural element of the suspension bridge subjected to most of the external loading. The girder must locally be able to resist the forces due to e.g. traffic loads and interaction between the girder and the wind flow, referred to as aerodynamics. Globally the cable system assists the girder in transferring the loading to the supporting points. Whether the girder is in steel or concrete the weight, cost, stiffness properties and the aerodynamics are all considerations of great importance. The shape of the stiffening girder has been subject to a lot of research and testing during the years, especially after the Tacoma Narrow collapse. As suspension bridges become longer the aerodynamic has become more important in addition to maintain the torsional stiffness as the girders becomes more slender. The most common configuration of long-span bridges today is closed box-girders of steel with trapezoidal shaped stiffeners inside the box and braced bulkheads at intermediate distance. Such a configuration is also favourable when considering corrosion and maintenance as well as the dead loads are considerably lower compared to girders of concrete. One example of such a configuration is the Great Belt Bridge in Denmark with a main span of 1,624 m. Girders of stiffening trusses are also widely used, examples are the Golden Gate Bridge and the worlds longest suspension bridge located in Japan, the Akashi-Kaikyö Bridge with a main span of 1,991 m [10]. From an aerodynamic point of view box-girders with edge fairings has proven to be favourable because the drag force is reduced. In resent years a twin box configuration has also proven to give increased stability during strong wind, especially together with guide vanes and other aerodynamic devices mounted on the girders. The box-girders in such a configuration are connected by crossbeams at intermediate distance, and the distance between the box-girders may be increased which also has been proven to give favourable effects [11, 14, 24, 30, 31]. Figure 2.2 gives an illustration of such a configuration where guide vanes has been mounted at the lower outer edge of the girder [11].

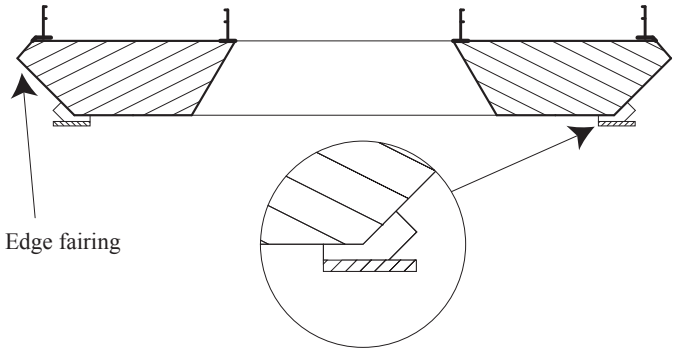

Figure 2.2: Twin box configuration with guide vanes and edge fairings as aerodynamic improving configurations.

2.2 Cables

The cables in cable supported bridges are characterized by the considerably larger tensile strength compared to ordinary steel. This reduces the amount of steel needed to carry the load acting on a bridge. The cables are made by small steel wires, usually of cylindrical shape with a diameter between 3 and 7 mm [10]. As the cables consist of several, maybe thousand of small wires, the bending stiffness of the cables is practically zero, which means that all loading must be transferred as tension through the cables. In suspension bridges the cables are used to carry the vertical load from traffic, dead load and other concentrated loading by vertical hangers transferring the load to the cables as tension forces. The load on a cable can be compared with a simply supported beam subjected to distributed load, where the moments in the beam for the given load is equal to the horizontal force in the cable times the sag. I.e. the horizontal cable force is inversely proportional to the sag meaning that the maximum tension in the cables will be larger as the sag decreases. The choice of sag is based on economical as well as performance aspects as larger sag will reduce the required cable area, but will increase the pylon height.

2.3 Hangers

The distributed load that acts on the stiffening girder has to be transferred through the hangers and to the cables. As for the cables the hangers transfers the load as tension and are placed with a certain distance between each other depending on the girder configuration, dead load of the girder and all additional loading.

2.4 Pylons

In suspension bridges the main purpose of the towers is to transfer the vertical forces from the cables down to the ground. Since the forces in the pylons mainly are compressive forces, and the cable system stabilizes the towers horizontally in longitudinal direction, the pylons can be constructed quite slender. The towers must be able to resist buckling due to compressive forces, forces from wind on the rest of the structure, forces due to oscillation both during construction and as a final construction, etc. Which material to use in the towers is influenced by several factors such as soil conditions, speed of erection, stability during construction, economical considerations, etc. [10]. Esthetical consideration has also been important in the design process as the appearance of suspension bridges are significant to the surroundings, e.g. the Golden Gate Bridge which is a landmark to the town of San Francisco.

2.5 Anchor blocks

Suspension bridges have earth anchored cable systems where tension forces in the main cables are transferred to the ground through the anchor blocks. The transmission of forces is established by anchoring each individual strand in the cables to the concrete of

the block. Using a splay saddle to separate the strands does this. Strands are referred to as a set of wires assembled together as prefabricated elements.

Chapter 3

Preliminary design

3.1 Geometry

Compared to the Hardanger bridge, which has a curvature of 20,000 m [19], the length of the main span will be about 2.82 times longer. Assuming a radius of curvature of the bridge girders 2.82 times higher than the Hardanger bridge will give a vertical curvature of about 56,500 m. Then the elevation of the girders will be 30.3 m above the supporting endpoints of the stiffening girder. The length of the stiffening girder will be 0.66 m longer than the projected length of the main span, see Appendix A.2. Normally the sag of the main cable is chosen as 1/10 of the span length [10, 23], i.e. 370 m. With a sailing clearance of 75 m, and a length of the shortest hanger equal to 2 m at midspan the total height from sea level to the top of the pylons will be (including a height of the girder of two meters);

$$k_{tot} = 370m + 2m + 2m + 75m = 449m$$

This implies that the pylons would have to be nearly 450 m high depending on topography and foundation, which is more than twice of those constructed for the Hardanger bridge. The topography on the Lavik-side is steep mountains directly from sea level, which means that the backstay cables don't have to be that long. On the other end of the bridge (Oppedal-side) the landscape is more flat, implying that the backstay cables have to be longer. In this thesis any considerations regarding the topography will not be considered, and the backstays will be assumed equal in length and geometry. Assuming that the backstays will be constructed as individual constructions, the bridge will be a single span suspension bridge. I.e. only the main span is supported by the cable system, but with the main cables continued as backstays from the pylon tops to the anchor blocks some distance from the pylons. The final geometry when all dead load acting on the bridge is shown in figure 3.1 on the following page. Different symbols that will be used throughout the thesis are listed below;

- k_m: Sag of the main span cable
- l_m: Horizontal main span length
- A_m: Area of suspension cable
- D_m: Diameter of cable

- F_{Rd}: Design tensile strength of cable or hanger steel
- γ_{cb}: Material density of steel (N/m^3)
- g_{cb}: Distributed load of cable along its length
- g_{cm}: Total cable weight distributed over the horizontal projected length of the cable

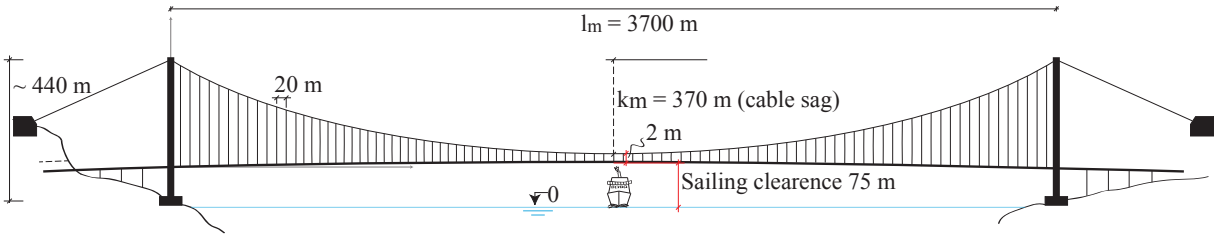

Figure 3.1: Geometry of the bridge.

3.2 Choice of stiffening girder shape

When constructing bridges with long spans, one of the most challenging problems is the aeroelastic stability in high wind speeds. In order to improve the aeroelastic stability, various researches have been conducted, and different configurations of the stiffening girder tested. Compared to the normally used single box girder for longer spans, e.g. Hardanger Bridge [22] and the Great Belt Bridge [10], it has been shown that slotted box girders gives improved aerodynamic behaviour [14, 30, 31]. To find the aeroelastic stability limit of a bridge it's necessary to find the aerodynamic derivatives of the girder. These can be found in literature, but it has not been successful to find girder shapes where all the 18 derivatives are given. This is due to the fact that wind tunnel tests usually are limited to vertical and rotational motion. I.e. the horizontal (lateral) displacements are not considered.

A choice of stiffening girder cross section has been made, see Figure 3.2 on the next page. This cross section has been tested in a wind tunnel on a scaled model and is given in Matsumoto et al. [14]. The cross section consists of two separated parallel box-girders, connected with a crossbeam at intermediate distance assumed to be 20 m. A vertical plate, "gap-plate", or central barrier centered in the cross section has been introduced to improve the stability in high wind speeds. The mass of the gap-plate is considered negligible and is left out in further calculations. Edge fairings are introduced, as can be observed in most bridges built with box-girders, in order to optimize the flow pattern around the cross section [10]. The chosen girder is henceforth referred to as cross section $2TFGP$. The dimensions are based on calculations given in Appendix A.3, where the width has been decided by using relevant Handbooks [17, 20].

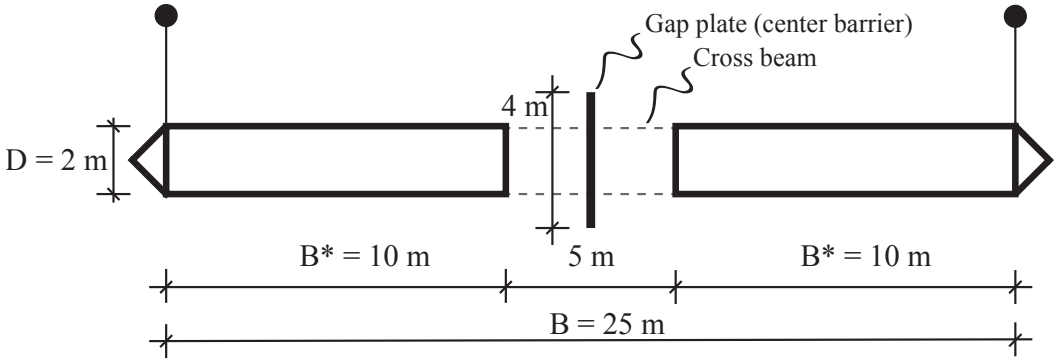

Figure 3.2: Chosen girder cross section.

3.3 Calculation of girder cross section parameters

When constructing a box-girder, there are several factors that must be considered in the design. The girder must globally be able to resist the moment distribution e.g. due to dead load, traffic load and wind load. Locally the steel plates must be thick enough to prevent local buckling due to moments from dead load, point loads, etc. Designing a box girder is a optimization process in the sense of maximizing the stiffness properties and at the same time minimizing the construction costs and the weight of the girder. The dimensioning is not the subject of this thesis and will not be considered because this is a time-consuming work. Instead other similarly box- girders has been studied, mainly the Hardanger Bridge and the new Svinesung Bride. The Svinesund Bridge has a similar cross section to the one chosen in this thesis with crossbeams connecting two symmetrically identical box-girders, see Figure 3.3. The width of the box-girders are of same magnitude, 11 m total width for Svinesund Bridge and 10 m for the actual bridge [7]. For simplicity, the same type and numbers of stiffeners has been adopted to the actual box-girders. The thickness of the plates are taken from the Svinesund cross section. One box-girder is modelled in CrossX [3] to find stiffness properties and mass of the suggested girder, see Figure 3.4 on the next page.

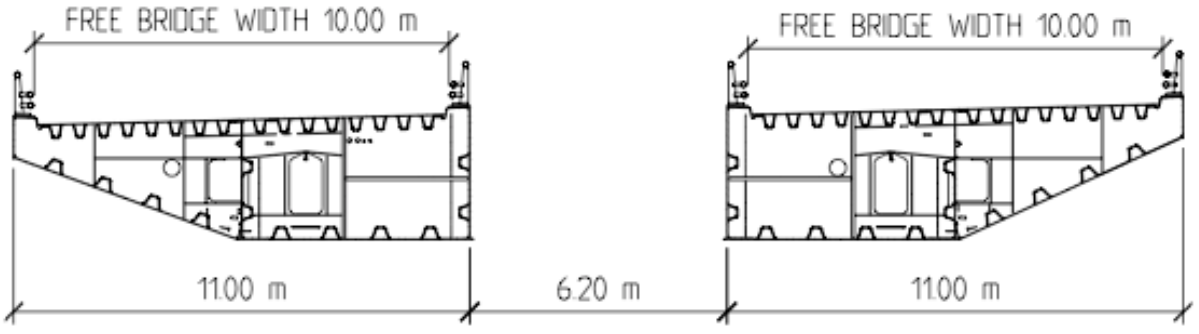

Figure 3.3: Girder cross section of the Svinesund Bridge [7].

The most important properties are summarized below. The material parameters used in

CrossX are given in the report presented in Appendix B. The origin (or reference point) is chosen in the left corner of the bottom plate, and the location of the shear centre and neutral axis (N.A) is given relative to this point. As can be seen from Figure 3.4 the shear centre almost coincides with the N.A, also shown in Figure 3.4. Here, Y' and Z' marks the reference coordinate system in CrossX, while Y and Z marks the coordinate system relative to the centroid. S shows the location of the shear centre. The direction of the coordinate system (Y, Z) is such that Y represents the strong axis of the cross section.

- Area: $A = 5.3175 * 10^5 mm^2$
- Second moment of inertia:
  1. $I_y = 6.1704 * 10^{12} mm^4$
  2. $I_z = 3.7967 * 10^{11} mm^4$
- Torsional moment of inertia: $I_t = 9.9314 * 10^{11} mm^4$
- Weight: $m = 4174.23 kg/m$
- Location of shear centre:
  - $y_s = 13.6mm$
  - $z_s = 48.8mm$

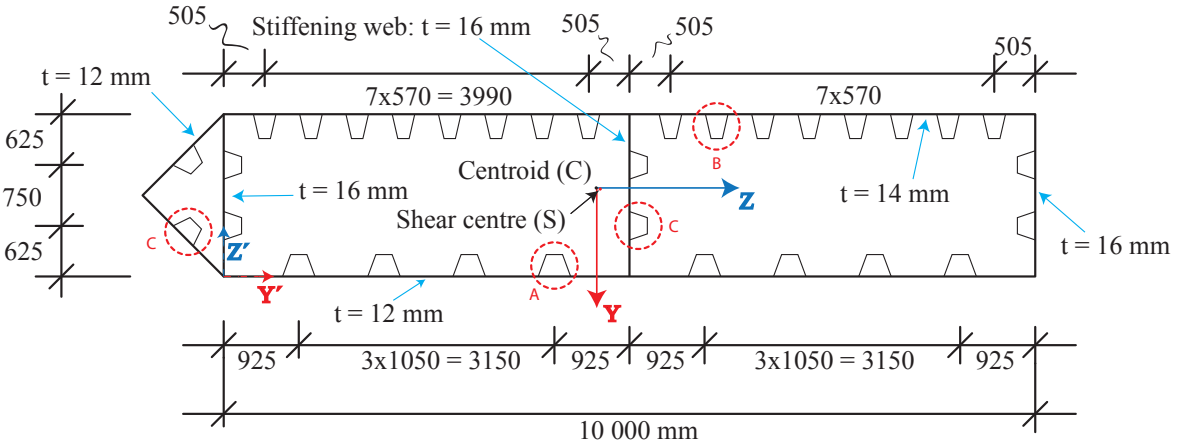

Figure 3.4: Box-girder with stiffeners modelled in CrossX.

3.4 Mass calculations

3.4.1 Specific weight

Parameters for specific weight of different components in the bridge are taken from handbooks given by The Norwegian Public Roads Administration. Parameters used in calculations are listed below [20]. The density used for steel is 7,850 kg/m^3, since this value is used in $CrossX$.

- Armed concrete: $\rho = 27kN/m^3$
- Asphalt: $\rho = 25kN/m^3$
- Steel railing (mass): $m = 0.5kN/m$

3.4.2 Dead load masses

Asphalt

According to Norwegian handbooks the weight of asphalt should be chosen as 2.0 kN/m^2. This value is a minimum requirement for AADT (Annual Average Daily Traffic volume) above 2000, and for bridge spans longer than 200 m. For pedestrian and cycling road the minimum value is set to 1.0 kN/m^2[20].

The road traffic spans over 6,5 m while 3 m for the pedestrian and cycling road. For simplicity it has been assumed that both girders have a walking/cycle path. Then the following distributed load on one box-girder will be;

$$6.5m * \frac{2000N/m^2}{9.81m/s^2} = 1325kg/m$$

$$3m * \frac{1000N/m^2}{9.81m/s^2} = 306kg/m$$

$$m_{asphalt} = \mathbf{1631kg/m} \tag{3.1}$$

Transverse bulkheads

In the box-girder there are intermediate transverse bulkheads assumed to cover the total cross sectional area of the girder. Any possibly transverse stiffeners on the bulkheads have been neglected. Also any holes for inspection and different installations have been neglected. The distance between bulkheads is chosen as 4 m, which means that there are five sections between each hanger in longitudinal direction. The total area within the outer plates is;

$$A = 10 * 2 + 2 * 1/2 \approx 21m^2$$

Assuming a plate thickness of 12 mm, this will give a distributed mass of;

$$m_{tb} = 21m^2 * 0.012m * 7850kg/m^3 * 1/4m = 495kg/m \approx \mathbf{500kg/m} \tag{3.2}$$

Steel railing

Since this thesis consists of a preliminary design, no details about types of railings will be given. Therefore values for the weight will be taken as $\rho = 0.5kN/m$ (see section 3.4.1 on the preceding page). With three railings on each girder, the distributed mass will be;

$$m_{rail} = 3 * 500N/m * 1/9.81m/s^2 = \mathbf{153kg/m} \tag{3.3}$$

Steel girder

Cross section values for the steel girder is given in Appendix B.1 , and repeated below. In addition there are non-constructional masses like electro installations, streetlights, ventilation systems etc. These masses are small compared to the girder, and therefore neglected. The attachments for the lower hanger links will contribute with some mass, but without any details of how these connections will be constructed some assumptions have been made. From calculations made for the Hardanger Bridge [19], each hanger attachment constitutes about 840 kg. The total amount of hangers equals the number of attachments, $n = l_m/20 = 185$, a total of 370 attachments. Assuming a weight of 850 kg per. attachment, this will give a distributed load on each girder as;

$$m_{hl} = 185 * 850kg * 1/3700m = \mathbf{43kg/m} \tag{3.4}$$

Values extracted from CrossX:

- Area: $A = 5.3175 * 10^5 mm^2$
- Weight per unit length:

$$m_g = \mathbf{4174.2\ kg/m} \tag{3.5}$$

Total dead load

Summing up the values from Equations 3.1-3.5 gives the total distributed dead load on each box-girder;

$$m_{dl,g} = (1631 + 500 + 153 + 43 + 4175)kg/m = \mathbf{6502\ kg/m} \tag{3.6}$$

3.4.3 Crossbeam

To connect the two box-girders, crossbeams will span laterally at every twenty meters. This solution was chosen on the new Svinesund Bridge, where the beam is simply a rectangular hollow beam with four plates welded together. The choice of plate thickness is an optimization process not taken into account in this thesis, and the same values are therefore used. The webs has been chosen a thickness of 14 mm while the flanges 30 mm. The height of the web has been chosen equal to the height of the box-girder, i.e. 2 m. The width of the beam has been chosen to 1 m. The cross sectional data has been calculated in CrossX, see Appendix B.2 . The distributed dead load in lateral direction is;

$$m_{cb,l} \approx 678kg/m = 6650N/m \tag{3.7}$$

The distance between each hanger is 20 m, which means that the hangers must carry load 10 m from each side in longitudinal direction. For simplicity, it has been assumed that both national lanes are loaded with full traffic load in the entire span, and without any loading in the pedestrian/cycling road, see Figure 3.5. This means that any point loads and load combinations are not considered. The procedure herein is assumed satisfactory for our purpose, and the loads are conservative. The traffic load is assumed distributed on the centre part of the top plate. The distributed load on each box-girder in lateral direction is given in the equation below. All estimations are calculated in the ultimate limit state (ULS). I.e. load factors are included, 1.3 for payloads and 1.2 for dead loads. The distributed load in longitudinal direction is taken from Handbooks as $9kN/m$ [20]. This load is distributed over 3 m in lateral direction, i.e. the load per. square meters is 3 kN/m^2.

$$p_{Ed} = 3kN/m^2 * 20m * 1.3 = 78000N/m \tag{3.8}$$

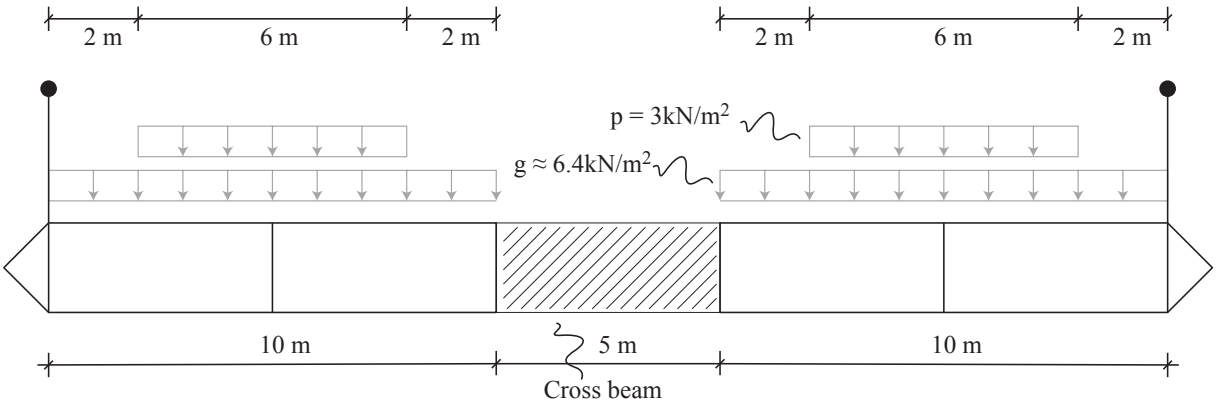

Figure 3.5: Distribution of load on girder. The load is given as distributed load per square meter.

The dead load weight on one box-girder from equation 3.6 is, when assuming that the dead load is distributed over the top plate of the girder ($10m$);

$$g_{Ed} = 6502kg/m * 9.81m/s^2 * 20m/10m * 1.2 = 153083.1N/m \tag{3.9}$$

Then the system can be illustrated as a simply supported beam with distributed mass, with the hangers representing the supports, see Figure 3.6. The force in each hanger can be calculated as;

$$\begin{aligned} N_H &= (78000N/m * 12m + 153083.1N/m * 20m + 6650N/m * 5m * 1.2)/2 \\ &= 2018790N \approx 2018.8kN \end{aligned} \tag{3.10}$$

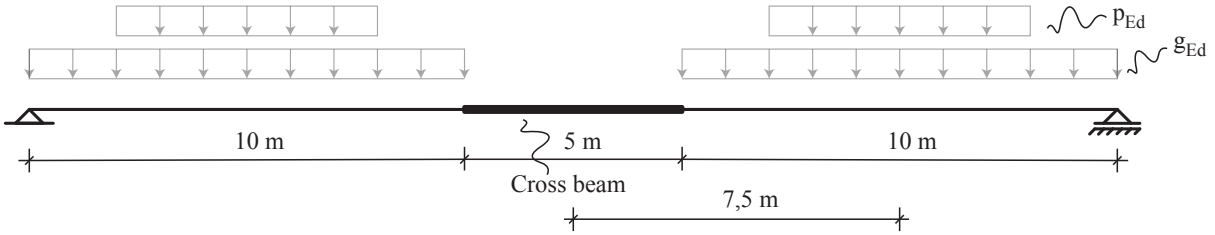

Figure 3.6: Static representation of cross section.

Maximum moment will occur in the middle of the crossbeam when assuming symmetry, and that the system can be considered as a simply supported beam with a span of 25 m between each cable plane. Referring to Figure 3.7 on the next page , the maximum moment will be;

$$\begin{aligned} M_{maks} &= N_H * 12.5m - 7.5 * (F_p + F_g) - 2.5^2/2 * m_{cb,l} * 1.2 \\ &= 10218637.5Nm \approx 10218.6kNm \end{aligned} \tag{3.11}$$

Where

- F_p is the resultant force from traffic load: $F_p = 78000N/m * 6m = 468kN$
- F_g is the resultant force from self weight: $F_g = 153084N/m * 10m = 1530.8kN$

Control of stresses in the crossbeam;

$$\sigma = \frac{M}{I_y} * z_{maks} = 223.9MPa \tag{3.12}$$

This value is about 72.5% of the yield stress when assuming $f_y = 355MPa$ and a material factor of 1.15 for regular steel. The dead load contribution from the crossbeam to each girder is then;

$$m_{cb} = 1/2 * 678kg/m * 5m/20m = \mathbf{84.8\ kg/m} \tag{3.13}$$

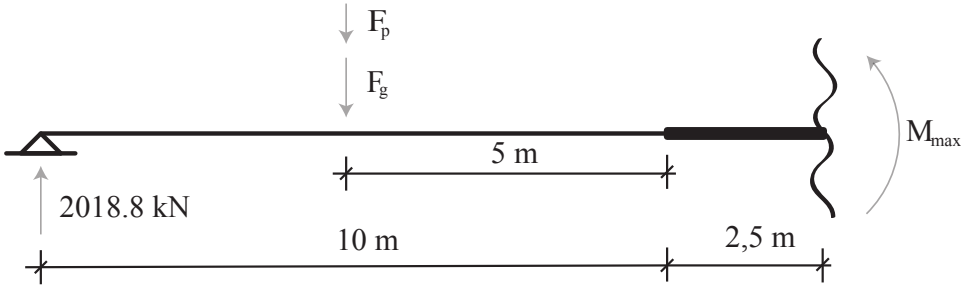

Figure 3.7: Maximum moment in crossbeam.

3.5 Mass moment of inertia of girder

In order to give a correct representation of the stiffening girder in an analysis program, where the cross section will not be modelled as it is but as line segments with assigned section properties, the mass moment of inertia (MOI) must be found. All masses, in addition to the girder mentioned in the preceding sections that contributes with inertia forces must be accounted for. The MOI is a property describing a body's resistance to angular acceleration. The definition of the MOI is as follows [12];

$$I = \int_m r^2 dm \tag{3.14}$$

Here the moment arm r is the distance from the axis to the element dm. Usually I is calculated about the body's mass centre G, defined as I_G. The MOI of the girder, calculated about an axis passing through the shear centre, is found by the use of the parallel-axis theorem. This theorem states that if the MOI about an axis passing through the body's mass centre is known, then the MOI through an arbitrary parallel axis can be determined. It can be shown that the MOI is equal to;

$$I = I_G + md^2 \tag{3.15}$$

Where

- I_G=moment of inertia about the axis passing through the mass centre
- m=mass of the body
- d=perpendicular distance between the two axes

The girder consists of plates welded together and stiffeners welded to the plates. Then it is convenient to threat every part separately, i.e. calculating the MOI of each part about it's own axis and use the parallel-axis theorem to calculate the MOI about the shear centre of the box-girder. When considering the stiffeners only the second term of Equation 3.15 is evaluated, since the first term will be small. The results are given in

Appendix A.5 , and the most important values are summed up in Table 3.1. Here the values are given as units per length of one girder.

Table 3.1
Summary of cross section values.

Girder element	Mass m (kg/m)	my' (kgm/m)	mz' (kgm/m)	I (kgm^2/m)
Longitudinal steel	4,173.4	9,072.2	4,755.8	51,454.9
Transvers bulkheads	494.6	2,347.2	494.5	5,167.0
Asphalt	1,631.0	9,555.8	3,321.1	14,507.1
Railing	153.0	548.3	397.8	1,515.3
Lower hanger attachment	43.0	0.0	86.0	954.1
Sum:	**6,494.9**	31,523.3	9,055.3	**73,598.4**

The centre of gravity (COG) of the girder including asphalt, railing etc. can be found by the following equation [12];

$$\bar{z} = \frac{\sum mz'}{\sum m} \qquad \bar{y} = \frac{\sum my'}{\sum m} \tag{3.16}$$

Here, $\bar{z}$ and $\bar{y}$ are related to the coordinate system (Y',Z'), see Figure 3.4 on page 12. Using the values from table 3.1, gives the following coordinates of the COG;

- $\bar{z} = 1.39$ m
- $\bar{y} = 4.85$ m

Table 3.2
Location of centre of gravity.

Coordinates	Center of gravity of girder			
	With additional mass (m)	Calculated COG of steel girder (m)	COG from CrossX (m)	Difference (m)
$\bar{z}$	1.39	1.14	1.09	-0.049
$\bar{y}$	4.85	4.57	4.4507	0.0005

As can be seen from Table 3.2 the COG from manual calculations almost coincide with the values extracted from CrossX, with some error of about $5cm$ in vertical direction (without additional mass). This also confirms that the theoretical calculations are reasonable.

3.6 Estimation of hanger dimensions

The length of each hanger is equal to the distance between the girder and the cable. The total weight of the hangers is calculated and then divided by the total span length to get an even distributed load on the cable. This is not quite correct since the hangers are longer near the pylons then at the middle of the bridge, but this is neglected. The dimensioning is done in the ultimate limit state (ULS), and load factors have therefore been used. With the dead load of the girder and full traffic load, and assuming that the hangers must transfer all load a distance $20m$ between each hanger in longitudinal direction, the force in each hanger are given from Equation 3.10 on page 16 as;

$$N_h = 2018.8kN \tag{3.17}$$

The nominal tensile stress for the hangers are $F_{uk,h} = 1{,}570\ MPa$ [18]. The design tensile stress F_{Rd} is given from Equation 3.18. Here the material factor γ_m is equal to 1.2 [21] The required steel area of each hanger is then given by Equation 3.19;

$$F_{Rd,h} = \frac{F_{uk}}{1.5 \cdot \gamma_m} = \frac{1,570}{1.5 \cdot 1.2} = 872.2MPa \tag{3.18}$$

$$A_h = \frac{N_h}{F_R} = 2314.6mm^2 \tag{3.19}$$

This will give a required diameter of $D_h = \sqrt{\frac{4A_h}{\pi}} = 54.3mm \approx 0.054m$. Choosing a value of $D_h = 0.05m$ since the loading is conservative. The distributed load per unit length of hanger is;

$$m_h = 15.4kg/m \tag{3.20}$$

The total amount of steel from hangers needed is found from calculations in $MATLAB$ [36]. The quantities are given below.

- $suml_h = 25054m$: total length of hangers (one cable plane)
- $Q_{mh} = 386180kg$ (total quantity of hanger steel, one cable plane)

Assuming that the total weight of hanger steel is distributed evenly over the length of the span gives a distributed mass over one box-girder as;

$$m_{m,h} = Q_{mh}/l_m = \mathbf{104.4kg/m} \tag{3.21}$$

3.7 Estimation of cable dimensions

In section 3.4 the total dead load of the girder was found. In order to find an approximate cable dimension, dead load of the girder and traffic load over the entire span will be assumed in the calculations. In addition the dead load from the hangers is given in Equation 3.21 on the preceding page. The total dead load per box-girder, with a load factor of 1.2, will be;

$$\begin{aligned} g_{Ed} &= (m_{dl,g} + m_{cb} + m_{m,h}) * 9.81 m/s^2 * 1.2 \\ &= (6502 kg/m + 84.8 kg/m + 104.4) * 9.81 m/s^2 * 1.2 \approx 78768.8 N/m \end{aligned} \tag{3.22}$$

Distributed load from traffic, when the assumption mentioned in Section 3.4.3 on page 15 with full traffic load in both national lanes and load factor 1.5, will be;

$$p_{Ed} = 3 kN/m^2 * 6m * 1.3 = 23400 N/m \tag{3.23}$$

An expression for the cable area required carrying all the dead load of the girder with additional mass, the hangers and the weight of the cable itself is given in Equation 3.24 (neglecting any concentrated forces)[10]. This equation is based on the assumption that the cable weight is distributed over the horizontal projection of the cable length. Clearly this is not correct since the weight is distributed along the length of the cable, leading to a higher dead load per meter horizontally near the towers. It is assumed that if this bridge is to be constructed, a higher nominal tensile strength of the cable steel has been developed. In the calculations it is assumed a nominal tensile strength of 1,850 MPa compared to 1,770 MPa which is the maximum strength used today. This will give a design tensile strength of the cables equal to $F_{Rd,c} = 1{,}027.8\ MPa$.

$$A_m = \frac{(p_{Ed} + g_{Ed}) l_m \sqrt{l_m^2 + 16 k_m^2}}{8 F_{Rd,c} k_m - \gamma_{cb} l_m \sqrt{l_m^2 + 16 k_m^2}} \tag{3.24}$$

Replacing g_{cb} with $g_{cm} = g_{cb} * l_c / l_m$ gives a more precise representation of the total load of the cable, but the difference is considerably small (2,6%). Equation 3.24 will then become;

$$A_m = \frac{(p_{Ed} + g_{Ed}) l_m \sqrt{l_m^2 + 16 k_m^2}}{8 F_{Rd,c} k_m - \gamma_{cb} l_c \sqrt{l_m^2 + 16 k_m^2}} \tag{3.25}$$

The density is here given as $\gamma_{cb} = \rho_{cb} \cdot 9.81 N/m^3$. Using the values found in Equations 3.22-3.23, the total area of steel required is found as;

$$A_m = 0.8025 m^2 \tag{3.26}$$

This gives a diameter of $D_m = \sqrt{\frac{4A_m}{\pi}} = 1.011m$. Choosing a value of $D_m = 1.0\ m$ since the assumption made regarding the loading have been conservative. This gives the following distributed load along the cable as;

$$m_{cb} = \frac{\pi}{4} D_m^2 * \rho_{cb} = \mathbf{6165.4\ kg/m} \tag{3.27}$$

and the distributed load on the projected length as;

$$m_{cm} = m_{cb} * l_c/l_m = \mathbf{6326\ kg/m} \tag{3.28}$$

3.8 Cable forces

The maximum cable forces can be determined assuming that all loads are distributed uniformly in the entire span. The horizontal force can be found considering the midpoint of the span where the sag is 370 m in the dead load condition. Then the system can be described as a simply supported beam with distributed load, which gives a maximum moment at midpoint as $ql_2^2/8$. This moment must be balanced out by the horizontal cable force with a moment arm of 370 m. Assuming dead load geometry when the bridge is loaded with traffic, the horizontal force becomes;

$$H_m = \frac{ql_m^2}{8k_m} + \frac{g_{cm}l_m^2}{8k_m} = \frac{(g+p)l_m^2}{8k_m} + \frac{g_{cm}l_m^2}{8k_m} \tag{3.29}$$

Where

- $g = (6502kg/m + 84.8kg/m + 104.4) * 9.81m/s^2 = 65640N/m$: Dead load of girder, hangers and additional mass (without load factor)
- $p = 3kN/m^2 * 6m = 18000N/m$: Traffic load (without load factor)
- $g_{cm} = m_{cm} * 9.81m/s^2 = 62058N/m$

$$H_m = \frac{(65640 + 18000 + 62058)N/m * (3700m)^2}{8 * 370m} \approx 673853.3kN \tag{3.30}$$

The load would have been smaller if the deflected geometry was considered, leading to larger cable sag. The horizontal force in the cable without the traffic load will be;

$$H_m = \frac{(65640 + 62058)N/m * (3700m)^2}{8 * 370m} \approx 590603.3kN \tag{3.31}$$

When the horizontal cable force is known, the maximum cable force can be found from Equation 3.32 on the following page [12]. Maximum tension in the cable will occur where the slope of the cable has it's maximum, i.e. at the pylon top.

$$T_{max} = \frac{(p + g + g_{cm})l_m}{2}\sqrt{1 + \left(\frac{l_m}{4k_m}\right)^2} \approx 725762.2kN \tag{3.32}$$

This gives a stress of 924.1 MPa, which leads to a load/capacity ratio of 90% when using the design tensile stress. Without the traffic load the maximum force will be;

$$T_{max} = \mathbf{636099\ kN} \tag{3.33}$$

and accordingly a load/capacity ratio of 78.8%. The cable area should probably be increased, but is considered satisfactory for our purpose.

3.9 Total mass of bridge

The total weight of the bridge is given in Table 3.3. Here the total mass of the bridge is given with only dead loads, which will be compared to the bridge in the analysis model. The backstays are not included here.

Table 3.3
Total mass of the main span: The distributed masses is given for one plane, while the total mass is obtained by multiplying the distributed mass with the length of each element and a quantity of 2.

Structural element	Diameter (m)	Amount	Distributed mass (kg/m) one plane	Mass ($tons$)
Cable	1.0	2	6,165.4	46,812.7
Hangers	0.05	370	104.4	772.4
Girder		2	6,502	48,114.8
crossbeam		185	84.8	313.8
Total			**12,856.6**	**96,013.6**

Chapter 4

Aeroelastic stability

4.1 Introduction

An important task when designing long span bridges is to insure that the vibrations due to wind loads are within accepted limits. Especially at high wind speeds, phenomenon such as galloping and flutter can be crucial and fatal to the construction. These self-exited vibrations are caused by changes in the total stiffness and damping of the structure. After the famous Tacoma Narrow bridge collapse, these phenomena has been subject to a lot of research, especially flutter instabilities, which consist of coupling of vibration modes.

The central theory describing wind loads on bridges, causing these effects are the buffeting theory. The total load can be described as a contribution from the mean wind velocity in the main flow direction (V), the velocity fluctuations u, v and w as well as motion induced contributions. The fluctuations in the main flow direction is denoted u; v describes fluctuations in the along structure direction while w describes the vertical fluctuations. Directions are related to a horizontal line like structure with the main wind flow perpendicular to the structure's longitudinal axis (x-axis). As these fluctuating components are stochastic variables they are functions both in space and in time. It is assumed that a bridge describes a line-like structure, the wind field is stationary and homogeneous and that the main flow direction is perpendicular to the longitudinal x-axis. The fluctuating component in x-direction are of no interest, leaving the along wind and the across vertical direction as the interesting parts. Basic assumptions in this theory is that the loads can be calculated from the instantaneous velocity pressure, load coefficients are found in wind tunnel experiments and a linearization of fluctuating parts will give acceptably accurate results. Structural displacements and rotations are assumed small, and u, w are assumed small compared to V [35]. The theory described is shown in Figure 4.1 on the following page. Explanations of the given components are given below, and where any fluctuating component can be described by a time invariant mean part and a zero mean fluctuating part.

From Figure 4.1 on the next page it can be seen that the cross section is given a static displacement $\bar{r}_y(x)$, $\bar{r}_z(x)$ and $\bar{r}_\theta(x)$. About this point the section oscillates with a dynamic displacement $r_y(x,t)$, $r_z(x,t)$ and $r_\theta(x,t)$. Components of displacement and distributed forces can be written as;

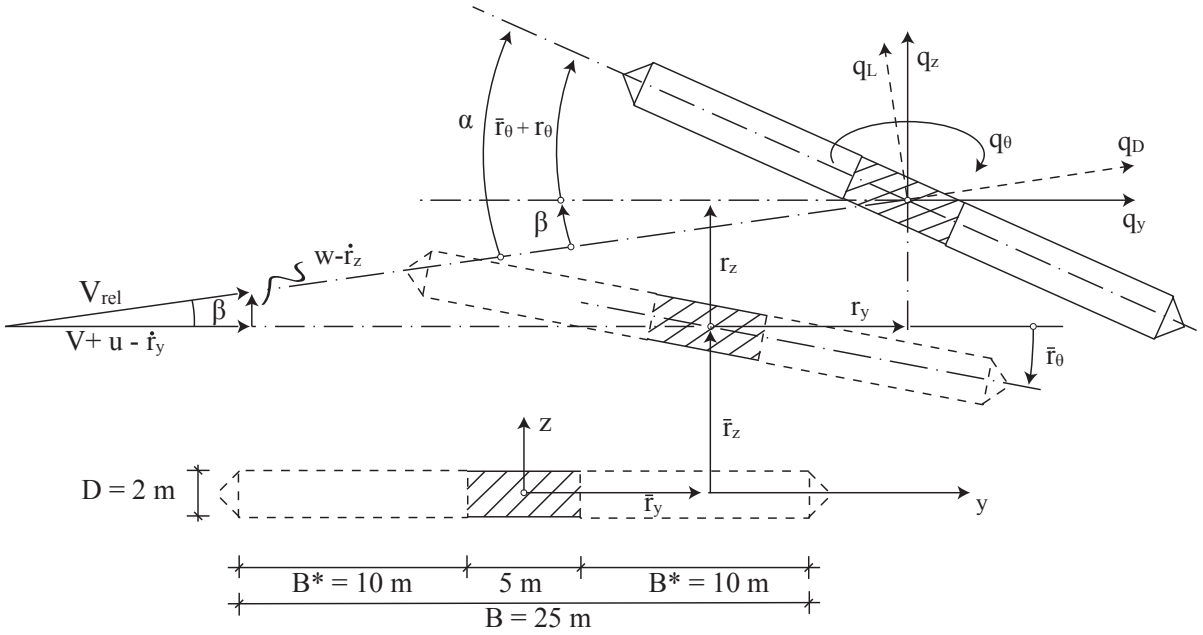

Figure 4.1: Representation of instantaneous flow, displacement and forces.

$$\begin{aligned}
\boldsymbol{r}_{tot}(x,t) &= \bar{\boldsymbol{r}}(x) + \boldsymbol{r}(x,t), \quad \bar{\boldsymbol{r}}(x) = \begin{bmatrix}\bar{r}_y & \bar{r}_z & \bar{r}_\theta\end{bmatrix}^T, \quad \boldsymbol{r}(x,t) = \begin{bmatrix}q_y & q_z & q_\theta\end{bmatrix}^T \\
\boldsymbol{q}_{tot}(x,t) &= \bar{\boldsymbol{q}}(x) + \boldsymbol{q}(x,t), \quad \bar{\boldsymbol{q}}(x) = \begin{bmatrix}\bar{q}_y & \bar{q}_z & \bar{q}_\theta\end{bmatrix}^T, \quad \boldsymbol{q}(x,t) = \begin{bmatrix}q_y & q_z & q_\theta\end{bmatrix}^T
\end{aligned} \tag{4.1}$$

The cross sectional drag, lift and moment forces in the flow axis defined in Figure 4.1, are given by;

$$\begin{bmatrix} q_D(x,t) \\ q_L(x,t) \\ q_M(x,t) \end{bmatrix} = \frac{1}{2}\rho V_{rel}^2 \cdot \begin{bmatrix} D \cdot C_D(\alpha) \\ B \cdot C_L(\alpha) \\ B^2 \cdot C_M(\alpha) \end{bmatrix} \tag{4.2}$$

The load coefficients describe non-linear curves dependent on the instantaneous oscillation angle. A linearization of the load coefficients in Equation 4.2 gives the following linear equations;

$$\begin{bmatrix} C_D(\alpha) \\ C_L(\alpha) \\ C_M(\alpha) \end{bmatrix} = \begin{bmatrix} C_D(\bar{\alpha}) \\ C_L(\bar{\alpha}) \\ C_M(\bar{\alpha}) \end{bmatrix} + \alpha_f \begin{bmatrix} C'_D(\bar{\alpha}) \\ C'_L(\bar{\alpha}) \\ C'_M(\bar{\alpha}) \end{bmatrix} = \begin{bmatrix} \bar{C}_D \\ \bar{C}_L \\ \bar{C}_M \end{bmatrix} + \alpha_f \begin{bmatrix} C'_D \\ C'_L \\ C'_M \end{bmatrix} \tag{4.3}$$

Here, $\bar{\alpha}$ and α_f are the mean value and the fluctuating part of the angle of incidence respectively. C'_D, C'_L and C'_M are the slopes of the load coefficient curves at the mean angle $\bar{\alpha}$. The expression for the total load matrix can be found in [35] as;

$$\begin{bmatrix} q_y \\ q_z \\ q_\theta \end{bmatrix}_{tot} = \rho V \left(\frac{V}{2} + u - \dot{r}_y \right) \left\{ \begin{bmatrix} D\bar{C}_D \\ B\bar{C}_L \\ B^2\bar{C}_M \end{bmatrix} + \left(r_\theta + \tfrac{w}{V} - \tfrac{\dot{r}_z}{V} \right) \begin{bmatrix} DC'_D \\ BC'_L \\ B^2C'_M \end{bmatrix} + \tfrac{w-\dot{r}_z}{V} \begin{bmatrix} -B\bar{C}_L \\ D\bar{C}_D \\ 0 \end{bmatrix} \right\} \tag{4.4}$$

An expression on matrix form is given below. Higher order terms containing products of quantities that are assumed small, are disregarded.

$$\boldsymbol{q}_{tot}(x,t) = \begin{bmatrix} \bar{q}_y(x) \\ \bar{q}_z(x) \\ \bar{q}_\theta(x) \end{bmatrix} + \begin{bmatrix} q_y(x,t) \\ q_z(x,t) \\ q_\theta(x,t) \end{bmatrix} = \bar{\boldsymbol{q}} + \boldsymbol{B}_q \cdot \boldsymbol{v} + \boldsymbol{C}_{ae} \cdot \dot{\boldsymbol{r}} + \boldsymbol{K}_{ae} \cdot \boldsymbol{r} \tag{4.5}$$

where

$$\boldsymbol{v}(x,t) = \begin{bmatrix} u & w \end{bmatrix}^T \tag{4.6}$$

$$\boldsymbol{r}(x,t) = \begin{bmatrix} r_y & r_z & r_\theta \end{bmatrix}^T \tag{4.7}$$

$$\bar{\boldsymbol{q}}(x) = \begin{bmatrix} \bar{q}_y \\ \bar{q}_z \\ \bar{q}_\theta \end{bmatrix} = \frac{\rho V^2 B}{2} \begin{bmatrix} (D/B)\bar{C}_D \\ \bar{C}_L \\ B\bar{C}_M \end{bmatrix} = \frac{\rho V^2 B}{2} \cdot \hat{\boldsymbol{b}}_q \tag{4.8}$$

$$\boldsymbol{B}_q(x) = \frac{\rho V B}{2} \begin{bmatrix} 2(D/B)\bar{C}_D & \left((D/B)C'_D - \bar{C}_L\right) \\ 2\bar{C}_L & \left(C'_L + (D/B)\bar{C}_D\right) \\ 2B\bar{C}_M & BC'_M \end{bmatrix} = \frac{\rho V B}{2} \cdot \hat{\boldsymbol{B}}_q \tag{4.9}$$

$$\boldsymbol{C}_{ae}(x) = -\frac{\rho V B}{2} \begin{bmatrix} 2(D/B)\bar{C}_D & \left((D/B)C'_D - \bar{C}_L\right) & 0 \\ 2\bar{C}_L & \left(C'_L + (D/B)\bar{C}_D\right) & 0 \\ 2B\bar{C}_M & BC'_M & 0 \end{bmatrix} \tag{4.10}$$

$$\boldsymbol{K}_{ae}(x) = \frac{\rho V^2 B}{2} \begin{bmatrix} 0 & 0 & (D/B)C'_D \\ 0 & 0 & C'_L \\ 0 & 0 & BC'_M \end{bmatrix} \tag{4.11}$$

It is seen that the total load vector is compounded by a static part and a fluctuating part. Some improvements have been made to make the buffeting theory suitable for a modal frequency domain approach. Frequency dependent flow induced dynamic load has been suggested to replace $\boldsymbol{B}_q$ from Equation 4.9, where frequency dependent admittance functions has been added to account for characteristics of the cross section, see [35]. Secondly the contents of $\boldsymbol{K}_{ae}$ and $\boldsymbol{C}_{ae}$ has been replaced with aerodynamic derivatives,

which are functions of the frequency of motion, the mean wind velocity and type of cross section.

The self-excited forces can be approximated by solving Equation 4.4 on the preceding page, disregarding any higher order terms and only looking at terms associating with $\boldsymbol{r}_n$ and $\dot{\boldsymbol{r}}_n$, $n \in \{y, z, \theta\}$. This gives the three force components;

$$
\begin{aligned}
q_{y,se} &= \frac{1}{2}\rho V^2 B\left(-2(D/B)\bar{C}_D\frac{\dot{r}_y}{V} - ((D/B)C'_D - C'_L)\frac{\dot{r}_z}{V} + (D/B)C'_D r_\theta\right)\\
q_{z,se} &= \frac{1}{2}\rho V^2 B\left(-2\bar{C}_L\frac{\dot{r}_y}{V} - (C'_L + (D/B)\bar{C}_D)\frac{\dot{r}_z}{V} + C'_L r_\theta\right)\\
q_{\theta,se} &= \frac{1}{2}\rho V^2 B^2\left(-2\bar{C}_M\frac{\dot{r}_y}{V} - C'_M\frac{\dot{r}_z}{V} + C'_M r_\theta\right)
\end{aligned}
\tag{4.12}
$$

This theory arrived from the buffeting theory and also called the quasi-steady theory, is applicable both in frequency domain as well as in time domain. As stated in Øiseth et al. [26] the theory is only valid when the period of oscillation is high compared to the time of the air flow to travel the distance across the section. Neither does the theory contribute with torsional damping related with torsional motion terms, $\dot{r}_\theta$. The improved theory, as mentioned above, uses aerodynamic derivatives to describe $\boldsymbol{K}_{ae}$ and $\boldsymbol{C}_{ae}$. The forces associated with the aerodynamic derivatives are given in Sarkar et al. [29] as (see also [26] and [5]);

$$
\begin{aligned}
q_{y,se} &= \frac{1}{2}\rho V^2 B\left(KP_1^*\frac{\dot{r}_y}{V} + KP_2^*\frac{B\dot{r}_\theta}{V} + K^2P_3^* r_\theta + K^2P_4^*\frac{r_y}{B} + KP_5^*\frac{\dot{r}_z}{V} + K^2P_6^*\frac{r_z}{B}\right)\\
q_{z,se} &= \frac{1}{2}\rho V^2 B\left(KH_1^*\frac{\dot{r}_z}{V} + KH_2^*\frac{B\dot{r}_\theta}{V} + K^2H_3^* r_\theta + K^2H_4^*\frac{r_z}{B} + KH_5^*\frac{\dot{r}_y}{V} + K^2H_6^*\frac{r_y}{B}\right)\\
q_{\theta,se} &= \frac{1}{2}\rho V^2 B^2\left(KA_1^*\frac{\dot{r}_z}{V} + KA_2^*\frac{B\dot{r}_\theta}{V} + K^2A_3^* r_\theta + K^2A_4^*\frac{r_z}{B} + KA_5^*\frac{\dot{r}_y}{V} + K^2A_6^*\frac{r_y}{B}\right)
\end{aligned}
\tag{4.13}
$$

Here, $K = (\omega B)/V$ denotes the reduced frequency, B the total girder width, ω the circular frequency of motion and $P_n^*, H_n^*, A_n^*, n \in \{1, 2, ..., 6\}$ are the dimensionless aerodynamic derivatives which are functions of the reduced velocity. The self-exited forces are due to interaction of the wind flow and the structure. Aerodynamic derivatives are strictly dependent on the geometry of the bridge girder and the reduced velocity, and they result in modifying the structural damping and stiffness away from their mechanical counterparts found from a zero-wind case. It's notable from Equation 4.13 that H_1^* and A_2^* are the aerodynamic damping in vertical and torsional motion respectively, as stated in Dyrbye and Hansen [8]. Usually, the aerodynamic derivatives have been found trough experiments done in wind tunnel tests of section models, and limited to vertical and torsional displacements. I.e. the terms associated with the along wind motion must either be disregarded or taken from the quasi-static theory, see [35]. They can found by comparing Equation

4.10 and 4.11 on page 25 with Equation 4.14. The contents of $\boldsymbol{K}_{ae}$ and $\boldsymbol{C}_{ae}$ can be found as [26, 35];

$$\boldsymbol{C}_{ae}(x) = \frac{\rho B^2}{2}\omega_i(V)\begin{bmatrix} P_1^* & P_5^* & BP_2^* \\ H_5^* & H_1^* & BH_2^* \\ BA_5^* & BA_1^* & B^2A_2^* \end{bmatrix}, \boldsymbol{K}_{ae}(x) = \frac{\rho B^2}{2}\omega_i^2(V)\begin{bmatrix} P_4^* & P_6^* & BP_3^* \\ H_6^* & H_4^* & BH_3^* \\ BA_6^* & BA_4^* & B^2A_3^* \end{bmatrix} \tag{4.14}$$

As shown in 4.14 the resonant frequency $\omega_i(V)$ is a function of the mean wind velocity V. At $V = 0$, ω_i is the natural-frequency in still air. When $V \neq 0$ the aerodynamic derivatives changes the total stiffness and damping of the structure, as mentioned above, i.e. calculations involving the aerodynamic derivatives demands iterations.

4.2 Flutter phenomena

The flutter stability limit is defined as when the input from the motion-induced loads is equal to the energy dissipated by structural damping. Flutter is characterized as a coupled translational and twisting (torsional) motion that will occur when the natural frequencies of vertical and torsional oscillations are close to each other and the torsional frequency is higher than the vertical frequency. When the difference of natural frequencies are high, coupled flutter will not occur but the critical oscillation will be pure torsional [10, 33, 35]. At, or in the vicinity of an instability limit the dominating forces are the motion-induced loads. The flutter phenomena originally described the behaviour of thin airfoils but have also found its application to suspension bridges. The coupling of vibration modes are called *classical flutter* and will be discussed further in this thesis.

The structure consists of several modes of vibration, and some more dominating then others. Vibrations occur as coupling between modes, and the modes that give coupling has the largest deflections at the same part of the bridges. The first vertical symmetric and first symmetric torsional modes are likely to couple since the largest deflection of the modes occur at the same point of the bridge, namely the midpoint. On the other hand it's not likely that the first vertical symmetric and first torsional asymmetric mode will couple since the torsional mode has small deflections where the vertical mode has large deflections. The coupling and the shapes of the modes play an important role in aeroelasticity and flutter considerations. The bridge will clearly have horizontal deflections as well, but in most situations the vertical load/deflection and angular moment/rotation will not couple significantly to the horizontal deflections. As the lengths of suspension bridges are increasing, e.g. above 2 km, the horizontal deflections will be significant. In these cases where modes of vertical, torsional and horizontal deflection couples may become important [8]. To apply the theory mentioned in Section 4.1, the formulation must include all terms of the aeroelastic loads (motion induced loads), i.e. the formulation must include all the 18 different aerodynamic derivatives. Usually any horizontal deflections of a section in a wind tunnel are neglected leaving only eight derivatives associated with vertical deflection/velocity and torsional rotations/angular velocity left. I.e. $H_n^*, A_n^*, n \in$

$\{1,2,3,4\}$ are the only experimentally obtained coefficients. The remaining coefficients $H_n^*, A_n^*, n \in \{5,6\}$ and $P_n^*, n \in \{1,2...,6\}$ are usually taken from the quasi-steady theory (or disregarded) by comparing Equation 4.14 on the previous page with Equations 4.10-4.11, rendering;

$$P_1^* = -2\bar{C}_D \frac{D}{B}\left(\frac{1}{K}\right) \quad P_5^* = \left(\bar{C}_L - C'_D \frac{D}{B}\right)\left(\frac{1}{K}\right) \quad P_3^* = C'_D \frac{D}{B}\left(\frac{1}{K}\right)^2$$
$$H_5^* = -2\bar{C}_L\left(\frac{1}{K}\right) \quad A_5^* = -2\bar{C}_M\left(\frac{1}{K}\right) \quad P_2^* = P_4^* = P_6^* = H_6^* = A_6^* = 0 \tag{4.15}$$

4.3 Flutter equations

When finding an instability limit, so called flutter equations can be used to estimate the critical mean wind velocity. These equations [8, 33, 35], are based on a modal approach where the structural displacements are expressed as the sum of the products between natural eigen-modes, $\boldsymbol{\varphi}_i$ and time dependent generalized coordinates, η_i;

$$\boldsymbol{r}(x,t) = \sum_{i=1}^{N_{mod}} \begin{bmatrix} \phi_y(x) \\ \phi_z(x) \\ \phi_\theta(x) \end{bmatrix}_i \cdot \eta_i(t) = \boldsymbol{\Phi}(x) \cdot \boldsymbol{\eta}(t), \quad \boldsymbol{\Phi}(x) = \begin{bmatrix} \boldsymbol{\varphi}_1(x) & ... & \boldsymbol{\varphi}_i(x) & ... & \boldsymbol{\varphi}_{N_{mod}}(x) \end{bmatrix}$$
$$\boldsymbol{\eta}(t) = \begin{bmatrix} \eta_1(t) & ... & \eta_i(t) & ... & \eta_{N_{mod}}(t) \end{bmatrix}^T, \quad \boldsymbol{\varphi}_i(x) = \begin{bmatrix} \phi_y & \phi_z & \phi_\theta \end{bmatrix}_i^T \tag{4.16}$$

Where $\phi_n, n \in \{y,z,\theta\}$ describing the lateral, vertical and torsional displacements along the bridge girder, respectively. Thus, it's assumed that the output of the system can be sufficiently described by an eigenvalue solution containing the necessary eigen-modes and corresponding eigen-frequencies (natural frequencies). The eigen-modes and their frequencies are usually extracted from a finite element method program (FEM), in this thesis $ABAQUS$ will we used. The FEM solution will give undamped natural frequencies from a zero wind case. Axial displacements along the bridge girder are disregarded, since this direction is not directly associated with any motion induced loads. From here, any motion induced terms associated with structural acceleration is disregarded. N_{mod} is the number of modes that has been chosen to give an accurately enough solution. Disregarding the mean load in equation 4.1 on page 24 the total load can be written as;

$$\boldsymbol{q}_{tot} = \boldsymbol{q}(x,t) + \boldsymbol{q}_{ae}(x,t,\boldsymbol{r},\dot{\boldsymbol{r}},\ddot{\boldsymbol{r}})$$
$$\text{where} \quad \begin{cases} \boldsymbol{q}(x,t) = \begin{bmatrix} q_y & q_z & q_\theta \end{bmatrix}^T \\ \boldsymbol{q}_{ae}(x,t,\boldsymbol{r},\dot{\boldsymbol{r}},\ddot{\boldsymbol{r}}) = \begin{bmatrix} q_y & q_z & q_\theta \end{bmatrix}_{ae}^T \end{cases} \tag{4.17}$$

Introducing the relations mentioned in Equations 4.16 on the preceding page- 4.17 on the facing page into the equilibrium equation will render N_{mod} modal equilibrium conditions;

$$\tilde{\boldsymbol{M}}_0 \cdot \ddot{\boldsymbol{\eta}}(t) + \tilde{\boldsymbol{C}}_0 \cdot \dot{\boldsymbol{\eta}}(t) + \tilde{\boldsymbol{K}}_0 \cdot \boldsymbol{\eta}(t) = \tilde{\boldsymbol{Q}}(t) + \tilde{\boldsymbol{Q}}(t, \eta, \dot{\eta}, \ddot{\eta}) \tag{4.18}$$

The modal flow induced load vector in the equation above is given by;

$$\begin{aligned} &\tilde{\boldsymbol{Q}}(t) = \begin{bmatrix} \tilde{Q}_1 & ... & \tilde{Q}_i & ... & \tilde{Q}_{N_{mod}} \end{bmatrix}^T \\ \text{where} \qquad &\tilde{Q}_i = \int_{L_{exp}} (\boldsymbol{\varphi}_i^T \cdot \boldsymbol{q}) dx \end{aligned} \tag{4.19}$$

Here L_{exp} is the wind exposed length of the girder, usually set equal to the length, L. $\tilde{\boldsymbol{M}}_0$ is the modal mass matrix; $\tilde{\boldsymbol{C}}_0$ is the modal damping matrix and $\tilde{\boldsymbol{K}}_0$ modal stiffness matrix. Index zero indicates structural properties in vacuum or in a zero wind condition. A Fourier transform of the aerodynamic modal load will render a Fourier amplitude given by;

$$\boldsymbol{a}_{\tilde{Q}ae} = (\tilde{\boldsymbol{C}}_{ae} i\omega + \tilde{\boldsymbol{K}}_{ae}) \cdot \boldsymbol{a}_\eta \tag{4.20}$$

Where $\tilde{\boldsymbol{C}}_{ae}$ is the modal aerodynamic damping matrix and $\tilde{\boldsymbol{K}}_{ae}$ represents the modal aerodynamic stiffness matrix. The elements of $\tilde{\boldsymbol{C}}_{ae}$ and $\tilde{\boldsymbol{K}}_{ae}$ are given by;

$$\begin{bmatrix} \tilde{C}_{ae_{ij}} \\ \tilde{K}_{ae_{ij}} \end{bmatrix} = \int_{L_{exp}} \begin{bmatrix} \boldsymbol{\varphi}_i^T \cdot \boldsymbol{C}_{ae} \cdot \boldsymbol{\varphi}_j \\ \boldsymbol{\varphi}_i^T \cdot \boldsymbol{K}_{ae} \cdot \boldsymbol{\varphi}_j \end{bmatrix} dx \tag{4.21}$$

Performing a Fourier transform on both sides of Equation 4.18, gathering all terms associated with structural motion on the left side and premultiply by $\tilde{\boldsymbol{K}}_0^{-1}$ gives the following relation;

$$\boldsymbol{a}_\eta(\omega) = \hat{\boldsymbol{H}}_\eta(\omega) \cdot \boldsymbol{a}_{\hat{Q}}(\omega) \tag{4.22}$$

where $\hat{\boldsymbol{H}}_\eta(\omega)$ is the non-dimensional frequency-response matrix while $\boldsymbol{a}_\eta(\omega)$ and $\boldsymbol{a}_{\hat{Q}}(\omega)$ are the Fourier amplitudes of $\boldsymbol{\eta}(t)$ and $\hat{\boldsymbol{Q}}(t)$ respectively. The complete derivation of the frequency-response matrix is given in [6, 35]. The inverse of the frequency-response matrix is called the impedance matrix, and by studying the properties of this matrix any stability limit can be found. When a structure becomes unstable the response will increase rapidly, even for a small increase in the load. It is seen from Equation 4.22 that the response of the system becomes infinitely large when the elements of the frequency-response matrix becomes infinitely large, or when the value of the determinant to the impedance matrix reaches zero.

$$\left|\det\left(\hat{\boldsymbol{E}}_\eta(\omega, V)\right)\right| = 0 \tag{4.23}$$

The impedance matrix is defined as;

$$\hat{\boldsymbol{E}}_\eta(\omega, V) = \left\{ \boldsymbol{I} - \boldsymbol{\kappa}_{ae} - \left(\omega \cdot diag\left[\tfrac{1}{\omega_i}\right]\right)^2 + 2i\omega \cdot diag\left[\tfrac{1}{\omega_i}\right] \cdot (\boldsymbol{\zeta} - \boldsymbol{\zeta}_{ae}) \right\} \tag{4.24}$$

The determinant of the impedance matrix will give a solution with N_{mod} roots, each representing a stability limit. The solution will contain complex quantities, giving two conditions to be solved simultaneously;

$$\mathrm{Re}\Big(\det(\hat{\boldsymbol{E}}_\eta)\Big) = 0 \qquad \text{and} \qquad \mathrm{Im}\Big(\det(\hat{\boldsymbol{E}}_\eta)\Big) = 0 \tag{4.25}$$

The search of an instability limit will demand iterations, finding a critical velocity V_{cr} and the associated resonant (or critical) frequency ω_r. All of the eigen-value solutions will clearly give different stability limits, leaving the one with the lowest V_{cr} as the interesting solution. Flutter is a coupling of vertical and torsional motion leaving two modes of particular interest, one mode with a dominating ϕ_z component and the other containing a dominating ϕ_θ component. The impedance matrix may then be reduced to a 2 by 2 matrix, given as;

$$\begin{aligned}\hat{\boldsymbol{E}}_\eta(\omega_r, V_{cr}) = \Bigg\{ &\begin{bmatrix} 1 & 0 \\ 0 & 1 \end{bmatrix} - \begin{bmatrix} \kappa_{ae_{zz}} & \kappa_{ae_{z\theta}} \\ \kappa_{ae_{\theta z}} & \kappa_{ae_{\theta\theta}} \end{bmatrix} - \begin{bmatrix} (\omega_r/\omega_z)^2 & 0 \\ 0 & (\omega_r/\omega_\theta)^2 \end{bmatrix} \\ &+2i \begin{bmatrix} \omega_r/\omega_z & 0 \\ 0 & \omega_r/\omega_\theta \end{bmatrix} \cdot \begin{bmatrix} \zeta_z - \zeta_{ae_{zz}} & -\zeta_{ae_{z\theta}} \\ -\zeta_{ae_{\theta z}} & \zeta_\theta - \zeta_{ae_{\theta\theta}} \end{bmatrix} \Bigg\}\end{aligned} \tag{4.26}$$

Here, using that the two modes can be simplified to;

$$\left.\begin{aligned} \boldsymbol{\varphi}_1(x) &\approx \begin{bmatrix} 0 & \phi_z & 0 \end{bmatrix}^T \\ \boldsymbol{\varphi}_2(x) &\approx \begin{bmatrix} 0 & 0 & \phi_\theta \end{bmatrix}^T \end{aligned}\right\} \tag{4.27}$$

The modes has the corresponding natural frequencies $\omega_1 = \omega_z$ and $\omega_2 = \omega_\theta$, modal damping ratios $\zeta_1 = \zeta_z$ and $\zeta_2 = \zeta_\theta$, and modal mass given as $\tilde{m}_1 = \tilde{m}_z$ and $\tilde{m}_2 = \tilde{m}_\theta$. The elements of the impedance matrix are;

$$\kappa_{ae_{zz}} = \frac{\rho B^2}{2\tilde{m}_z}\left(\frac{\omega_z(V)}{\omega_z}\right)^2 H_4^* \frac{\int_L^{L_{exp}} \phi_z^2 dx}{\int_L \phi_z^2 dx} \qquad \kappa_{ae_{z\theta}} = \frac{\rho B^3}{2\tilde{m}_z}\left(\frac{\omega_z(V)}{\omega_z}\right)^2 H_3^* \frac{\int_L^{L_{exp}} \phi_z \phi_\theta dx}{\int_L \phi_z^2 dx} \tag{4.28}$$

$$\kappa_{ae_{\theta\theta}} = \frac{\rho B^4}{2\tilde{m}_\theta}\left(\frac{\omega_\theta(V)}{\omega_\theta}\right)^2 A_3^* \frac{\int_L^{L_{exp}} \phi_\theta^2 dx}{\int_L \phi_\theta^2 dx} \qquad \kappa_{ae_{\theta z}} = \frac{\rho B^3}{2\tilde{m}_\theta}\left(\frac{\omega_\theta(V)}{\omega_\theta}\right)^2 A_4^* \frac{\int_L^{L_{exp}} \phi_\theta \phi_z dx}{\int_L \phi_\theta^2 dx} \tag{4.29}$$

$$\zeta_{ae_{zz}} = \frac{\rho B^2}{4\tilde{m}_z}\frac{\omega_z(V)}{\omega_z} H_1^* \frac{\int_L^{L_{exp}} \phi_z^2 dx}{\int_L \phi_z^2 dx} \qquad \zeta_{ae_{z\theta}} = \frac{\rho B^3}{4\tilde{m}_z}\frac{\omega_z(V)}{\omega_z} H_2^* \frac{\int_L^{L_{exp}} \phi_z \phi_\theta dx}{\int_L \phi_z^2 dx} \tag{4.30}$$

$$\zeta_{ae_{\theta\theta}} = \frac{\rho B^4}{4\tilde{m}_\theta}\frac{\omega_\theta(V)}{\omega_\theta} A_2^* \frac{\int_L^{L_{exp}} \phi_\theta^2 dx}{\int_L \phi_\theta^2 dx} \qquad \zeta_{ae_{\theta z}} = \frac{\rho B^3}{4\tilde{m}_\theta}\frac{\omega_\theta(V)}{\omega_\theta} A_1^* \frac{\int_L^{L_{exp}} \phi_\theta \phi_z dx}{\int_L \phi_\theta^2 dx} \tag{4.31}$$

Flutter can only occur if the off diagonal terms of Equation 4.26 on the preceding page are unequal to zero. When the diagonal terms are zero, stability problems describing motion in either vertical direction (galloping) or in torsion (static divergence or dynamic instability in torsion) may be identified from the first or second row of Equation 4.26 on the facing page. The following dimensionless coefficients are introduced to simplify further calculations;

$$\psi_{z\theta} = \frac{\int_L^{L_{exp}} \phi_z \phi_\theta dx}{\int_L \phi_z^2 dx}\frac{\int_L^{L_{exp}} \phi_z \phi_\theta dx}{\int_L \phi_\theta^2 dx} \quad \beta_z = \frac{\rho B^2}{\tilde{m}_z} \quad \beta_\theta = \frac{\rho B^4}{\tilde{m}_\theta} \quad \gamma = \frac{\omega_\theta}{\omega_z} \quad \text{and} \quad \hat{\omega}_r = \frac{\omega_r}{\omega_\theta} \tag{4.32}$$

The coefficient $\psi_{z\theta}$ is a measure of the shape-wise similarity of the vertical and torsional mode, where a value of unity describing two mode shapes that are identical, and on the other hand dissimilar shapes as the value reaches zero. Shape-wise dissimilarity clearly means that the off diagonal terms of Equations 4.28-4.31 equals zero, and static divergence or galloping may occur. $\hat{\omega}_r$ is the reduced resonant frequency or the reduced critical frequency when flutter occur. In the case of flutter the frequency of vertical and torsional motion equals the resonant frequency, $\omega_z = \omega_\theta = \hat{\omega}_r$. Solving the determinant of real and complex part of the impedance matrix, see Equation 4.25 on the preceding page, gives the two following equations;

$$R_4\hat{\omega}_r^4 + R_3\hat{\omega}_r^3 + R_2\hat{\omega}_r^2 + 1 = 0 \tag{4.33}$$

$$I_3\hat{\omega}_r^3 + I_2\hat{\omega}_r^2 + I_1\hat{\omega}_r + \zeta_z\gamma + \zeta_\theta = 0 \tag{4.34}$$

The real and imaginary coefficients are expressed as follows [8, 26, 35];

$$
\begin{aligned}
R_4 &= \gamma^2 \left[1 + \tfrac{\beta_z}{2} H_4^* + \tfrac{\beta_\theta}{2} A_3^* + \tfrac{\beta_z \beta_\theta}{4} \left(A_1^* H_2^* \psi_{z\theta} - A_2^* H_1^* + A_3^* H_4^* - A_4^* H_3^* \psi_{z\theta} \right) \right] \\
R_3 &= \gamma \left(\zeta_\theta \beta_z \gamma H_1^* + \zeta_z \beta_\theta A_2^* \right) \\
R_2 &= -\left(1 + \gamma^2 + 4\gamma \zeta_z \zeta_\theta + \frac{\beta_z}{2} \gamma^2 H_4^* + \frac{\beta_\theta}{2} A_3^* \right)
\end{aligned} \tag{4.35}
$$

$$
\begin{aligned}
I_3 &= \gamma^2 \left[\tfrac{\beta_z \beta_\theta}{8} \left(H_1^* A_3^* - H_2^* A_4^* \psi_{z\theta} - H_3^* A_1^* \psi_{z\theta} + H_4^* A_2^* \right) + \tfrac{1}{4} \left(\beta_z H_1^* + \beta_\theta A_2^* \right) \right] \\
I_2 &= -\left[\zeta_z \left(\tfrac{\beta_\theta}{2} A_3^* + \gamma \right) + \zeta_\theta \gamma^2 \left(\tfrac{\beta_z}{2} H_4^* + 1 \right) \quad \right] \\
I_1 &= -\frac{1}{4} \left(\beta_z \gamma^2 H_1^* + \beta_\theta A_2^* \right)
\end{aligned} \tag{4.36}
$$

Usually, Equation 4.33 and 4.34 are solved graphically by choosing values of the reduced velocity, and finding the corresponding roots $\hat{\omega}_r$ when the equations equals zero. The instability limit is found where the real and imaginary roots cross each other. The root providing the lowest critical velocity is identified as the critical frequency. The critical velocity is found from solving the equation below. The resonant frequency ω_r is henceforth referred to as the critical frequency $\hat{\omega}_{cr}$

$$
\begin{aligned}
& \frac{V_{cr}}{\omega_\theta B} = \frac{V_{cr}}{\omega_{cr} B} \cdot \hat{\omega}_{cr} = V_{cr,red} \cdot \frac{\omega_{cr}}{\omega_\theta} \\
\implies \quad & V_{cr} = V_{cr,red} \cdot \hat{\omega}_{cr} \cdot \omega_\theta \cdot B
\end{aligned} \tag{4.37}
$$

4.4 General eigenvalue problem

The flutter equations presented in Section 4.3 by Equations 4.33 - 4.34 were derived by the assumption that coupling of only two modes contributes to the calculations of any instability. Solving the determinant of the real and imaginary part of the impedance matrix gives no direct physical interpretation. When solving an eigenvalue problem, the solution is dependent on the number of modes chosen to describe the problem with sufficient accuracy. As before the structural displacements are represented with generalized coordinates and natural eigen-modes, $\boldsymbol{r}(x,t) = \boldsymbol{\Phi}(x) \cdot \boldsymbol{\eta}(t)$ which gives an exactly representation when all the structural modes are included. Introducing this relation into the equation of motion, considering only aerodynamic forces, and premultiplying by the modal mass matrix $\tilde{\boldsymbol{M}}_0$ the equilibrium equation is given by;

$$\ddot{\boldsymbol{\eta}} + \tilde{\boldsymbol{M}}_0^{-1}\boldsymbol{\Phi}^T(\boldsymbol{C}_0 - \boldsymbol{C}_{ae})\boldsymbol{\Phi}\cdot\dot{\boldsymbol{\eta}} + \tilde{\boldsymbol{M}}_0^{-1}\boldsymbol{\Phi}^T(\boldsymbol{K}_0 - \boldsymbol{K}_{ae})\boldsymbol{\Phi}\cdot\boldsymbol{\eta} = 0$$
$$\implies \quad \ddot{\boldsymbol{\eta}} + \tilde{\boldsymbol{M}}_0^{-1}(\tilde{\boldsymbol{C}}_0 - \tilde{\boldsymbol{C}}_{ae})\dot{\boldsymbol{\eta}} + \tilde{\boldsymbol{M}}_0^{-1}(\tilde{\boldsymbol{K}}_0 - \tilde{\boldsymbol{K}}_{ae})\cdot\boldsymbol{\eta} = 0 \tag{4.38}$$

The characteristic solution of the homogeneous equation above is given as;

$$\boldsymbol{\eta} = \hat{\boldsymbol{\eta}}e^{\lambda_n t} \tag{4.39}$$

where $\hat{\boldsymbol{\eta}}$ is the amplitude vector. Introducing this solution into Equation 4.38 gives the following quadratic eigenvalue problem;

$$\left(\lambda_n^2 + \lambda_n\tilde{\boldsymbol{M}}_0^{-1}\left(\tilde{\boldsymbol{C}}_0 - \tilde{\boldsymbol{C}}_{ae}(V,\omega)\right) + \tilde{\boldsymbol{M}}_0^{-1}\left(\tilde{\boldsymbol{K}}_0 - \tilde{\boldsymbol{K}}_{ae}(V,\omega)\right)\right)\hat{\boldsymbol{\eta}} = 0, \qquad n = 1, 2, ..., 2N \tag{4.40}$$

As before, $\tilde{\boldsymbol{M}}_0$, $\tilde{\boldsymbol{C}}_0$ and $\tilde{\boldsymbol{K}}_0$ denotes the N_{mod} by N_{mod} modal mass matrix, modal damping matrix and modal stiffness matrix respectively. $\tilde{\boldsymbol{C}}_{ae}(V,\omega)$ and $\tilde{\boldsymbol{K}}_{ae}(V,\omega)$ stands for aerodynamic modal damping matrix and aerodynamic modal stiffness matrix respectively. $\tilde{\boldsymbol{C}}_{ae}(V,\omega)$ and $\tilde{\boldsymbol{K}}_{ae}(V,\omega)$ are functions of the oscillation frequency ω, the wind velocity V as well as the aerodynamic derivatives, see Equation 4.14 on page 27. It can be shown that Equation 4.40 may be written as a complex eigenvalue problem given by, see Appendix A.6 and [28];

$$(\mathbf{A} - \lambda\mathbf{I})\hat{\boldsymbol{\psi}} = 0 \tag{4.41}$$

where $\hat{\boldsymbol{\psi}} = [\lambda_n\hat{\boldsymbol{\eta}}^T \quad \hat{\boldsymbol{\eta}}^T]^T$, and $\boldsymbol{A}$ is given as;

$$\boldsymbol{A} = \begin{bmatrix} -\tilde{\boldsymbol{M}}_0^{-1}(\tilde{\boldsymbol{C}}_0 - \tilde{\boldsymbol{C}}_{ae}) & -\tilde{\boldsymbol{M}}_0^{-1}(\tilde{\boldsymbol{K}}_0 - \tilde{\boldsymbol{K}}_{ae}) \\ \boldsymbol{I} & \mathbf{0} \end{bmatrix} \tag{4.42}$$

$\boldsymbol{I}$ is the N_{mod} by N_{mod} identity matrix, while $\mathbf{0}$ is a N_{mod} by N_{mod} matrix containing only zeros. The solution gives $2N$ eigenvalues λ_n and corresponding eigenvectors $\hat{\boldsymbol{\psi}}$. N is equal to the number of modes included in the eigenvalue problem. Each of the N complex couples of conjugated eigenvalues can be written as $\lambda_n = \mu_n \pm i\omega_D$, where $\omega_D = \omega_n\sqrt{1 - v_n^2}$ is the damped circular frequency. $\mu_n = -v_n\omega_n$ where $v_n = -Re(\lambda_n)/\omega_n$ is the damping ratio including both structural and aerodynamic damping. i is the imaginary unit. If μ_n is negative (positive damping ratio) the system exhibit positive damping and the solution converges exponentially (decay oscillation). On the other hand, when μ_n is positive (negative damping ratio), the damping becomes negative and the solution diverges and the response becomes infinitely large. I.e. when the real part of the complex conjugated eigenvalues turn to a positive value ($\mu_n < 0$) the system has reached a critical

stage, identified as a stability limit. The wind velocity associated with this critical value is termed the critical velocity. The associated frequency is termed the resonant or the critical frequency. Since the flutter derivatives are functions of the frequency of motion and the wind velocity, the eigenvalue problem has to be solved by an iterative process. A solution of the eigenvalue problem will give a better understanding of the problem since one can follow the development of the frequency and damping as the wind velocity increases. Further descriptions of the eigenvalue problem is given in [2, 28]

Chapter 5

Finite element model

5.1 Introduction

Based on preliminary calculations carried out in Chapter 3, a finite element model has been created in order to find natural frequencies and mode shapes of the bridge. The model is based on the finite element method, henceforth referred to as FEM, and created by applying the computer program $ABAQUS$ [34]. $ABAQUS$ is an advanced tool and can be used to model the simplest problems to the more demanding ones. The program is suitable for static as well as dynamic problems and provides a good user interface, making it well suited for most users regardless of simulation expertise. $ABAQUS$ can solve nonlinear as well as linear problems, but in this thesis only linear behaviour is accounted for. I.e. linear material behaviour is assumed. The cables of suspension bridges are highly non-linear elements. They can have large displacement even if the strains are small (non-linear geometry). The geometric stiffness is the most important non-linearity of suspension bridges since the bending stiffness of the cables practically equals zero. This non-linear effect can be taken into account by specifying the $NLGEOM$ option in $ABAQUS$. The geometric stiffness of the cables will then be updated as the loading is applied to the model. The first step in creating a model is to create the parts to be included in the simulation. Elements and nodes build up the parts. The elements will then be assigned properties such as stiffness and material properties. When all the necessary parts are created, they are assembled together to one model to be included in the simulation. As the last step boundary conditions, loads and other properties may be assigned to the model before the analysis type is chosen. In this thesis a *static* analysis will be used when applying load to the model, while an *eigenvalue* analysis will be used to extract natural frequencies and mode shapes.

5.2 The ABAQUS model

The FEM-model is be based on calculations and geometry presented in Chapter 3. The origin in the FEM-model is chosen to be in the shear center of the western girder on the Lavik side, referred to as North (N), where the girders are supposed to be supported by the pylons. The other end of the girders are supposed to be connected to the pylons on Oppedal side, referred to as South (S). The axis parallel with the girders is denoted the x-axis, positive from North to South. The vertical axis is denoted the y-axis and positive in the upward direction. The horizontal lateral axis is denoted the z-axis and positive to the East. As the preliminary design showed the main cable sag has been chosen to be

$k_m = 370\ m$, and are connected to the pylon tops at a vertical distance 402.3 m from the origin. The two girders are connected with crossbeams at intermediate distance 20 m along the span. The intermediate distance between hangers in one plane is also chosen to be 20 m and are connected to the outer top edge of the girders. An illustration of the geometry and coordinates used in *ABAQUS* is shown in Figure 5.1. The geometry of the backstay cables has been varied during the analysis, but as a reference geometry the projected height and length has been chosen as $l_{bs} = 350\ m$ and $h_{bs} = 140\ m$ respectively. The curvature of the girders are modelled as presented in Section 3.1 on page 9, with a maximum elevation 30.3 m of the shear centre in the girders, referred to the origin.

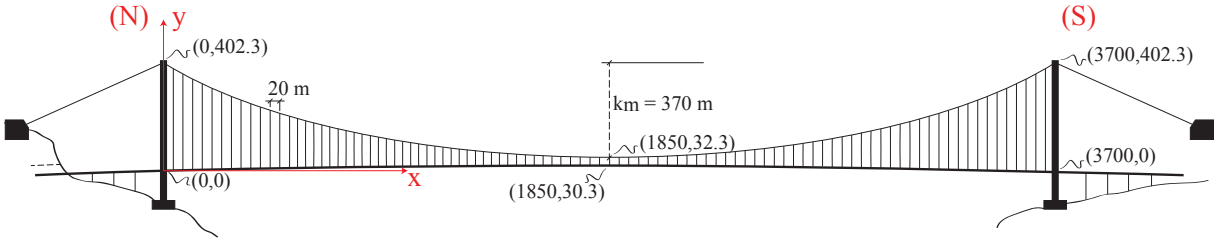

Figure 5.1: Coordinates and geometry used to model the bridge in *ABAQUS*. Red arrows show the vertical y-axis and longitudinal x-axis.

5.3 Parts in the FEM-model: Geometry and properties

5.3.1 Stiffening girder

As presented in the preliminary design section, a separated box-girder has been chosen as the stiffening girder. Thus, the stiffening girder will consist of two symmetric longitudinal and identical girders spanning from (N) to (S). The girders are modelled as two continuous beams with the mass and stiffness properties presented in Section 3.3 on page 11, extracted from *CrossX* (see Appendix B.1) and repeated for convenience below. The girders are given a generalized section assignment which means that the values below are implemented and *ABAQUS* calculates the mass and the mass moment of inertia. *ABAQUS* then renders a generalized beam section with properties equal to those of the real section, as shown in Figure 5.2 on the next page.

- Area: $A = 0.53175m^2$
- Second moment of inertia:
  - $I_y = 6.1704m^4$
  - $I_z = 0.37967m^4$
- Torsional moment of inertia: $I_t = 0.99314 * 10^{11}m^4$

- Material density: ρ =7850 kg/m^3
- Location of shear centre:
  - $y_s = 0.0136\ m$
  - $z_s = 0.0488\ m$

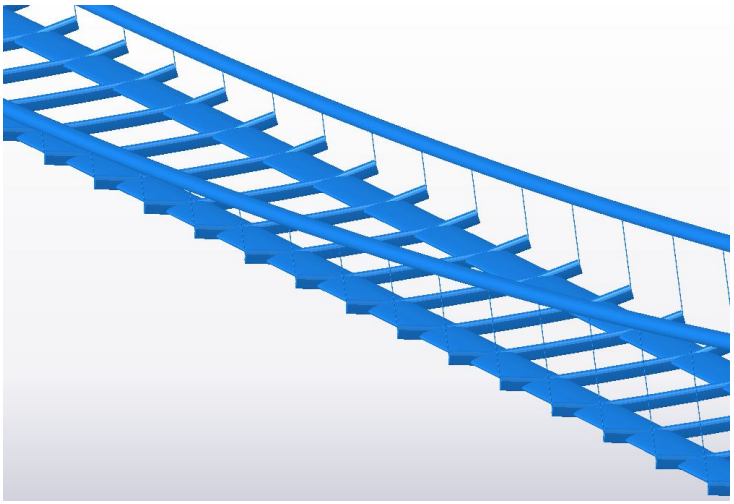

Figure 5.2: Rendered beam profiles in the finite element model.

The hangers are connected to the outer edges of the girders. In order to model the hangers as vertical elements, fictitious beams are modelled stretching from the shear centre in the girders to the points where the hangers are connected to the girders. Dummy nodes are introduced to model the connection between the hangers and girders. The same procedure is followed when modelling the connection between the two box-girders and the crossbeams. Two fictitious beams stretching from the shear centres to the points where the crossbeam is welded to the girders. The fictitious beams are modelled as stiff members with practically zero mass. Figure 5.3 on the following page shows the principles of this modelling technique where the cross section is modelled as an own part. This configuration is repeated for every 20 meters along the span. Blue circles specifies the shear centre of the girders where distributed mass and MOI of additional masses has been lumped and added. The cross section has been modelled in a local coordinate system, (x', y'), and transformed to the global coordinate system in the assembly. The girders are modelled as a second order polynomial by specifying the supporting end points and the maximum elevation point at the midpoint of the bridge. As for the girders, the crossbeams are given a generalized section assignment by implementing the values extracted from modelling the beams in $CrossX$, see Appendix B.2.

The approximate element size in the stiffening girder is chosen as 10 m. The type of element chosen for the girders, fictitious beams and crossbeams are $B33$ elements, a 2-node beam element with a cubic formulation. This element do not account for shear flexibility (Euler Bernoulli beam theory) but are effective for modeling frame structures with slender

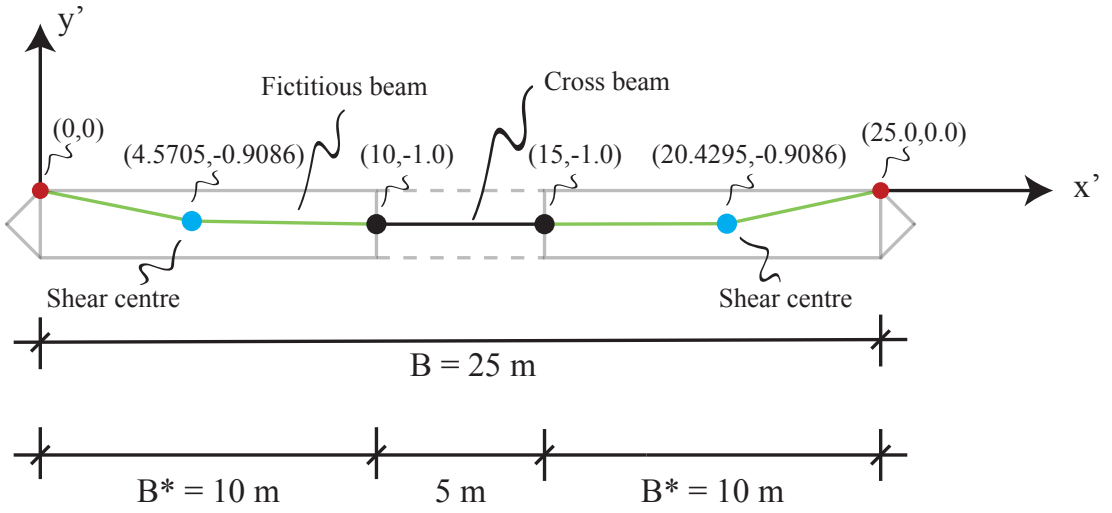

Figure 5.3: Cross section of girder. The cross section is modeled as an own part. Red circles refer to the dummy nodes connecting the lower hanger attachments to the edge of the girders. Blue circles refers to the shear centre in the girders, where also additional mass and MOI has been added. Green lines refer to the fictitious stiff beams with zero mass. Black circles refer to nodes representing the welded connection between the crossbeam and girders. All dimensions are given in m.

members. This element was found to give accurate natural frequencies compared to e.g. a $B21$ element, a 2-node linear beam member with shear deformations [34]. The findings are based on an analysis carried out on a simply supported beam with cross sectional height and width equal to 1 m and 3 m respectively. The length is chosen as $L = 20$ m. The cross sectional properties are given below, and the element length is chosen as 0.5 m.

- $I_y = 2.25\ N/m^2$
- $I_z = 0.25\ N/m^2$
- $I_t = 0.78999\ N/m^2$
- $A = 3\ m^2$
- $m = 23{,}550\ kg/m$

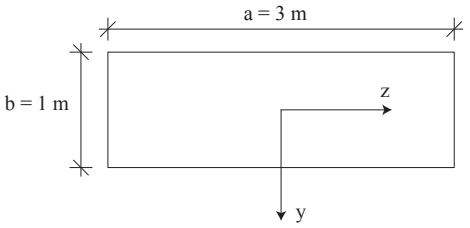

The analytical expression for the horizontal and vertical frequency for mode n is given as [6];

$$\omega_n = \frac{n^2\pi^2}{L^2}\sqrt{\frac{EI}{m}} \tag{5.1}$$

Results from the analysis is given in Table 5.1 on the next page where the vertical, horizontal and torsional frequencies extracted from $ABAQUS$ are compared to the analytical values. The analytic torsional frequency has not been presented, therefore the percent-

age difference of the analysis using $B21$ elements has been given compared to the analysis using $B33$ elements. As can be seen the analysis using $B33$ elements give accurate frequencies compared with $B21$ elements, especially for lateral horizontal modes. Both elements seem to give approximately the same torsional frequencies, but the difference increases for higher modes. Based on these findings, $B33$ elements are used. An approximate element size of 10 m is used for the stiffening girder.

Table 5.1
Natural frequencies given for a simply supported beam. The simulated values for different element formulations are compared with the analytical values given for vertical and lateral horizontal modes. V refers to the vertical modes, LH refers to the lateral horizontal modes, T refers to torsional modes and H refers to the longitudinal horizontal mode.

Mode nr.	Mode description	Analytical (rad/s)	B33 (rad/s)	Error %	B21 (rad/s)	Error %
1	1st V	36.8	36.8	0.0	36.7	-0.4
2	1st LH	110.5	110.5	0.0	106.6	-3.5
3	2nd V	147.4	147.4	0.0	145.0	-1.6
4	1st T		284.2		284.0	-0.1
5	3rd V	331.6	331.6	0.0	320.0	-3.5
6	1st H		406.2		406.2	0.0
7	2nd LH	442.1	442.1	0.0	389.6	-11.9
8	2nd T		568.9		567.7	-0.2
9	4th V	589.4	589.5	0.0	554.6	-5.9
10	3rd T		854.4		850.4	-0.5
11	5th V	921.0	921.0	0.0	840.4	-8.8
12	3rd LH	994.7	994.7	0.0	780.3	-21.6

5.3.2 Cables

The main span cables has been modelled as curves describing a second order polynomial based on the geometry given in Figure 5.1 on page 36, by specifying three points on the curve. The lowest point on the curve is where the hangers are shortest, i.e. at midpoint of the bridge 2 m above the top plate of the girders. $B33$ elements have been used to model the cables, and the approximate element size is chosen to be 10 m. The equation of the cable is given as follows, when specifying the origin in accordance with Figure 5.1;

$$y_m = \frac{4k_m}{l_m} x \left(\frac{x}{l_m} - 1 \right) + 402.3 \tag{5.2}$$

The hangers are connected to the cables at nodes with a horizontal distance of 20 m along the cable. The backstay cables have been modelled as straight elements, and have been varied in different analysis. An approximate element size of 10 m has been chosen for the main span cables, while for the backstay cables six elements has been chosen along each

cable. To insure that the cables are simulated with a small bending stiffness, the cable area has been calculated such that the stiffness is 10 % of a circle with outer diameter equal to 1 m found from the preliminary design. The second moment of area of a circle with diameter 1 m is given as $I_0 = \pi/64 \cdot D^4$, where D is the diameter. The new stiffness is then found to be;

$$I_{new} = 0.1 \cdot I_0 = 4.909 \cdot 10^{-3} m^4 \tag{5.3}$$

which gives a diameter of $D_{new} = 0.5623$ m. The new elasticity modulus may then be calculated by the following equation, assuming a modulus of elasticity equal to $E =$ 205,000 N/mm^2;

$$E_{new} = \frac{EA}{A_{new}} = 6.483 \cdot 10^{11} N/m^2 \tag{5.4}$$

The new density is then found when using the distributed mass, $m = 6165.38$ kg/m, along the cable found from Equation 3.27;

$$\rho_{ny} = \frac{m}{A_{new}} = 24,827.5 kg/m \tag{5.5}$$

5.3.3 Hangers

As for the cables the hangers has been given a stiffness 10 % of a circle with outer diameter 0.05 m found from the preliminary design. This gives a diameter of $D_{ny} = 0.028$ m. Assuming, for simplicity, a modulus of elasticity $E = 205{,}000$ N/mm^2 gives a modified modulus of elasticity and density equal to that of the cables, see above. The modulus of elasticity is usual 160,000 N/mm^2 but results will not be affected significantly by using a higher value. The hangers are modelled with one element for each hanger stretching from the cable to the dummy nodes connecting them to the girders. $B33$ elements are used for the hangers.

5.3.4 Pylons

In this thesis the pylons has been disregarded in the simulations and in the preliminary design. This has been done because the primary purpose of the towers are to transfer the vertical cable forces at the pylon top down to the ground, while the anchor blocks and the backstay cable transfers the horizontal forces to the ground. The design process of the pylons has been considered to time consuming and is left for further investigations. This may have some effect on the simulation results, but they are regarded insignificant in this thesis.

Table 5.2 on the next page below summarize the properties of the different components of the bridge. I_1 denotes the second moment of area about the strong axis, while I_2 denotes the second moment of area about the weak axis. Other parameters used during analysis are listed below.

- Thermal expansion coefficient: $\alpha = 1.2E^{-5}\ 1/K$
- Gravity acceleration: 9.81 m/s^2

Table 5.2
Equivalent properties of bridge elements in *ABAQUS*. Not all values needs to be implemented.

Bridge component	Properties						
	$\rho\ (kg/m)$	$A\ (m^2)$	$D\ (m)$	$I_1\ (m^4)$	$I_2\ (m^4)$	$I_t\ (m^4)$	$E\ (N/m^2)$
Crossbeams	7,850	0.08630		0.0456	0.00778	0.02153	$2.05 \cdot 10^{11}$
Girders	7,850	0.53175		6.1704	0.37967	0.99314	$2.05 \cdot 10^{11}$
Cables	24,827.5	0.24833	0.562	$4.909 \cdot 10^{-3}$	$4.909 \cdot 10^{-3}$		$6.483 \cdot 10^{11}$
Hangers	24,827.5	$6.158 \cdot 10^{-4}$	0.028	$3.068 \cdot 10^{-8}$	$3.068 \cdot 10^{-8}$		$6.483 \cdot 10^{11}$

5.3.5 Boundary conditions and interactions

The boundary conditions have been changed in different analysis to see how this effects the results for natural frequencies and mode shapes. The boundary conditions for the cables are the same in all analysis that has been carried out. The boundary condition for a reference analysis is given in the list below. To model the connections between the girders and fictitious beams in the cross section, an option called TIE is specified in each of these points. This option creates a constraint where all translational and rotational degree of freedoms of two nodes will be the same. I.e. the connection represents a moment stiff connection. The same option is used where the lower hanger attachments are connected to the dummy nodes of the girders.

- Girder supports: The girders are simply supported at each end, i.e. translational degree of freedoms are prevented. No rotational degree of freedoms prevented.
- Cables at pylon top: In the points where the pylon tops should be, the translational degree of freedoms in lateral horizontal direction and vertical direction are prevented. I.e. the cables are free to move in longitudinal direction, and also free to rotate.
- Backstay anchor: All translational degree of freedoms are prevented.

5.3.6 Main geometrical characteristics

The main geometrical characteristics of the bridge are summed up in Table 5.3 on the following page.

Table 5.3
Main geometrical characteristics of the bridge.

Main span length	$l_m = 3{,}700\ m$
Tower height from origin	$h_t = 402{,}3\ m$
Height from sea level to girders	$h_g = 75\ m$
Main cable sag	$k_m = 370\ m$
Number of hangers in main span	$n_h = 370$
Girder width	$B^* = 10.0\ m$
Girder height	$D = 2.0\ m$
Shortest hanger	$l_{h,min} = 2\ m$
Distance between cable planes	$B = 25\ m$

5.4 Applying load

Since a suspension bridge is a relatively flexible structure and the only stiffness in the cables are the geometric stiffness, non-linear geometry must be used. In all the analysis steps, non-linear geometry is taken into account by the *NLGEOM* option. This implies that the deformations are considered in every load increment, and insures that the geometric stiffness is introduced in the cables.

5.4.1 Modeling of mass

In addition to the mass and *MOI* from the stiffening girder itself, the mass and *MOI* (or rotary inertia) of non-constructional elements must be added to the model. These elements contribute significantly and affect the mass matrix. Such elements are e.g. asphalt, railing, lower hanger attachments etc. They have been mentioned in Chapter 3 where the distributed mass and *MOI* were found. The additional values must be specified as point mass (or lumped mass) with specification of the *MOI* about the three coordinate axises. The values given in Table 3.1 on page 18 are distributed values along one girder. They are repeated for convenience in Table 5.4 on the facing page where also the total lumped mass and *MOI* has been calculated. The total mass is found by multiplying the distributed mass by 20 m. The *MOI* about the longitudinal axis, I_{11} is found by multiplying the distributed value by 20 m. The total *MOI* about the vertical and lateral axis, I_{22} and I_{33} respectively is found by applying the formula $I = 1/12 \cdot m \cdot L^3$, where L is the distance between the hangers in one plane. Bold values are specified in each of the part illustrated in Figure 5.3 on page 38 , and in each of the two shear centres indicated by blue circles. I.e. the bold values are specified at every 20 m along the girder, and in each of the two parallel girders.

An alternative procedure has also been tested in one of the analysis. Instead of modelling the girders as continuous generalized beams with mass, they have also been modelled as massless beams but with the mass specified as lumped mass every 20 m and with rotary inertia as described above. This has been done in order to see if the results change

Table 5.4
Mass and MOI of non constructional elements added in the FEM-model. Bold values are implemented in the model. I_{11}: MOI about the x-axis. I_{22}: MOI about the y-axis. I_{33}: MOI about the z-axis.

Additional elements	Mass m (kg/m)	M (kg)	I'_{11} (kgm^2/m)	I_{11} (kgm^2)	I_{22} (kgm^2)	I_{33} (kgm^2)
Transvers bulkheads	494.6	9,892.0	5,167.0	103,340.0	329,733.3	329,733.3
Asphalt	1,631.0	32,620.0	14,507.1	290,142.0	1,087,333.3	1,087,333.3
Railing	153.0	3,060.0	1,515.3	30,306.0	102,000.0	102,000.0
Lower hanger attachment	43.0	860.0	954.1	19,082.0	28,666.7	28,666.7
Total	2,321.6	**46,432.0**	22,143.5	**442,870.0**	**1,547,733.3**	**1,547,733.3**

significantly. Table 5.5 shows the values implemented when this procedure has been followed.

Table 5.5
Mass and MOI of girder elements added in the FEM-model. Bold values are implemented in the model. I_{11}: MOI about the x-axis. I_{22}: MOI about the y-axis. I_{33}: MOI about the z-axis.

Additional elements	Mass m (kg/m)	M (kg)	I'_{11} (kgm^2/m)	I_{11} (kgm^2)	I_{22} (kgm^2)	I_{33} (kgm^2)
Longitudinal steel	4,173.4	83,468.0	51,454.9	1,029,098.0	2,782,266.7	2,782,266.7
Transvers bulkheads	494.6	9,892.0	5,167.0	103,340.0	329,733.3	329,733.3
Asphalt	1,631.0	32,620.0	14,507.1	290,142.0	1,087,333.3	1,087,333.3
Railing	153.0	3,060.0	1,515.3	30,306.0	102,000.0	102,000.0
Lower hanger attachment	43.0	860.0	954.1	19,082.0	28,666.7	28,666.7
Total	6,495.0	**129,900.0**	73,598.4	**1,471,968.0**	**4,330,000.0**	**4,330,000.0**

5.4.2 Dead load

The geometry modelled in the FEM-model is equal to the geometry in real life with all dead load acting on the bridge. The only real load given to the model is the gravity force. When introducing the gravity force in the model, the bridge will deform and the sag of the cables will be larger. At the same time the deformation in the main span will cause displacements where the main span cable and backstay cable meet (at pylon top). Introducing a fictitious contraction force in the cable system by applying a negative temperature field throughout the cables counteracts these deformations. Several attempts have been carried out in order to get the geometry equal to the initial. The final model was found to have a geometry that deviated slightly from the initial but this have been considered negligible.

The total mass of the bridge extracted form $ABAQUS$ was found to be;

$$M_{tot,ABQS} = 1.055 \cdot 10^8 kg = 105,529 ton = 1.035 \cdot 10^6 kN \tag{5.6}$$

Subtracting the weight of the backstay cables, the weight of the main span in the FEM-model is approximated to be, with a projected height and length of the backstay cables as 140 and 350 respectively;

$$M_{main} = 105,529 ton - \sqrt{140^2 + 350^2} * 6165.4 \cdot 4/1000 ton = 96,233 ton \tag{5.7}$$

This is about 0.2 % higher then the value found from analytical calculation, see Table 3.3 on page 22. This may be due to some inaccuracy in geometry and mass specified in the model but this difference is of no significant importance. The maximum force in the cables are found from $ABAQUS$ where the backstay cables and main span cables meet;

$$T_{max} = 629266 kN \tag{5.8}$$

This will give a stress in the cables equal to;

$$\sigma = \frac{T_{max}}{A_{cable}} = 801.2 MPa \tag{5.9}$$

The maximum tension force given in Equation 3.33 on page 22, T_{max} = 636,099 kN, gave a stress of $\sigma = 809.9 MPa$. This is only about 1 % higher and confirms that the finite element mode agrees well with the theoretical calculations. The load/capacity ratio when using the nominal tensile strength, F_{Rd} = 1,850 MPa, will then be 43.3 %.

5.4.3 Other loading

In this thesis the focus has been on the aeroelastic stability limit in strong wind found by a frequency domain approach. Any response calculations have not been considered, i.e. only the static loading mentioned above has been introduced in the model. Other loading such as earthquake loads, traffic loads and wind loads has not been introduced in the model, but must be part of further investigations. Vortex shedding is an important phenomenon that occurs at lower wind speeds due to interaction between the bridge girder and the wind flow. This phenomenon will not cause structural failure since the oscillations are self-destructive, but may cause unacceptably large oscillations in a serviceability state and are also left for further investigations.

Chapter 6

Results from Finite element model

The main purpose of the finite element model is to find the mode shapes and the corresponding natural frequencies obtained from a zero wind case. These outputs are essential in order to calculate the stability limit of the suspension bridge where the mode shapes and frequencies goes directly into the equation system presented in Section 4.4. In the ABAQUS model it's easy to change parameters and see how these changes effects the results. In the following these changes are analysed and described more thoroughly.

The mode shapes can be categorized into symmetric and antisymmetric (asymmetric) modes. The symmetric modes are symmetric about the midpoint of the bridge, while the asymmetric modes are unsymmetrical about the midpoint. The modes of the bridge are represented by horizontal (lateral) and vertical deformations as well as deformations due to rotation of the girder about the longitudinal axis (x-axis). In the ABAQUS model nodes in the middle of every crossbeam has been chosen as points where displacements and rotations are extracted.

In order to compare displacements due to torsional rotation of the girder with vertical and lateral displacements, the rotations about the x-axis has been multiplied with half the width between the cable planes. Asymmetric modes can be identified as modes that meet the condition $\int_0^l w dx = 0$ in the cables and produces no overall additional tension in the cables. Here, w is the distributed weight of the cable and l is the length of the span [13].In symmetric modes additional tension will be produced in the cables. The displacements calculated in ABAQUS in an eigenvalue analysis have been normalized such that the maximum displacement in the bridge is set to unity. A pure torsional motion of the girder will then be identified with a vertical displacement at the end of the girder, or vertical displacement of the cables, equal to ± 1.Some modes presented in the following shows displacements of the girder lower than ± 1, which means that the maximum displacement will occur in the cables, or the pylons if they where modelled.

6.1 Discription of analysis

Several analyses have been carried out to see the effects on the natural frequencies and mode shapes. The reference analysis is identified as a total symmetric model where the boundary conditions of the girder are equal on both sides. The mode shapes presented in the following are extracted from the reference run since this configuration will show displacements that are symmetric in absolute value about the midpoint on the bridge. The different analyses are shortly presented below.

Analysis 1: Reference analysis. Girder is fixed in all translational degree of freedoms (DOFs). The girders are free to rotate about all axes. At the points where the pylon tops should be, the translational DOF in the longitudinal direction is free. The backstay cables are modelled with an initial slope at the pylon top equal to that of the main span cable. The vertical projected height from the end supports of the backstay cables to the pylon top supports has been chosen as 140 m.

Analysis 2: Same configuration as the reference run but with modified end supports of the girder. The girder supports at Oppedal side are free to move in longitudinal direction. This configuration is often used in bridges to prevent compression forces due to a thermal expansion of the girder. This will affect the stiffness of the bridge as the girder becomes more flexible.

Analysis 3: Same configurations as the reference run, but rotational DOFs about the lateral axis (z-axis) is prohibited. This configuration can be chosen when differences in curvatures at the girder ends between the girder and the oncoming road are unwanted.

Analysis 4: In this run the modelling technic of the girders is changed. Instead of modelling the girders as continuous beams with distributed mass, they have been modelled as massless beams, but with the mass lumped at every 20 meters, see Table 5.5 on page 43.

Analysis 5: In this analysis the horizontal projected length of the backstay cable has been changed. Two analyses has been performed with the same projected height of the backstay cables as for the reference run, i.e. the slope of the cable is different on each side of the pylon top. The projected length is chosen as 555 m and 740 m, i.e. a backstay/main span ratio of 0.15 and 0.2 respectively. Two other analysis has been performed with projected lengths of 555 m and 740 m but now with an initial slope equal in the main span and in the backstays. This results in a larger projected height of the backstay cable. The boundary conditions are the same as the reference run. Table 6.1 shows the configurations from the analyses.

Table 6.1
Configurations regarding Analysis 5.

Analysis description	Span ratio	Projected length (m)	Projected height (m)
5 a)	0.2	740	140
5 b)	0.15	555	140
5 c)	0.2	740	296
5 d)	0.15	555	222

6.2 Natural frequencies

6.2.1 Classification of modes

In order to separate modes from each other, the modes have been classified into horizontal, vertical and torsional modes. Each class has then been divided into symmetric and asymmetric modes. The 3 first modes within symmetric and asymmetric modes has been found and presented in the following. This means that a total of 18 modes of vibration will be shown. The following notation has been used to describe the mode shapes;

- Class 1
  - 1st HS: First Horizontal symmetric
  - 2nd HS: Second Horizontal symmetric
  - 3rd HS: Third Horizontal symmetric
  - 1st HA: First Horizontal asymmetric
  - 2nd HA: Second Horizontal asymmetric
  - 3rd HA: Third Horizontal asymmetric
- Class 2
  - 1st VS: First Vertical symmetric
  - 2nd VS: Second Vertical symmetric
  - 3rd VS: Third Vertical symmetric
  - 1st VA: First Vertical asymmetric
  - 2nd VA: Second Vertical asymmetric
  - 3rd VA: Third Vertical asymmetric
- Class 3
  - 1st TS: First Torsional symmetric
  - 2nd TS: Second Torsional symmetric
  - 3rd TS: Third Torsional symmetric
  - 1st TA: First Torsional asymmetric
  - 2nd TA: Second Torsional asymmetric
  - 3rd TA: Third Torsional asymmetric

6.2.2 Results

The natural frequencies extracted from ABAQUS is shown in Table 6.2 on the facing page for the first four analysis. Here, a total of 18 modes are presented (6 horizontal, 6 vertical and 6 torsional modes). *Analysis* 2-4 are compared to *Analysis* 1. The number in front indicates how many sinus half waves the mode consists of. Because of this there are several modes that could be classified in the same way. As can be seen the biggest discrepancy in natural frequencies are for the horizontal modes in *Analysis* 2, were a slide bearing is introduced at one of the end supports. This leads to a more flexible structure laterally, and the frequencies decrease. Some changes in torsional frequencies can also be seen. No significant changes are seen for the vertical modes accept for the $1stVA$. This may be due to the horizontal displacements of the cables in vertical asymmetric modes, and since the girder will not constrain any movement longitudinally in this analysis, the frequency will be reduced. For the other analysis the changes are insignificant, but some small changes are seen for *Analysis* 3 where the frequencies increase for some vertical modes. This is because rotation about the lateral axis is prevented. The stiffness is increased in vertical direction causing a slightly increase in natural frequencies. *Analysis* 4 shows the results from the analysis where all mass in the girder are lumped in the shear centre and rotary inertia specified. As can be seen the two modelling techniques presented in this thesis produce the same results.

From *Analysis* 1 a total of 35 vibration modes with corresponding undamped natural frequencies has been extracted. The results are shown in Table 6.3 on page 50. Explanations of the modal shapes are given since many modes consist of a coupling between motions in different directions. As can be seen all the torsional modes are coupled with lateral deformations. All the horizontal modes given in Table 6.3 are coupled with the cables, and can be seen in Figures 6.7 on page 55 to 6.8 on page 56.

In Table 6.4 on page 51 the frequencies extracted for *Analysis* 5 are shown for the 15 first modes and compared with *Analysis* 1. Generally it can be seen the frequencies changes most for the two first vertical symmetric modes, indicated by mode 5 and 9. This is because the vertical symmetric modes introduce additional tension as mentioned earlier. And since the backstays are longer in these analyses the cables are more flexible when tension is introduced. This will reduce the natural frequencies. It can be seen that *Analysis* 5*c*) and 5*d*) cause a higher reduction in frequencies compared to *Analysis* 5*a*) and 5*b*) respectively, and this is probably because the length of the backstay cables are longer in these analysis. One torsional mode shows the same magnitude of change in frequencies as mode 5 and 9 , identified as a $2ndTS$ mode (mode 14).

6.3 Mode shapes

6.3.1 Coupling of modes

In Figure 6.1 on page 52 to 6.6 on page 55 the modes extracted from ABAQUS is plotted for *Analysis* 1. The 18 modes mentioned in Section 6.2.1 are presented. Each plot shows

Table 6.2
Natural frequencies for the 18 modes representing horizontal, vertical and torsional motion of the girder. The modes are separated as symmetric and asymmetric. Results are shown for the first four analyses where the percentage differences are given compared to Analysis 1. Values in parenthesis refer to the mode number. The empty cells indicated that any mode shape was difficult to find for this class.

Mode Description	Analysis1	Analysis2		Analysis3		Analysis4	
	Natural frequency ω_i (rad/s)	ω_i	%	ω_i	%	ω_i	%
1st HS (1)	0.185	0.179	-3.2	0.185	0.0	0.185	0.0
2nd HS (4)	0.427	0.395	-7.5	0.427	0.0	0.427	0.0
3rd HS (11)	0.721	–	–	0.721	0.0	0.721	0.0
1st HA (2)	0.321	0.295	-8.1	0.321	0.0	0.321	0.0
2nd HA (6)	0.572	0.541	-5.4	0.572	0.0	0.572	0.0
3rd HA (17)	1.003	0.968	-3.5	1.003	0.0	1.003	0.0
1st VS (5)	0.492	0.492	0.0	0.493	0.2	0.492	0.0
2nd VS (9)	0.686	0.683	-0.4	0.686	0.0	0.686	0.0
3rdVS (15)	0.921	0.919	-0.2	0.923	0.2	0.921	0.0
1st VA (3)	0.408	0.403	-1.2	0.408	0.0	0.408	0.0
2nd VA (12)	0.727	0.725	-0.3	0.728	0.1	0.727	0.0
3rdVA (18)	1.085	1.082	-0.3	1.088	0.3	1.085	0.0
1st TS (11)	0.721	0.720	-0.1	0.721	0.0	0.721	0.0
2nd TS (13)	0.772	0.747	-3.2	0.772	0.0	0.772	0.0
3rd TS (22)	1.232	1.224	-0.7	1.232	0.0	1.232	0.0
1st TA (10)	0.720	0.701	-2.6	0.720	0.0	0.720	0.0
2nd TA (21)	1.224	1.192	-2.5	1.224	0.0	1.223	0.0
3rd TA (33)	1.723	1.713	-0.6	1.724	0.1	1.723	0.0

the horizontal, vertical and torsional component of the deformation along the girder. The results show that coupling between horizontal motion and torsional motion is present in most of the modes except from the vertical modes. In some cases there are more than one mode that have the same amount of sinus half waves in the same class, as indicated in Table 6.3, but will show different degree of coupling between directions. The amplitudes are plotted as a function of the reduced length of the girder, i.e. $L(x)/L$. The deformations are labelled as follows;

- H: Horizontal (lateral)

Table 6.3
First 35 undamped vibration modes of the structure with corresponding natural frequencies, and description of the modal shape for Analysis 1.

Structural modes		
Mode nr.	ω_i (rad/s)	Modal shape
1	0.1849	1st HS
2	0.3207	1st HA
3	0.4077	1st VA
4	0.4274	2nd HS
5	0.4924	1st VS
6	0.5719	2nd HA
7	0.6445	1st Cable
8	0.6528	2nd Cable
9	0.6863	2nd VS
10	0.7201	2nd HA + 1st TA
11	0.7207	3rd HS + 1st TS + Cables
12	0.7265	2nd VA
13	0.7720	3rd HS + 2nd TS
14	0.8139	2nd TS + 3rd HS
15	0.9210	3rd VS
16	0.9507	1st TA + 3rd HA
17	1.0027	3rd HA
18	1.0847	3rd VA
19	1.1266	3rd Cable
20	1.1630	4th Cable
21	1.2235	3rd HA + 2nd TA
22	1.2318	4th HS + 3rd TS
23	1.2570	4th HS + 2nd TS
24	1.2625	4th VS
25	1.2689	3rd TS + 4th HS
26	1.4003	2nd TA + 3rd HA + Cables
27	1.4307	4th VA
28	1.5218	4th HA + 2nd TA
29	1.5741	5th Cable
30	1.6011	5th VS
31	1.6493	3rd TS
32	1.6655	6th Cable
33	1.7230	4th HA + 3rd TA
34	1.7280	5th HS + 3rd TS
35	1.7641	5th VA

- V: Vertical
- T: Torsional

Table 6.4
Comparison between Analysis 1 and Analysis 5 for the 15 first modes. Results show the natural frequencies of each analysis, and the results for Analysis 5 are compared with Analysis 1 by giving the percentage change in natural frequencies.

Mode nr.	Analysis1	Analysis 5a)		Analysis 5b)		Analysis 5c)		Analysis 5d)	
	Natural frequency ω_i (rad/s)	ω_i	%	ω_i	%	ω_i	%	ω_i	%
1	0.1849	0.1846	-0.16	0.1852	0.16	0.1852	0.16	0.1850	0.05
2	0.3207	0.3201	-0.19	0.3213	0.19	0.3214	0.22	0.3210	0.09
3	0.4077	0.4070	-0.17	0.4080	0.07	0.4078	0.02	0.4077	0.00
4	0.4274	0.4264	-0.23	0.4281	0.16	0.4280	0.14	0.4276	0.05
5	0.4924	0.4819	-2.13	0.4881	-0.87	0.4789	-2.74	0.4860	-1.30
6	0.5719	0.5710	-0.16	0.5728	0.16	0.5729	0.17	0.5723	0.07
7	0.6445	0.6442	-0.05	0.6449	0.06	0.6448	0.05	0.6447	0.03
8	0.6528	0.6524	-0.06	0.6532	0.06	0.6451	-1.18	0.6530	0.03
9	0.6863	0.6531	-4.84	0.6696	-2.43	0.6532	-4.82	0.6639	-3.26
10	0.7201	0.7130	-0.99	0.7179	-0.31	0.7110	-1.26	0.7164	-0.51
11	0.7207	0.7195	-0.17	0.7208	0.01	0.7209	0.03	0.7204	-0.04
12	0.7265	0.7255	-0.14	0.7275	0.14	0.7275	0.14	0.7269	0.06
13	0.7720	0.7684	-0.47	0.7719	-0.01	0.7690	-0.39	0.7708	-0.16
14	0.8139	0.7976	-2.00	0.8062	-0.95	0.7956	-2.25	0.8033	-1.30
15	0.9210	0.9163	-0.51	0.9204	-0.07	0.9182	-0.30	0.9192	-0.20

In ABAQUS the horizontal lateral component is along the z-axis. The vertical component is along the y-axis while the torsional rotation is referred to as rotation about the longitudinal x-axis.

Horizontal modes

Figure 6.1 to 6.2 on the next page shows that the presented horizontal modes are coupled with torsional motion. Accept from the third horizontal symmetric mode this coupling is insignificant. It can be seen that the maximum displacement in the third horizontal mode is less than unity. This means that also a coupling with the cables is present, and that the maximum displacement occurs in the cables. The plotted modes are those given in Table 6.2. A three-dimensional representation of these modes is given in Appendix D.1.

Vertical modes

Figure 6.3 on page 53 to 6.4 on page 53 shows that no coupling is present in the vertical modes. All vertical modes have the largest displacement in the girder and the cables since the girder and cables will share the same motion. The plotted modes are those given in Table 6.2. A three-dimensional representation of these modes is given in Appendix D.2.

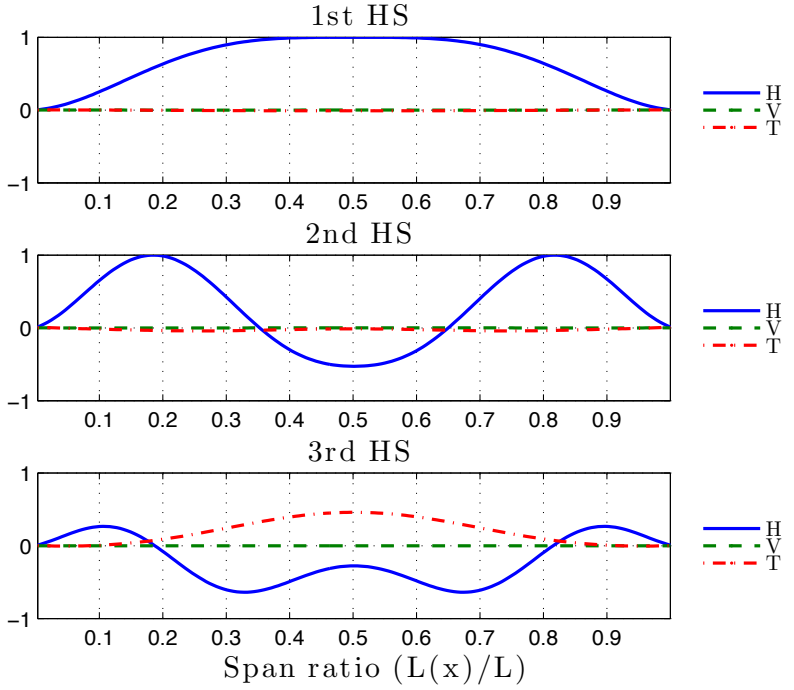

Figure 6.1: Horizontal symmetric modes.

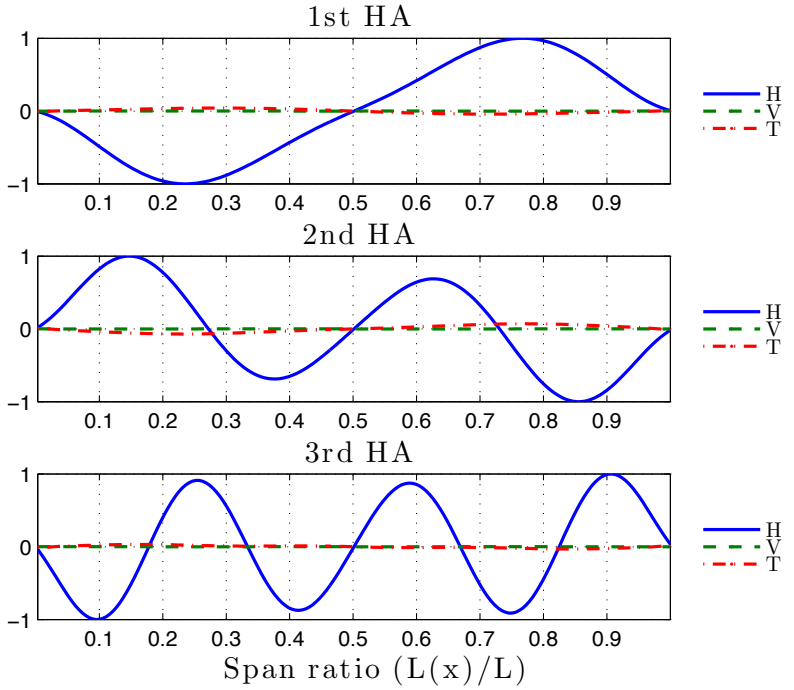

Figure 6.2: Horizontal asymmetric modes.

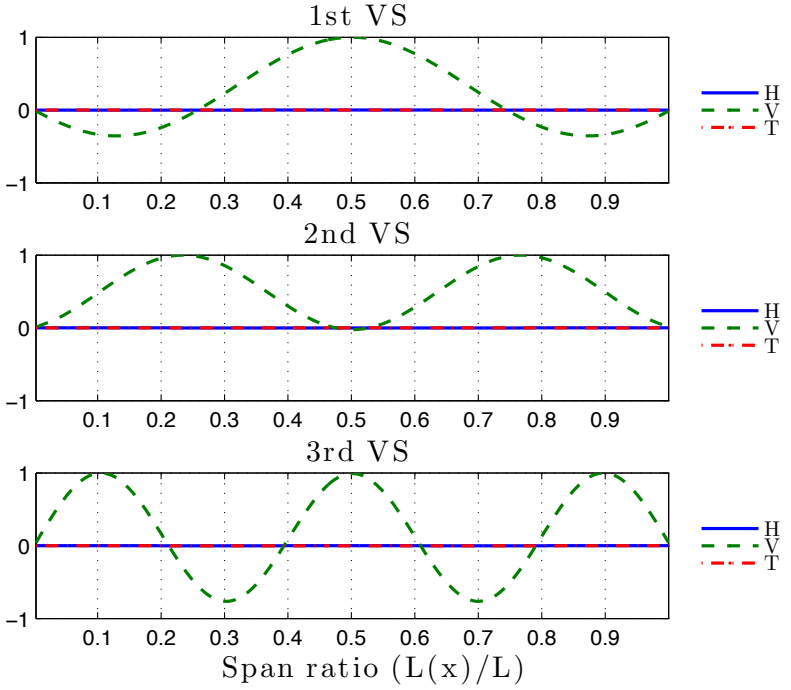

Figure 6.3: Vertical symmetric modes.

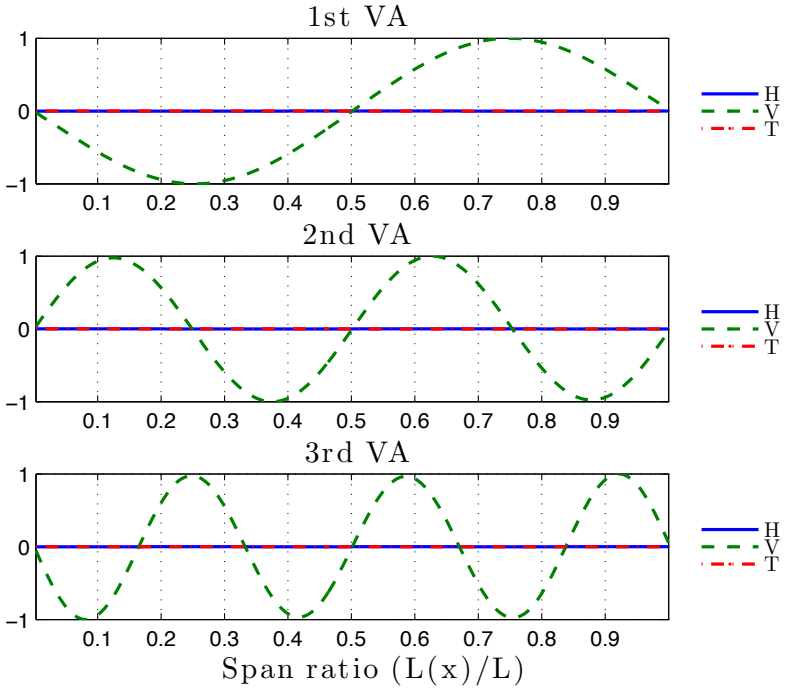

Figure 6.4: Vertical asymmetric modes.

Torsional modes

Figure 6.5 to 6.6 on the next page shows that coupling between horizontal and torsional motion is present in every mode presented. The vertical displacement due to rotation of the stiffening girder refers to the point where the hangers are attached to the bridge girder, i.e. 12.5 m from the centre of the crossbeam. Note that the torsional modes here are not necessarily those listed in Table 6.2. The symmetric modes $2ndTS$ and $3rdTS$ in the figures represents mode 14 and 31 respectively. The asymmetric modes $1stTA$ and $2ndTA$ represents mode 16 and 26 respectively. This has been done because these modes show larger amplitudes and are more illustrative, and the number of half waves are equal. A three-dimensional representation of these modes is given in Appendix D.3.

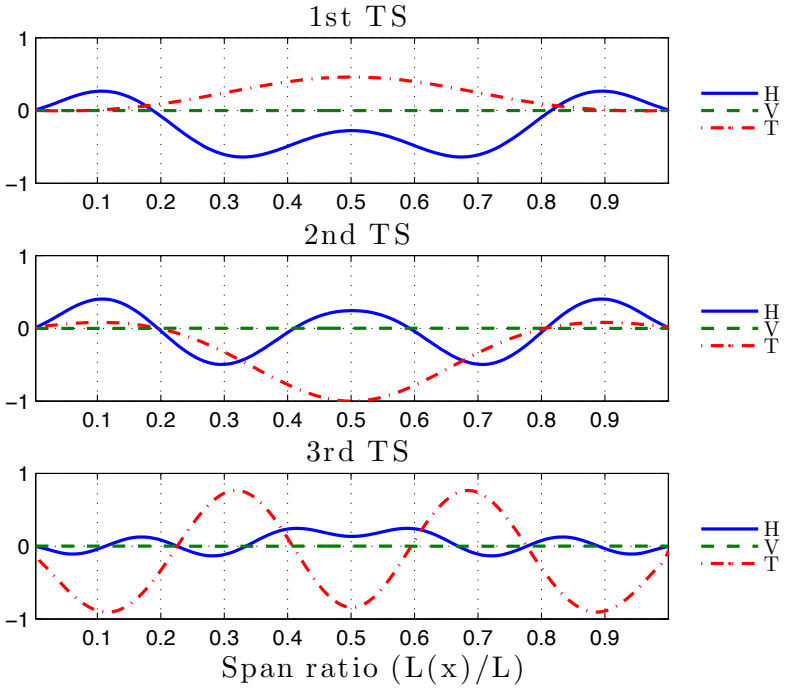

Figure 6.5: Torsional symmetric modes.

6.3.2 Coupling between cables and girder

In this section the coupling between the cables and the girder is shown. The horizontal motion of the cables are extracted from the eigenvalue analysis in ABAQUS and compared to the horizontal motion of the girder. Figures 6.7 and 6.8 on page 56 shows that the largest displacement occur in the girder in all the 6 modes accept from the third horizontal symmetric mode. It's also noticeable that the shapes of the girder and the cables are equal only for the first horizontal symmetric and asymmetric modes.

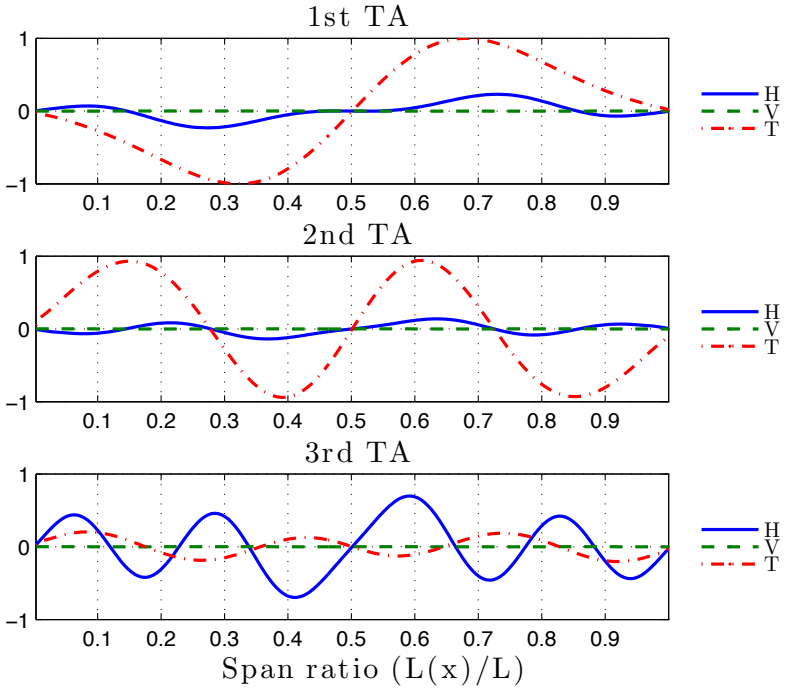

Figure 6.6: Torsional asymmetric modes.

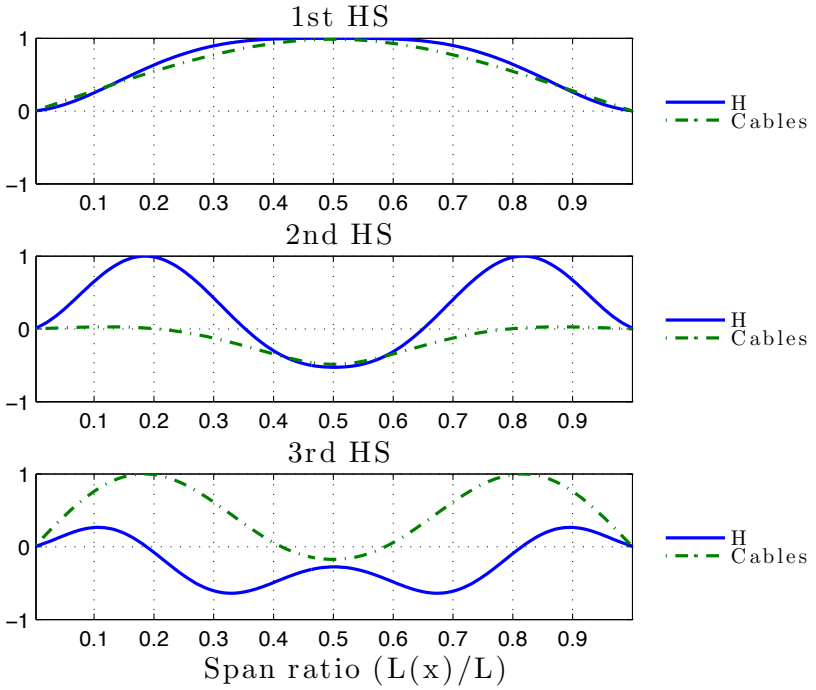

Figure 6.7: Coupling between cables and horizontal symmetric motion of the girder.

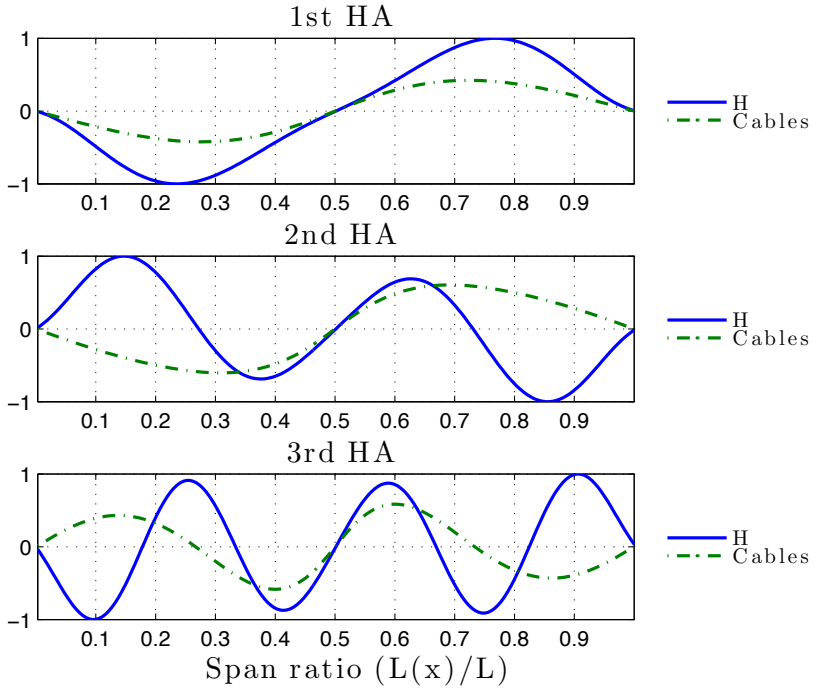

Figure 6.8: Coupling between cables and horizontal asymmetric motion of the girder.

6.4 Effective mass in response calculation

When calculating the response of a structure, it is convenient to use modal frequency analysis due to its efficiency. The modal approach can approximate the response by using only a small number of modes. For large structures, including many modes can be computationally expensive. Therefore it is important to understand which modes contribute most to the overall response. The mode shapes presented in the previous section says nothing about the response since the modal displacements are scaled and only shows how the structure will deform at natural frequencies. A method to understand the response is by studying the *modal effective mass*. The *modal effective mass* associated with each mode represents the amount of effective mass participating in the mode, compared to the total effective mass in the respective direction. Large modal effective mass compared to the total effective mass will contribute significantly to the response [6]. In ABAQUS the *modal effective masses* are calculated during the eigenvalue analysis step.

Figure 6.9 on the next page shows the percentage of modal effective mass for the first 35 modes compared to the total effective mass in vertical translational direction. The results are given for *Analysis*1. It is seen from the figure that the three highest peaks, identified as modes 5, 9 and 15, contributes most to response in vertical direction. In this thesis the focus is on stability of a suspension bridge but the *effective mass* can be helpful when interpreting the modes of the structure. The modes 5, 9 and 15 are also identified as the three first vertical symmetric (VS) modes, see Table 6.2 on page 49. I.e. the VS modes contributes most to any response in vertical direction.

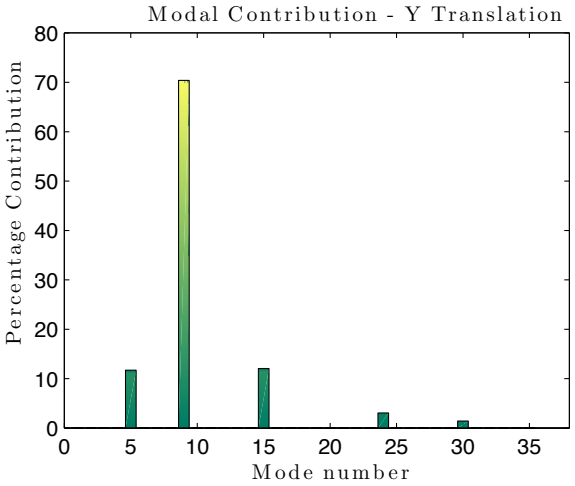

Figure 6.9: Modal effective mass for vertical translation. The modal effective mass is given for the first 35 modes. The percentage modal effctive mass contribution of each mode to the total effective mass for translation in vertical direction is shown. The first four peaks are identified as mode 5, 9, 15 and 24 respectively. The four modes contributes with more than 96 % of the total effective mass.

Figure 6.10 shows the percentage of modal effective mass for the first 35 modes compared to the total effective mass in translational lateral direction. The three highest peaks, identified as mode 1, 4 and 11 respectively, contributes most to lateral response. These modes are found to be the three first horizontal symmetric modes. It can be seen that the $1stHS$ mode contributes alone with over 80 % to any response in lateral direction.

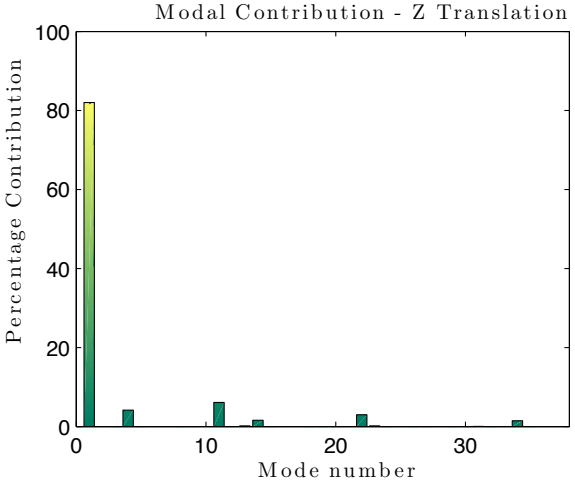

Figure 6.10: Modal effective mass for horizontal (lateral) translation. The modal effective mass is given for the first 35 modes. The percentage modal effective mass contribution of each mode to the total effective mass for translation in horizontal direction is shown. The three first peaks are identified as mode 1, 4 and 11 respectively. The three modes contributes with more than 92 % of the total effective mass.

Figure 6.11 on the following page shows the percentage of modal effective mass compared

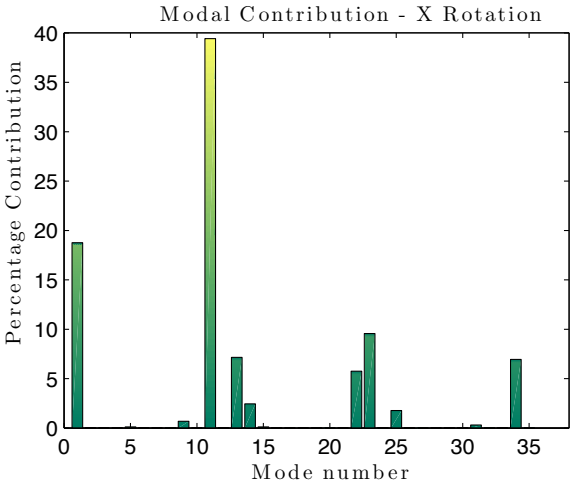

Figure 6.11: Modal effective mass for rotation about the longitudinal axis. The modal effective mass is given for the first 35 modes. The percentage modal effective mass contribution of each mode to the total effective mass for rotation about the longitudinal axis is shown. The two highest peaks are identified as mode 1 and 11 respectively. The two modes contributes with about 58% of the total effective mass.

to total effective mass for rotation about the x-axis. The two highest peaks are identified as mode 1 and 11, i.e. the first horizontal symmetric mode and the third horizontal symmetric mode (or the first torsional symmetric mode) respectively. As can be seen there are several other modes that contributes to rotation about the x-axis, and these modes are identified as a coupling between horizontal and torsional motion.

It has been shown that the asymmetric modes do not contribute that much to lateral response as the symmetric modes. But the asymmetric modes for horizontal and vertical motion can be shown to have a significant contribution to the total effective mass for rotation about the vertical and lateral axes, see figures in Appendix A.7.

6.5 Estimation of structural properties

When calculating the stability limit by the flutter formula presented in 4.3 on page 28 the structural mass associated with the horizontal, vertical and torsional degree of freedoms goes into the equations as modal equivalent distributed mass or mass moment of inertia (MOI). The modal equivalent distributed masses , $\tilde{m}_y$ and $\tilde{m}_z$, can be estimated from a theoretical approach assuming that the total mass in the main span is spread out or distributed over the length of the girder. The MOI, $\tilde{m}_\theta$, can be approximated by summation of the contribution from the cables, hangers, girders and crossbeam in the centre of the sailing lane, i.e. at the midpoint of the bridge where the cables are horizontal. The MOI is then calculated by assuming that the rotation centre is in the middle of the crossbeam since the bridge is symmetric about this point. From Table 3.1, Equation 3.21 and Equation 3.27 in Section 3.4 the MOI can be calculated for cross section $2TFGP$ using the parallel axis theorem, and that the radius of gyration d for the cables are equal to

half the total width of the cross section, i.e. 12.5 m. The results from the calculation are summed up in the Table 6.5. When calculating the contribution from the crossbeam the formulae $1/12 * m_{cb} * L_{cb}^3/20m$ is used, where m_{cb} is the distributed mass of the crossbeam in lateral direction, and L_{cb} is the length of the beam (5 m). The table shows that the modal equivalent distributed masses $\tilde{m}_y$ and $\tilde{m}_z$ are approximated to be 25,700 kg/m, and the modal equivalent MOI as 2,840,000 kgm^2/m. Henceforth the coordinate system is changed such that the notations of the axis are in accordance with that given in Chapter 4, i.e. the vertical axis will be denoted z-axis and the y-axis denotes the lateral axis.

Table 6.5
Theoretical modal equivalent distributed mass and MOI of the bridge in the centre of the sailing lane. The value in parenthesis refers to the distributed mass of the crossbeam along its length in lateral direction. In the total value for the MOI given for the girder, the MOI about its shear centre is added, according to Table 3.1.

Element	Distributed mass one plane (kg/m)	Radius of gyration d (m)	Mass moment of inertia (kgm^2/m)
Girder	6,494.9	7.5	877,873.1
Hangers	104.4	12.5	32,625.0
Cables	6,165.4	12.5	1,926,687.5
Crossbeam	84.8 (678.4)		353.3
Total	25,699		2,837,538.9

An alternative approach is to calculate the modal equivalent distributed mass and MOI from the output given by the FEM model using the mode shape integrals and the modal masses. The equation below can be used as an estimation [35].

$$\tilde{M}_{ii} = \int \phi_{yi}^2 dx * \tilde{m}_y + \int \phi_{zi}^2 dx * \tilde{m}_z + \int \phi_{\theta i}^2 dx * \tilde{m}_\theta \tag{6.1}$$

This equation has three unknown $\tilde{m}_y$, $\tilde{m}_z$ and $\tilde{m}_\theta$, but by studying the mode shapes and the modes shape integrals the number of unknowns may be reduced. The first horizontal symmetric mode has been shown to have no significant coupling with the torsional motion, see Figure 6.1 on page 52. The vertical deformation in this mode is equal to zero. This eliminates the second and third term on the right hand side in the equation above since the mode shape integrals associated with $\tilde{m}_z$ and $\tilde{m}_\theta$ are zero. Equation 6.1 can then be solved for $\tilde{m}_y$;

$$\tilde{m}_{y1} = \frac{\tilde{M}_{11}}{\int \phi_y^2 dx} \tag{6.2}$$

The same procedure can be done with the other horizontal modes, and from Figures 6.1-6.2 on page 52 it is seen that all the horizontal modes, except from the third horizontal

symmetric mode, doesn't couple (at least not significantly) with torsional motion. These modes are identified as mode 1, 4, 2, 6 and 17 respectively. Table 6.6 show the results by using Equation 6.2. As can be seen the distributed mass will vary, depending on the mode shapes but also the coupling between the girder and the cables. This is clearly seen from Figure 6.7 on page 55 where the girder shape of the first horizontal symmetric mode almost equals the shape of the cables, leading to a large modal mass. The value obtained from mode 11 is clearly not valid when using Equation 6.2 since this mode show significant coupling between horizontal and torsional deformations.

Table 6.6
Modal equivalent distributed mass $\tilde{m}_{yi}$ for selected number of modes.

Mode nr.	Modal equivalent distributed mass $\tilde{m}_{yi}$
1	23 735
4	15 021
11	56 327
2	15 924
6	19 872
17	17 095

The vertical modes are not coupled to any of the other directions but are coupled to the cables. Equation 6.2 can then be used to estimate the modal equivalent distributed mass $\tilde{m}_z$, by changing y with z. Table 6.7 shows the results for the three first horizontal symmetric and asymmetric vertical modes. As can be seen there are some variations between modes but the values are close to each other. An average for all values is given in the bottom cell, and by comparing with the value given in Table 6.5 there is a discrepancy of about $1,3\%$ compared to the theoretical value.

Table 6.7
Modal equivalent distributed mass $\tilde{m}_{zi}$ for six first vertical modes.

Mode nr.	Modal equivalent distributed mass $\tilde{m}_{zi}$
5	25 944
9	25 843
15	25 659
3	27 289
12	26 241
18	25 264
Average	26 040

Since the horizontal modal equivalent distributed mass $\tilde{m}_y$ varies from mode to mode, the moment of inertia will also vary when using Equation 6.1 to calculate $\tilde{m}_\theta$. Some values has been calculated by assuming that $\tilde{m}_y$ is equal to the one of mode 1 for all modes and

solving the equation below. Modes where deflection due to rotation of the girder is large are chosen. The results are given in Table 6.8.

$$\tilde{m}_{\theta i} = \frac{\tilde{M}_{ii} - \int \phi_{yi}^2 dx * \tilde{m}_{yi}}{\int \phi_{\theta}^2 dx} \tag{6.3}$$

Table 6.8
Mass moment of inertia $\tilde{m}_\theta$ for some selected modes when assuming $\tilde{m}_y$ found from mode 1.

Mode nr.	Mass moment of inertia $\tilde{m}_\theta$
14	2 570 000
16	3 377 200
25	3 331 900
26	3 569 500
31	3 527 000

Compared to the theoretical values these results gives deviating values, but at least they are in the same order of magnitude. In order to visualize the variation in modal mass, the modal mass is calculated for different values of $\tilde{m}_y$, $\tilde{m}_z$ and $\tilde{m}_\theta$. The estimated modal mass is plotted as percentage of the modal mass found from the FEM model. The results are shown in Figure 6.12 on the next page. As can be seen it is the estimated modal mass for the vertical modes that coincide fair with the exact modal mass, obviously. The cable modes are left out in the plot. The biggest discrepancy is for the modes where horizontal and torsional deformation couples. When using the flutter equations to find any stability limit the vertical modal equivalent distributed mass, $\tilde{m}_z$, and the mass moment of inertia, $\tilde{m}_\theta$, is chosen from the theoretical values found above. I.e. $\tilde{m}_z = 25,700 kg/m$ and $\tilde{m}_\theta = 2,840,000 kgm^2/m$. This has been done based on the discussion above and since this will make comparison between different cross sections easier.

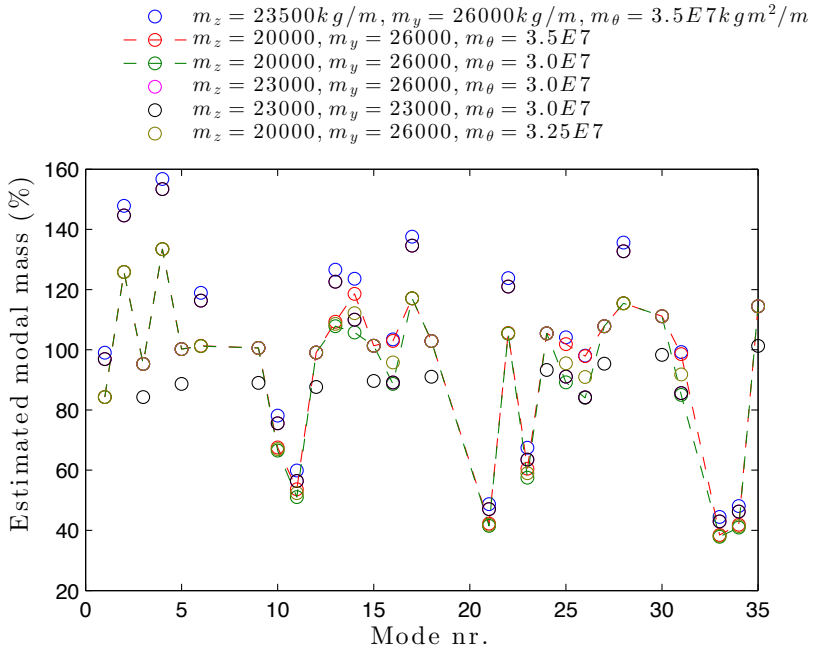

Figure 6.12: Estimated modal mass given as percentage of the modal mass from the FEM model. The modal mass is calculated using different values and combinations of $\tilde{m}_y$, $\tilde{m}_z$ and $\tilde{m}_\theta$.

Chapter 7

Results from stability analysis

In Chapter 4 the flutter equations and the eigenvalue solution was presented. In this chapter these solutions have be tested for a range of cross section models. The cross section $2TFGP$ presented in Section 3.2 has been found in the literature, and the aerodynamic derivatives has been extracted from figures in the article written by Matsumoto et al. [14]. The quality of these figures is limited, so that the results given must not be taken for granted. Some other cross sections have also been tested. These are found in a report carried out by Hansen et al. [11] as a study for The Norwegian Public Road Administration called *Brusymfonien*. Here several cross sections with separated box-girders have been tested in the wind tunnel. The shapes are similar to the cross section $2TFGP$ and with crossbeams connecting the box-girders. The cross sections have been tested with and without guide vanes, and with/without a walking/cycle path centrally aligned at the top of the crossbeams. Herein, only cross sections without a walking/cycle are discussed. The distance between the box-girder has been varied to see if this gives improved results. In this thesis four different configurations has been tested, a cross section with distance between the girders of 15 m (henceforth referred to as $BS15GV$), one with a distance of 20 m ($BS20GV$) and one with 30 m between the girders. The cross section with 30 m between the girders has been chosen to be tested for a configuration with/without guide vanes mounted at the top ends of the crossbeams. With guide vanes the cross section is referred to as $BS30GV$ and without as $BS30$. On both $BS15GV$ and $BS20GV$ the guide vanes are mounted to the lower outer edge of the girders. In the wind tunnel the cross sections has been tested on a scale model of $1:50$, i.e. the mass properties has been scaled up in order to represent a full-scale model. In the following the different cross sections will be presented, with their cross sectional properties and aerodynamic derivatives. In the FEM-model the same stiffness properties as for $2TFGP$ has been used for the girders and the crossbeams when modelling the bridge with cross sections from $Brusymfonien$. The same configurations regarding the cables and hangers are used in all analysis.

7.1 Representation of self-exited forces

The force model for the self exited forces associated with the aerodynamic derivatives presented in Section 4.1 was developed for a single girder with total width equal B. When the formulas are used for the presented cross sections above it is important that the forces are represented in the same way they are implemented in the solution routines. The difference is how the aerodynamic derivatives are extracted and what is defined as the width B. In Strømmen [35] and Øiseth et al. [26] (see also [27]), the aerodynamic

derivatives are functions of the circular frequency (rad/s) and the width B of a girder, while for the cross sections mentioned above the aerodynamic derivatives are functions of the frequency in Hz and different definitions of the width. Below these differences are discussed for each cross section. All the derivatives associated with lateral motion, $P_n^*, n \in \{1, 2..., 6\}$, H_n^* and $A_n^*, n \in \{5, 6\}$, are disregarded for cross section $2TFGP$. This because the load coefficients has not been found for this cross section. I.e. any forces in lateral direction have not been considered. At the end of this chapter the quasi-steady load coefficients have been introduced for the cross sections from $Brusymfonien$.

7.1.1 Section 2TFGP

In Matsumoto et al. [14] the self-exited forces are given as;

$$\begin{aligned} q_{z,se} &= \frac{1}{2}\rho(2b)V^2\left(kH_1^*\frac{\dot{r}_z}{V} + kH_2^*\frac{b\dot{r}_\theta}{V} + k^2H_3^*r_\theta + k^2H_4^*\frac{r_z}{b}\right) \\ q_{\theta,se} &= \frac{1}{2}\rho(2b)^2V^2\left(kA_1^*\frac{\dot{r}_z}{V} + kA_2^*\frac{b\dot{r}_\theta}{V} + k^2A_3^*r_\theta + k^2A_4^*\frac{r_z}{b}\right) \end{aligned} \tag{7.1}$$

Here, $k = b\omega/V$ is the reduced frequency and ω the in-wind resonant frequency. b is here defined as half the chord length, where the chord length describes the width of one box-girder. Using the notation presented in Figure 3.2 on page 11 for the width of one girder, B^*, and introducing that $B^* = 2b$ the equation above can be written as;

$$\begin{aligned} q_{z,se} &= \frac{1}{2}\rho V^2B^*\left(K\left(\frac{H_1^*}{2}\right)\frac{\dot{r}_z}{V} + K\left(\frac{H_2^*}{4}\right)\frac{B^*\dot{r}_\theta}{V} + K^2\left(\frac{H_3^*}{4}\right)r_\theta + K^2\left(\frac{H_4^*}{2}\right)\frac{r_z}{B^*}\right) \\ q_{\theta,se} &= \frac{1}{2}\rho V^2(B^*)^2\left(K\left(\frac{A_1^*}{2}\right)\frac{\dot{r}_z}{V} + K\left(\frac{A_2^*}{4}\right)\frac{B^*\dot{r}_\theta}{V} + K^2\left(\frac{A_3^*}{4}\right)r_\theta + K^2\left(\frac{A_4^*}{2}\right)\frac{r_z}{B^*}\right) \end{aligned} \tag{7.2}$$

Here, $K = B^*\omega/V$ is the reduced frequency. One other thing to be aware of is that the derivatives must be read off at the reduced velocity $V_{red} = V/(n * B^*)$, where n is the frequency in Hz. This means that the reduced velocity $V_{red} = V/(\omega * B^*)$ must be multiplied by 2π in order to extract the correct values of the derivatives.

7.1.2 Sections from $Brusymfonien$

The other cross sections for *Brusymfonien* (given in [11]) presented above use the width of one girder as b, which in this case equals B^*. I.e. the self-excited forces are directly given by Equation 4.13 on page 26 with B^* replacing B. The derivatives for the cross sections in *Brusymfonien* are also given as a function of the frequency in Hz, therefore the same procedures must be executed as mentioned in the previous section. The self-exited forces for the cross sections are then given by;

$$q_{z,se} = \frac{1}{2}\rho V^2 B^* \left(KH_1^* \frac{\dot{r}_z}{V} + KH_2^* \frac{B^* \dot{r}_\theta}{V} + K^2 H_3^* r_\theta + K^2 H_4^* \frac{r_z}{B^*} \right)$$
$$q_{\theta,se} = \frac{1}{2}\rho V^2 (B^*)^2 \left(KA_1^* \frac{\dot{r}_z}{V} + KA_2^* \frac{B^* \dot{r}_\theta}{V} + K^2 A_3^* r_\theta + K^2 A_4^* \frac{r_z}{B^*} \right) \quad (7.3)$$

7.2 Aerodynamic derivatives and mass properties

7.2.1 Cross section 2TFGP

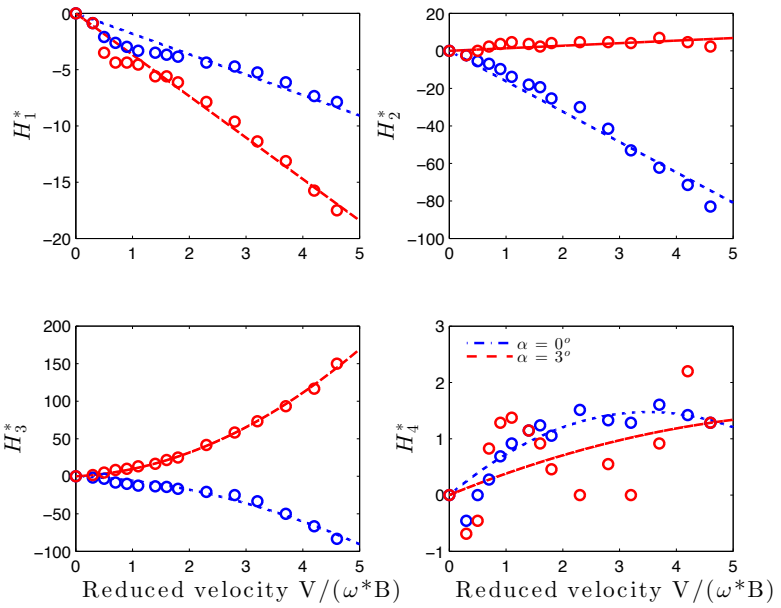

Figure 7.1: Aerodynamic derivatives H_n^* for cross section $2TFGP$: Blue circles refers to experimental data obtained in wind tunnel experiments in smooth flow at an angle of 0^o. Blue dashed lines are curves fitted to the data. Red circles refers to data obtained at an angle of 3^o and red dashed lines are curves fitted to the data.

The cross section used for the preliminary design in this thesis is shown in Figure 3.2 on page 11. As mentioned the aerodynamic derivatives has been extracted from Matsumoto et al. [14] and polynomials has been fitted to the curves. The derivatives H_1^*, A_3^* and A_4^* has been fitted with a first order polynomial (linear functions), while the five remaining derivatives has been fitted with a second order polynomial. This has been done because the reduced velocity for the actual bridge will become large since the natural frequencies are low, meaning that the critical frequency also will be quite low. Since the experimental data are limited to a reduced velocity at about 5, it is important to have curves that not gives unrealistic data outside the experimental range. Higher polynomial has been found to give such unrealistic values. The experimental results and curves fitted to the data are shown in Figure 7.1 and 7.2 on the following page. It has been investigated in the literature

that the most important derivatives associated with flutter are A_1^*, A_2^*, A_3^*, H_1^* and H_3^* [14, 27]. As can be seen the polynomial curves fit well for the most important derivatives in the reduced velocity range measured in experiments. The experiments presented have been carried out under the condition with wind angle of attack α of 0^o in smooth flow, and $\alpha = 3^o$ in turbulent flow.

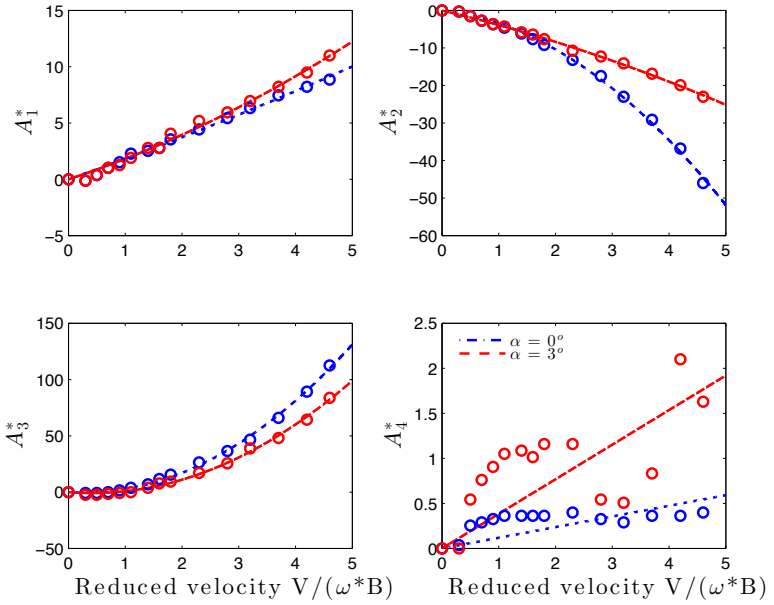

Figure 7.2: Aerodynamic derivatives A_n^* for cross section $2TFGP$: Blue circles refers to experimental data obtained in wind tunnel experiments in smooth flow at an angle of 0^o. Blue dashed lines are curves fitted to the data. Red circles refers to data obtained at an angle of 3^o and red dashed lines are curves fitted to the data.

7.2.2 Cross section BS15GV

The cross section with 15 m between the box-girders is shown in Figure 7.3 on the next page. The mass properties are given in Table 7.1 on the facing page, where values are given for the model scale and the full scale. When modelling the cross section in $ABAQUS$ the distributed mass and mass moment of inertia are specified as point mass with rotary inertia at every 20 m in nodes located in the centre of each crossbeam. The values implemented in $ABAQUS$ is given in Table 7.2 on page 69. The experimental data and the polynomial parameters are given in Appendix C.6. The experimental data has been fitted with second order polynomials and the result is shown in Figure 7.4 on page 68. As can be seen, the results show fairly good accuracy for the important derivatives, especially for the highest reduced velocities from where experimental results have been found.

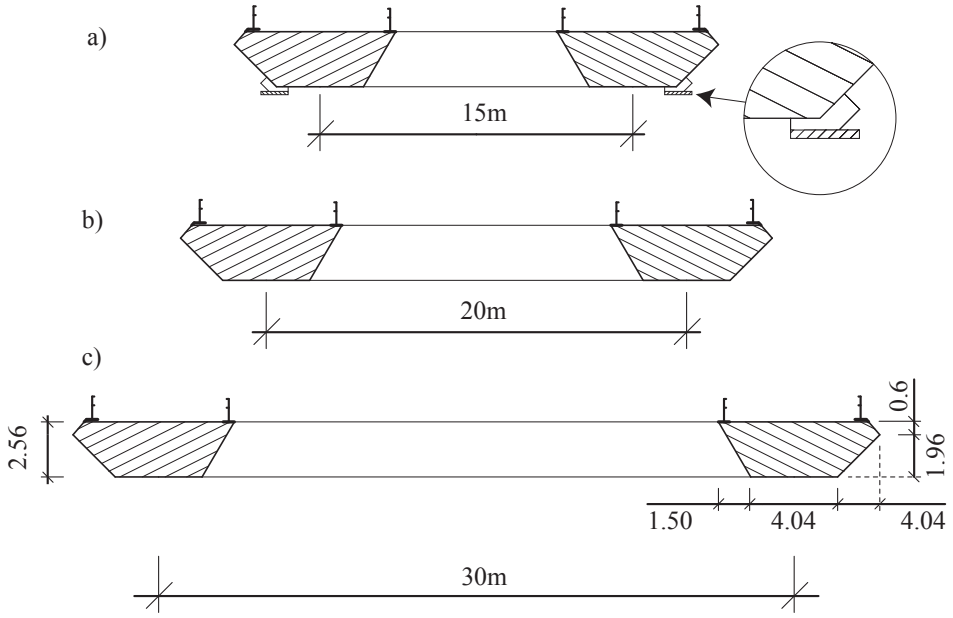

Figure 7.3: Cross sections from *Brusymfonien* [11]: (a) Cross section $BS15GV$ with $15m$ between the centres of the box-girders. (b) Cross section $BS20GV$. (c) Cross sections $BS30/BS30GV$. All dimensions are in meters. Guide vanes for $BS30/BS30GV$ are mounted at the top of the crossbeams, but not shown here.

Table 7.1
Mass and mass moment of inertia (MOI) for the tested cross sections. Values are given for the model scale (MS) and the full scale (FS) [11].

Section	Mass, MS (g)	Mass mom. of inertia, MS (gmm^2)	Mass, FS (tons/m)	Mass mom. of inertia, FS ($tonsm^2/m$)
BS30	7,326	$494.678 * 10^6$	10.77	1,818.7
BS30GV	7,326	$494.678 * 10^6$	10.77	1,818.7
BS20GV	6,827	$267.377 * 10^6$	10.04	983.0
BS15GV	6,758	$201.726 * 10^6$	9.94	741.6

7.2.3 Cross section BS20GV

The cross section with 20 m between the box-girders is shown in Figure 7.3. The mass properties are given in Table 7.1. When modeling the bridge with this cross section the same procedure as before was followed. The experimental data for the derivatives are taken from *Brusymfonien* and fitted with second order polynomials. The result are shown in Figure 7.5 on page 70, and the experimental data with the polynomial parameters are given in Appendix C.5. As can be seen, the results show fairly good accuracy for the

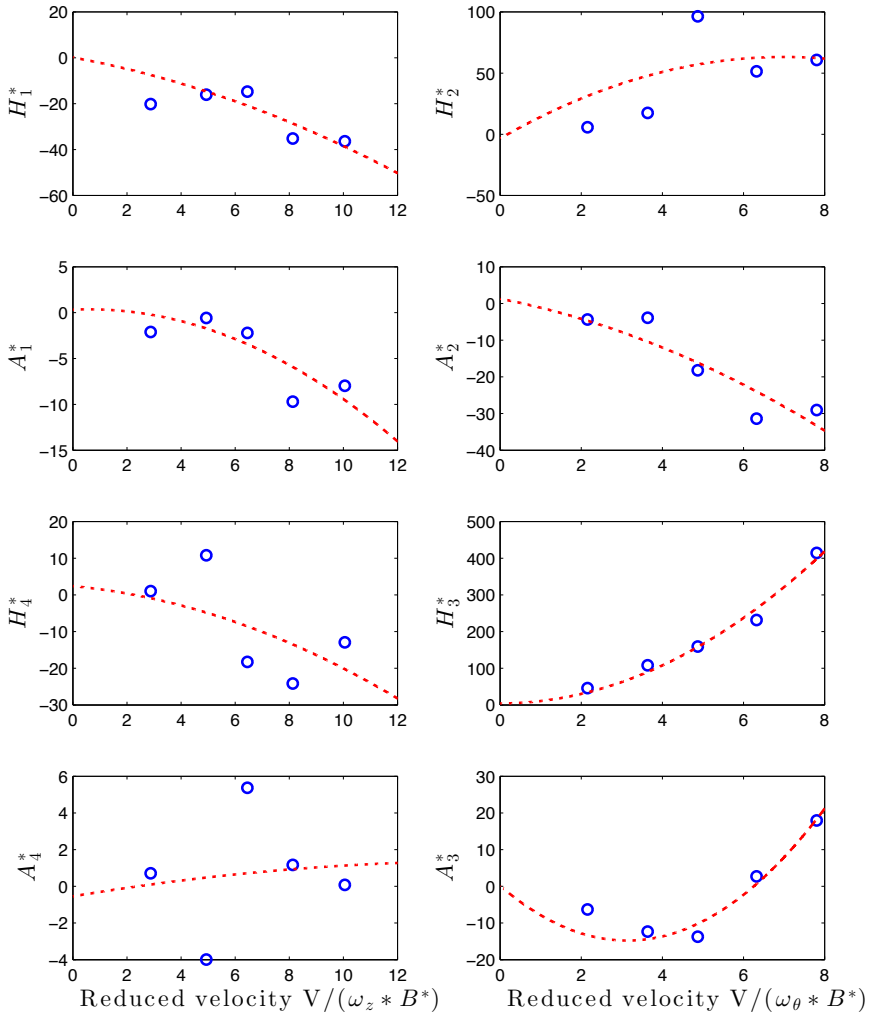

Figure 7.4: Aerodynamic derivatives for cross section $BS15GV$ with guide vanes. Blue circles refers to experimental data obtained in wind tunnel experiments, angle of incidence 0^o. Red dashed lines are curves fitted to the data.

important derivatives. The biggest discrepancy is for A_1^* which shows a scatter spread out in the data range. I.e. values for A_1^* outside the data range are highly uncertain.

7.2.4 Cross section BS30 and BS30GV

The cross section with 30 m between the box-girders is shown in Figure 7.3 on the preceding page. The mass properties of the cross section is given in Table 7.1 on the previous page. The values implemented in the FEM-program is given in Table 7.2. The experimental data for the derivatives are, as mentioned, taken from *Brusymfonien*, and second order

Table 7.2
Mass properties for the cross sections given in $Brusymfonien$ and used as input in the FEM model. I11 is the mass moment of inertia (MOI) about the longitudinal x-axis, I22 the MOI about the vertical y-axis and I33 the MOI about the lateral z-axis. The directions follow the notation in ABAQUS. The values are calculated by multiplying the values in Table 7.1 by 20 m.

Point mass/Inertia	Section			
	BS30	BS30GV	BS20GV	BS15GV
Mass (tons)	215.4	215.4	200.8	198.8
I11 (tons m^2)	36,374.0	36,374.0	19,660	14,832
I22 (tons m^2)	7,180	7,180	6,693.3	6,626.7
I33 (tons m^2)	7,180	7,180	6,693.3	6,626.7

polynomials has been used as an approximation. The experimental data and the parameters used is given in Appendix C.2 and C.3. Figure 7.6 on page 71 and 7.7 on page 72 shows the approximation and the experimental results. As can be seen, the results shows fairly good approximations for the important aerodynamic derivatives, except for A_2^* for cross section $BS30$ where a first order polynomial may give better approximation outside the reduced velocity range tested. Outside the reduced velocity range the polynomial values turns towards zero, which implies that the aerodynamic torsional damping will be underestimated, i.e. the results will be conservative. For all the cross sections the range of the reduced velocities vary, and outside this range it is difficult to know which values are correct. Any stability results obtained when choosing values outside the range of the data must therefore be interpreted with caution.

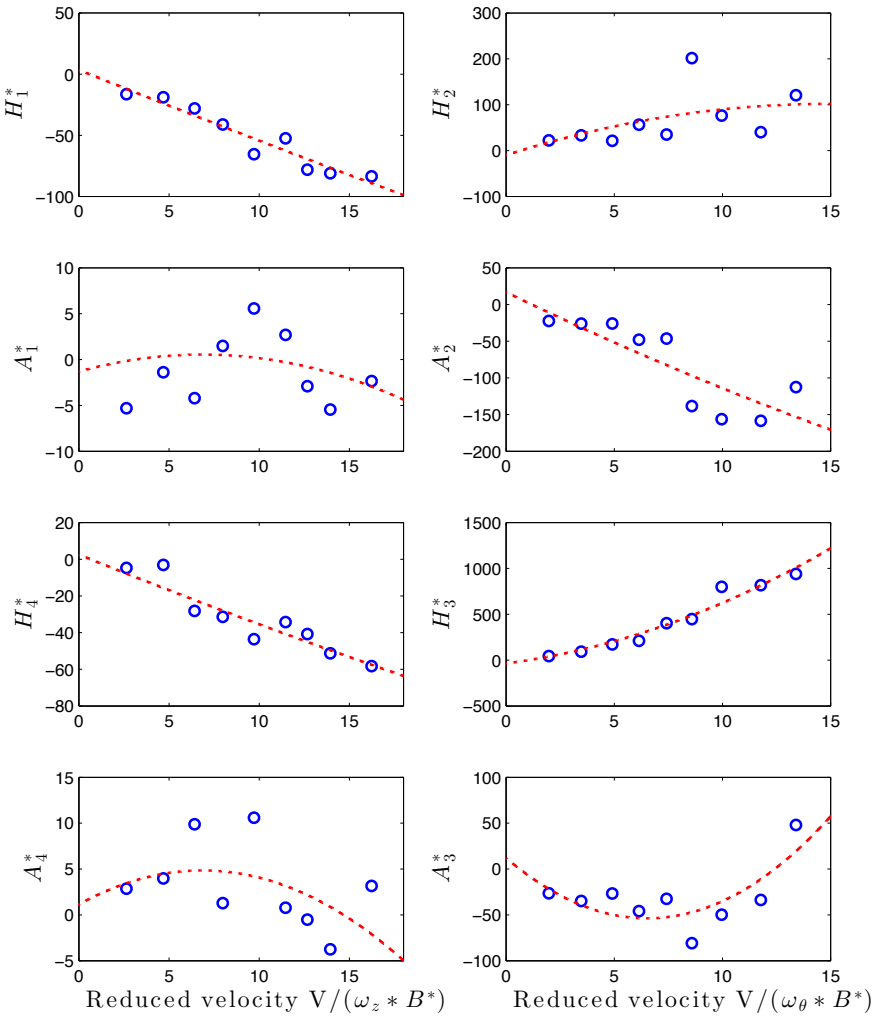

Figure 7.5: Aerodynamic derivatives for cross section $BS20GV$ with guide vanes. Blue circles refers to experimental data obtained in wind tunnel experiments, angle of incidence 0^o. Red dashed lines are curves fitted to the data.

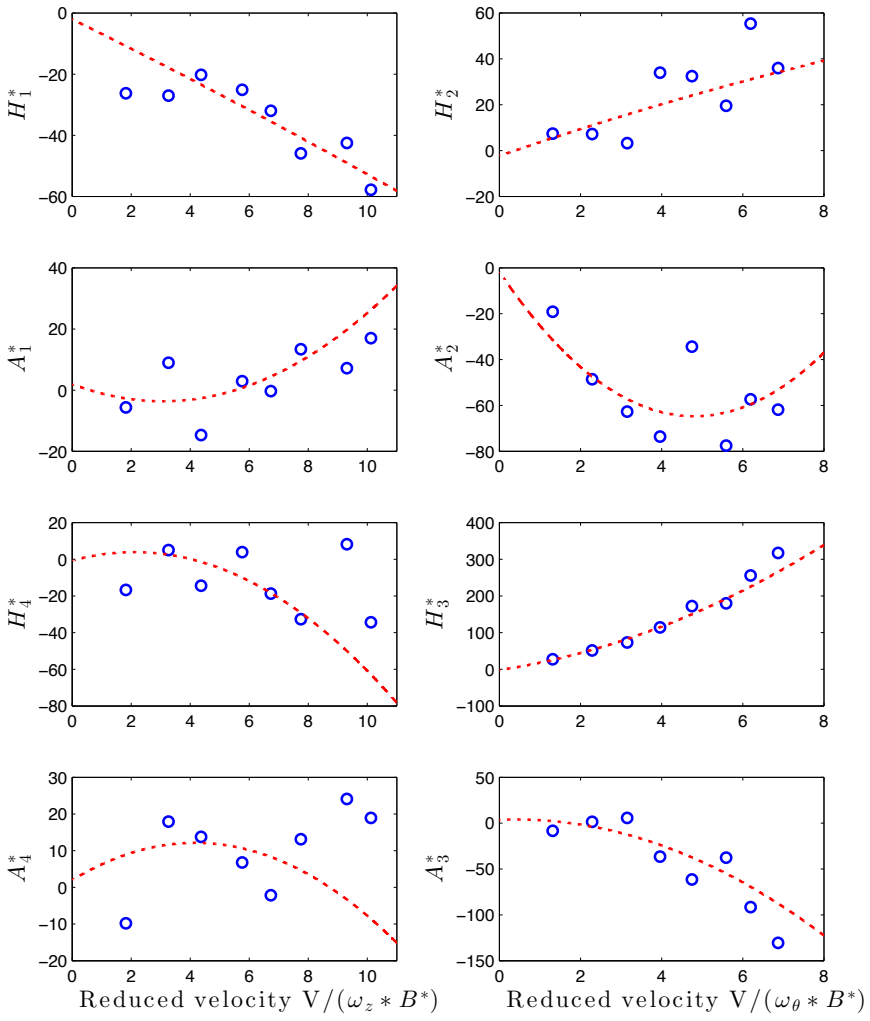

Figure 7.6: Aerodynamic derivatives for cross section $BS30$ without guide vanes. Blue circles refers to experimental data obtained in wind tunnel experiments, angle of incidence 0^o. Red dashed lines are curves fitted to the data.

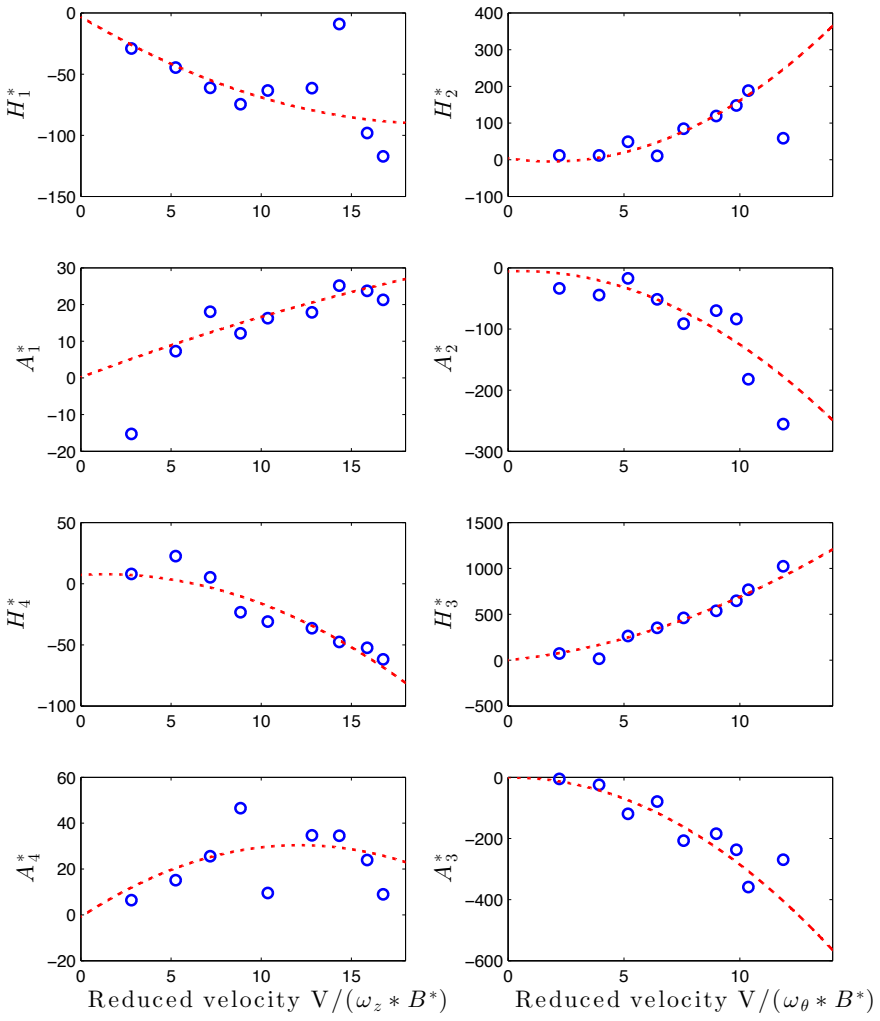

Figure 7.7: Aerodynamic derivatives for cross section $BS30GV$ with guide vanes. Blue circles refers to experimental data obtained in wind tunnel experiments, angle of incidence 0^o. Red dashed lines are curves fitted to the data.

7.3 Numerical Results: Eigenvalue solution

In this section the different cross sections have been tested applying an eigenvalue solution routine provided by Øiseth [25]. First, results from *Analysis* 1 through *Analysis* 5 are presented using the cross section $2TFGP$ for an angle of incidence of the wind flow equal to 0^o and 3^o. Next the solution from *Analysis* 1 has been evaluated and the modes that contribute most to the stability limit is found and discussed further. The cross sections from $Brusymfonien$ has also been tested and compared with each other and cross section $2TFGP$. It is well known that two factors are of great importance for which modes that couples into a flutter motion, namely the shape-wise similarity and the frequency ratio between shape-wise vertical and torsional modes. In the following these factors will be studied further. An attempt of solving the complex eigenvalue solution has been made, and the solution routines are given in Appendix E.2 and E.4. The solution is given for selected results, and compared with the provided solution. The solution routine in Appendix E.1 is used when calculating the stability limit from the provided eigenvalue solution.

7.3.1 Eigenvalue solutions for cross section 2TFGP

Results obtained from the eigenvalue solution using cross section $2TFGP$ in *Analysis* 1 through *Analysis* 5 are shown in Table 7.3 on the following page. The width and height of the cross section are B= 25 m and D= 2 m respectively. The width of one girder, B^* is 10 m. The density of air is assumed to be $\rho = 1.25\ kg/m^3$. As can be seen from the table the stability limit doesn't change significantly for *Analysis* 1 through *Analysis* 4. In these analysis the boundary conditions were changed, and as expected the results shows only small changes because of small changes in frequencies for the vertical and torsional modes, see Table 6.2 on page 49. The natural frequencies of the horizontal modes were reduced with up to about 8% (for the $1stHS$ mode) when introducing a slide bearing at one of the girder supports in *Analysis* 2. If this affects the stability limit is unknown since the eigenvalue solution used doesn't account for horizontal contributions from self-exited forces associated displacements and velocities. I.e. the derivatives $A_n^*, n \in \{1, 2, ..., 6\}$, $H_n^*, n \in \{5, 6\}$ and $A_n^*, n \in \{5, 6\}$ has been neglected. *Analysis* 2 shows a small reduction in critical velocity for the 3^o case, which may be caused by small changes in the mode shapes or that the frequency between the first vertical and torsional symmetric mode were slightly reduced. But this may just as well be due to accuracy in the solution routine.

A higher discrepancy can be seen for *Analysis* 5 where the backstay geometry has been changed. *Analysis* 5*a*) shows a higher reduction then *Analysis* 5*b*), clearly because the length of the backstay cable were longer in this analysis, leading to a more flexible structure when the pylons are not present. It has been shown, see Table 6.4 on page 51, that the reduction in natural frequencies are largest for the vertical symmetric modes. And because of the additional tension these modes introduce the backstay cable will stretch out, leading to a larger displacement at the pylon top when the backstay cable becomes longer (larger sag). This has also been studied in Toshio [37] where it was found that a higher span ratio

Table 7.3
Eigenvalue solution for the different analysis performed in the FEM model with cross section 2TFGP. The results are shown both for angle 0^0 and 3^o of incidence of the wind flow. The percentage difference compared to *Analysis* 1 is given at the bottom of each cell. 30 modes has been included in the calculations.

Mode combination	Derivatives 0^o		Derivatives 3^o	
	Critical Velocity V_{CR}(m/s)	Critical frequency ω_{CR} (rad/s)	Critical Velocity V_{CR} (m/s)	Critical frequency ω_{CR} (rad/s)
Analysis 1	142.32	0	100.27	0.473
Analysis 2	142.27 (-0.04%)	0	100.01 (-0.26%)	0.473 (0%)
Analysis 3	142.37 (0.04 %)	0	100.25 (-0.02%)	0.474 (0.21%)
Analysis 4	142.32 (0%)	0	100.27 (0%)	0.473 (0%)
Analysis 5a)	138.29 (-2.83%)	0	96.82 (-3.44%)	0.462 (-2.33%)
Analysis 5b)	140.03 (-1.61%)	0	98.47 (-1.80%)	0.469 (-0.85%)
Analysis 5c)	136.91 (-3.80%)	0	95.84 (-4.42%)	0.459 (-2.96%)
Analysis 5d)	139.22 (-2.18%)	0	97.84 (-2.42%)	0.467 (-1.27%)

between the backstay and the main span length reduced the critical velocity. The main reason is probably because the mode shapes changes slightly. An investigation showed that the shape-wise similarity of the vertical and torsional mode contributing most to the stability limit increased as the backstay geometry was changed. The two governing modes were found to be mode 5 and 14. The shape-wise similarity was found to be 0.95 for *Analysis* 5*c*) compared to 0.90 for *Analysis* 1. The reduction in stability limit seems to be almost proportional to the increase in shape-wise similarity of mode 5 and 14. The frequency change may also explain the difference in stability limit. From Table 6.4 the overall frequencies of the vertical and torsional modes are reduced. This also changes the reduced velocity and by this also the values of the aerodynamic derivatives.

An eigenvalue solution from *Analysis* 1 is shown in Table 7.4 on the next page. Here, different modes combinations have been included in the solution routine. From the table, the critical frequency is zero for the case with an angle of incidence of the wind equal to 0^o. This indicates that an instability phenomenon other that flutter will occur, namely static

Table 7.4
Eigenvalue solution when using cross section $2TFGP$. The results are shown for a variety of mode combinations, both for angle 0^0 and 3^o of incidence of the wind flow. Empty cells indicate that no solution was found within the maximum iterations specified in the solution routine or that the resonant frequency is zero. The values in parenthesis are found from the eigenvalue routine created by the author.

Mode combination	Derivatives 0^o			Derivatives 3^o		
	Critical Velocity V_{CR}(m/s)	Critical frequency ω_{CR} (rad/s)	Reduced velocity V_{red}	Critical Velocity V_{CR} (m/s)	Critical frequency ω_{CR} (rad/s)	Reduced velocity V_{red}
50 modes	142.3	0	–	100.2	0.473	21.2
40 modes	142.3	0	–	100.2	0.473	21.2
30 modes	142.3	0	–	100.3	0.473	21.2
20 modes	142.7	0	–	100.6	0.473	21.3
15 modes	142.7	0	–	100.6	0.473	21.3
14 modes	142.7	0	–	100.6	0.473	21.3
13 modes	268.7	0	–	160.8	0.479	33.6
10 modes	458.4	0	–	242.8	0.313	77.6
3 and 16	248.1	0	–	153.7	0.407	37.8
3 and 21	–	–	–	677.4	0.537	126.1
5 and 11	331.3	0	–	187.6	0.478	39.2
5 and 13	464.8	0	–	234.3	0.488	48.0
5 and 14	168.7	0	–	114.4	0.475	24.1
5,11,13 and 14	144.0	0	–	100.9	0.473	22.2
3,11,13 and 14	143.7	0	–	158.9	0.472	21.4
3,5,11,13 and 14	143.7	0	–	100.9 (101.0)	0.472 (0.472)	21.3 (21.4)
3,5,9,11,13 and 14	143.7	0	–	100.3 (100.4)	0.472 (0.473)	21.3 (21.2)
11,13 and 14	144.5	0	–	159.2	0	–
11 and 14	151.7	0	–	–	–	–
11 and 13	272.5	0	–	–	–	–
13 and 14	159.4	0	–	–	–	–
14	169.4	0	–	–	–	–

divergence. This instability phenomenon is recognized as a static instability where the structure looses its torsional stiffness due to interaction with the airflow. Assume that the torsional mode that has the lowest natural frequency and responsible for the instability can be simplified to;

$$\boldsymbol{\varphi}_2(x) \approx \begin{bmatrix} 0 & 0 & \phi_\theta \end{bmatrix}^T \tag{7.4}$$

Then, the impedance matrix given in Equation 4.26 on page 30 is reduced to;

$$\hat{E}_\eta(\omega_r = 0, V_{cr}) = 1 - \kappa_{ae_{\theta\theta}} = 0 \tag{7.5}$$

Thus, static divergence may be identified from the following equation;

$$\kappa_{ae_{\theta\theta}} = \frac{\rho B^4}{4\tilde{m}_\theta}\left(\frac{\omega_\theta(V_{cr})}{\omega_\theta}\right)^2 A_3^* \frac{\int_{L_{exp}} \phi_\theta^2 dx}{\int_L \phi_\theta^2 dx} = 1 \tag{7.6}$$

When the instability is static, the quasi-static counterpart to A_3^* applies, and by comparing $\boldsymbol{K}_{ae}(x)$ in Equation 4.14 with $\boldsymbol{K}_{ae}(x)$ in Equation 4.11 the critical velocity is given as;

$$V_{cr} = B \cdot \omega_\theta \cdot \left(\frac{2\tilde{m}_\theta}{\rho B^4 C'_M} \cdot \frac{\int_L \phi_\theta^2 dx}{\int_{L_{exp}} \phi_\theta^2 dx}\right)^{1/2} \tag{7.7}$$

For this cross section it has not been successful to find any values for the coefficient C'_M, therefore it has been considered unnecessary to estimate the static stability limit from the equation given above with values found from other cross sections in the literature.

From Table 7.4 on the previous page it is seen that when using three torsional modes (11, 13 and 14) the solution converges. This indicates that the static instability limit is a multimode phenomenon, where three still air torsional modes contributes significantly to the stability limit. The table also indicate that mode nr. 14 contribute most of the three torsional modes. Since static divergence is the governing stability phenomenon it is reasonable to believe that flutter will not occur below this wind velocity, at least for an angle of incidence 0^o. For the 3^o case the stability limit decreases significantly, and the solution indicate that the instability is a flutter phenomena. The table shows that when using modes 5 and 14 in the calculations the stability limit is increased from 100 to 114 m/s. Compared to other mode combinations this indicates that these two modes contribute significantly to the critical velocity. But when adding modes 11 and 13 to the calculations the solution converges, indicating a multimode-coupled flutter phenomenon. From Table 7.5 on the facing page it can be seen that mode 5 is highly shape-wise similar to mode 11, 13 and 14, but one may expect that the mode combination 5 and 13 would contribute more to the stability limit then mode 5 and 14 since they are more shape-wise similar than 5 and 14. Also the frequency ratio between mode 5 and 13 is lower. This may be explained by studying the mode shapes of mode 13 and 14. In Appendix D.4 it can be seen that in mode 14 the maximum displacements are due to a torsional motion of the bridge girder with some coupling to the lateral motion, while in mode 13 it has been found that maximum displacements are in the lateral direction. I.e. both modes couples with the horizontal motion but to a different degree, and may indicate that this coupling have an influence on which modes that will contribute most to the critical velocity, and not only the shape-wise similarity and frequency ratio. The result indicates that the

multimode phenomenon has a destabilizing effect since including several torsional modes reduces the stability limit.

Table 7.5
Shape-wise similarity of modes for cross section $2TFGP$.

Mode combination	Shape-wise similarity $\psi_{z\theta}$
5 and 11	0.74
5 and 13	0.93
5 and 14	0.90
3 and 11,13 or 14	$\sim$0
9 and 11	0.26
9 and 13	0.07
9 and 14	0.09

As Table 7.4 shows, the reduced velocity ranges from 21 at the lowest critical velocity up to about 50 when combining mode 5 and 13. Compared to the reduced velocity range in the experiments for the aerodynamic derivatives (up to about 5), this is obviously a much higher reduced velocity range, implying that the aerodynamic derivatives must be extrapolated for all possible mode combinations. This reduces the reliability of the results since experiments up to these ranges are unknown. In Appendix A.1 the design critical velocity was found as 63.3 m/s. In the vicinity of this velocity the frequency of motion in the 3^o case is found from the eigenvalue solution to be ω= 0.786 rad/s for mode combination 5, 11, 13 and 14. This implies a reduced velocity of 7.63, which is much closer to the experimental range, but still values must be extrapolated. For the most important derivatives the extrapolated values may be said to provide reasonable accurate values, see Figures 7.1 and 7.2 on page 66.

Values in parenthesis were obtained using the eigenvalue solution routine created by the author. This solution did not give any reasonable results for the 0^0 case, but for the 3^o case this solution gave the same results when including few modes in the calculations. One reason is that the solution gives eigenvalues λ_n that doesn't necessarily come in the same order in each velocity iteration. This has been found to give some unstable behaviour in the numerical solution, especially when several modes are included in the calculations. This problem has not been given any attention in this thesis, and any modification in the routine is left for further investigations. From the discussion above it may be concluded that the stability limit caused by multimodal effects are possible when a vertical mode is shape-wise similar to two or more torsional modes. This has also been stated in [27]. Results also indicate that several torsional modes contribute when static divergence is the governing instability phenomenon. In the 3^o case, the wind flow is turbulent. This may reduce the validity of the results since the buffeting forces may become considerably in this configuration and are no longer negligible. This has not been considered herein, but are more thoroughly discussed in Sarkar et al. [29].

In Section 4.4 on page 32 it was stated that in the present of any stability limit the

damping term μ_n turns positive, indicating negative damping and diverging oscillation of the structure. This is illustrated in Figure 7.8 where the real part and the imaginary part of the eigenvalues are shown for mode combination 5, 11, 13 and 14 in the 3^o case. As can be seen the damping term turns positive for the vertical mode indicating that the critical frequency is on the vertical branch solution. This is confirmed as the critical frequency is found to be 0.473 rad/s compared to the undamped natural frequency of mode 5 (0.492 rad/s), see Table 6.3 on page 50.

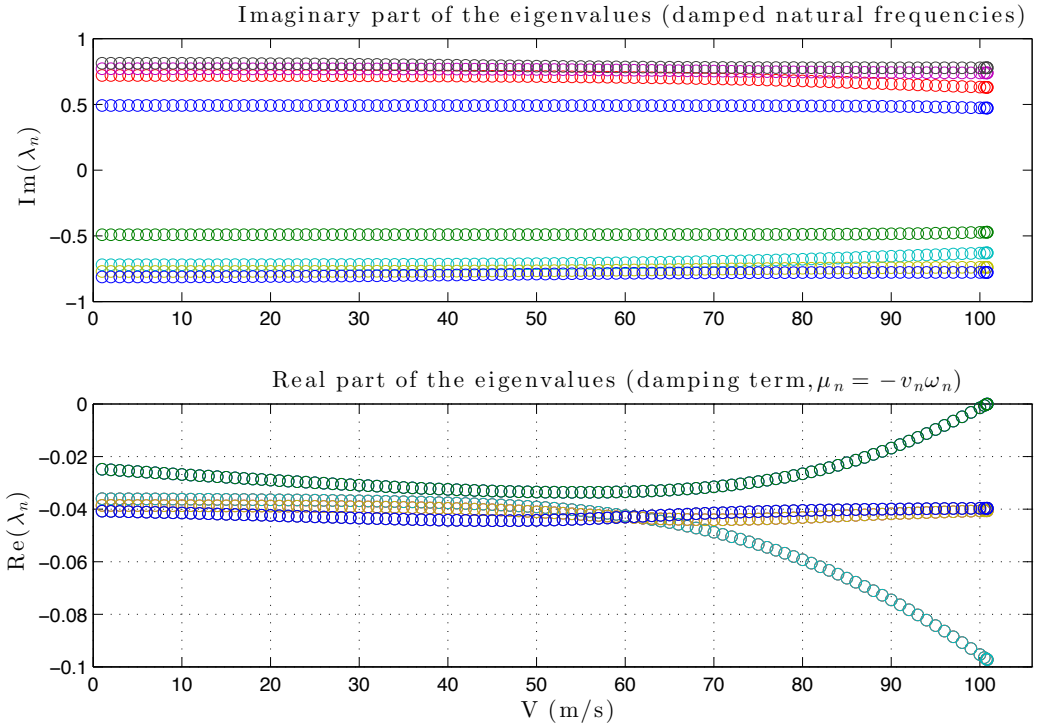

Figure 7.8: Development of the eigenvalue solution for cross section 2TFGP and mode combination 5, 11, 13 and 14 in the 3^o case. The upper plot shows the damped natural frequencies given by $\omega_D = \omega_n\sqrt{1-v_n^2}$. Since the eigenvalues comes in complex conjugated pairs both the negative and positive values of the damped natural frequencies are plotted. The lower plot shows the real part of the solution associated with damping of the modes, including both structural and aerodynamic damping.

As the eigenvalue solution shows, only a few modes are needed for the solution to converge to the exact value. It is usual the lowest modes that contributes most to the critical velocity. In a computational point of view this is an advantage since the system matrices are strongly reduced in dimensions when only a few modes are included in the solution. This is clearly shown in Figure 7.9 on the next page where the computational time is plotted against the number of modes included in the solution. The result is shown for cross section $2TFGP$ at 3^o, and indicates a reduction in computational time of about 96% when reducing the number of modes from 50 to 14. Calculating the shape-wise similarity of different mode combinations is helpful when choosing the modes to be included in the calculation, and may save a lot of computational effort.

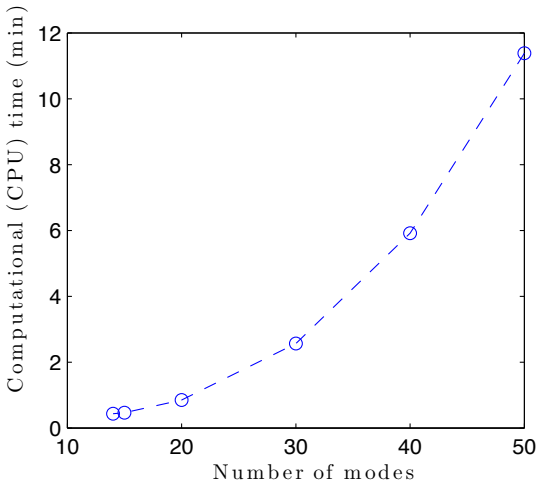

Figure 7.9: Computational time as a function of the number of modes included in the eigenvalue solution for the 3^o case. Computational time will also depend on the CPU power in the computer used.

7.3.2 Eigenvalue solutions for cross section BS15GV

Results obtained from the eigenvalue solution using cross section $BS15GV$ are shown in Table 7.6 on the following page, and shape-wise similarities for a collection of mode combinations are shown in Table 7.7 on page 81. This analysis is referred to as *Analysis* $BS15$. The width and height of the cross section are $B = 22.96\ m$ and $D = 2.56\ m$ respectively. The width of one girder, B^* is $7.5\ m$. The density of air is assumed to be $\rho = 1.25\ kg/m^3$. Table 7.6 shows the critical velocities and corresponding critical frequencies for several different mode combinations, both shape-wise similar modes and dissimilar modes.The first 5 vertical and torsional modes are shown in Apendix D.5. Values in parenthesis are values extracted from the created eigenvalue routine. It can be seen that a mode combination of mode 5, 12 and 14 gives a critical velocity close to the exact solution. With only mode 5 and 14 included the critical velocity decreases to $114\ m/s$. This is likely to be caused by the weakly shape-wise similarity of mode 12 and 14, providing a higher stability limit and a stabilizing effect. This also indicates that the stability phenomenon is multimode-coupled flutter, where two vertical modes and one torsional mode contributes significantly. As for cross section $2TFGP$ it is mode 5 and 14 that contributes most to the stability limit. These modes are identified as the first vertical symmetric mode and the second symmetric torsional mode respectively, as given in Figure 6.3 on page 53 and 6.5 on page 54. Compared with cross section $2TFGP$ the critical velocity is about $20\ m/s$ higher. The discrepancy between the 3^o case and the present analysis may be due to some differences in structural masses. This cross section is lighter than $2TFGP$ and the distance between the cable planes are reduced. This changes the natural frequencies. Table 7.8 on page 82 shows natural frequencies of vertical and torsional modes and they are meant to represent the same modes as for $2TFGP$. It can be seen that the vertical frequencies are higher probably because of a reduced distributed mass of the cross section. The torsional frequencies are reduced probably because of the

reduced torsional stiffness provided by the cables. This would indicate a lower stability limit, but this is not the case. The reason may be due to the reduced shape-wise similarity of mode 5 and 14 as the governing modes, see Table 7.5 on page 77 and 7.7 on the facing page. It must also be mentioned that the results for $2TFGP$ were obtained by using derivatives at $\alpha = 3^o$. This is markable tilting of the cross section and may reduce the stability limit significantly. It may be concluded that the aerodynamic properties of the cross section is of great importance for the stability.

Table 7.6
Eigenvalue solution using cross section BS15GV with a distance of $15m$ between each box-girder. The cross section has been tested with guide vanes. Empty cells indicate that no solution were found within the maximum iterations specified in the solution routine or that the resonant frequency is zero. The values in parenthesis are found from the eigenvalue routine created by the author.

Mode combination	Critical Velocity V_{CR}(m/s)	Critical frequency ω_{CR} (rad/s)	Reduced velocity V_{red}
30 modes	120.2	0.744	21.5
20 modes	123.5	0.746	22.1
15 modes	122.5	0.746	21.9
	(84.6)	(0.746)	(15.1)
4 and 16	139.6	0.808	23.0
5 and 11	–	–	–
5 and 14	114.9	0.725	21.1
12 and 14	182.0	0	–
5,12 and 14	121.6	0.745	21.8
	(121.6)	(0.745)	(21.8)
12 and 25	181.5	1.122	21.6
	(181.5)	(1.122)	(21.6)
5,12,14 and 25	118.4	0.744	21.2
	(118.4)	(0.744)	(21.2)

From Table 7.6 it can be seen that the reduced critical velocity is 21.5 when 30 modes are included, which is way out of the range of the experimental results for the aerodynamic derivatives. As for cross section $2TFGP$ this reduces the reliability of the results. At a velocity of 60 m/s the frequency of motion is found to be 0.786, which gives a reduced velocity of about 10.2. This is within the experimental range for the derivatives $H_n^*, A_n^*, n \in \{1, 4\}$. For the other four derivatives an interpolation is needed but as can be seen from 7.4 on page 68 the polynomials seems to follow the path of the experiments, except from derivative H_2^* where the polynomial path seems to change towards zero. But this cross section is not very sensitive to any changes for derivative H_2^*, as will be shown at the end in this section. The discussion above indicates that any stability problem due to high wind velocities below the critical design wind velocity is of no concern.

Table 7.7
Shape-wise similarity of modes for cross section $BS15GV$.

Mode combination	Shape-wise similarity $\psi_{z\theta}$
4 and 14	∼0
4 and 16	0.94
5 and 11	0.43
5 and 14	0.84
12 and 14	0.15
12 and 25	0.86

The development of the eigenvalue solution using mode 5, 12 and 14 is given in Figure 7.10. Since the critical frequency were found to be 0.745 rad/s for this mode combination, the result indicate that the critical frequency is on the torsional branch. This is confirmed by comparing the colours on both plots, indicating that the damping in the torsional mode reaches zero. It can also be seen that the damped frequency of the lowest vertical mode reaches zero. This may indicate that the instability goes from a multimode to a classic coupled flutter phenomenon.

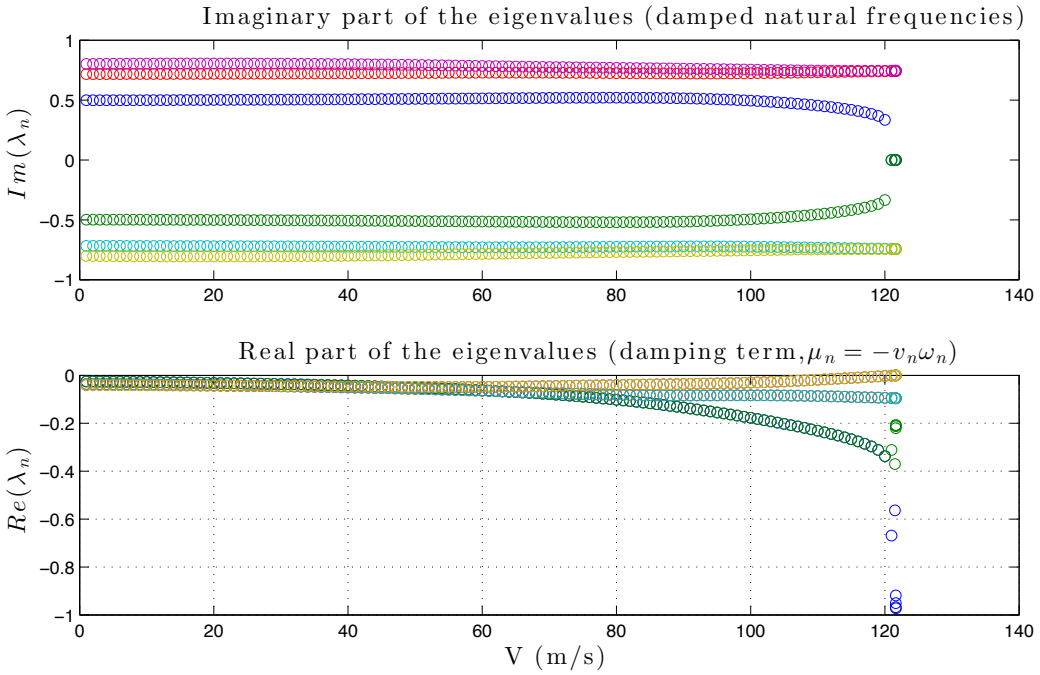

Figure 7.10: Development of the eigenvalue solution for cross section $BS15GV$ with mode combination 5, 12 and 14.

Table 7.8
Vertical and torsional natural frequencies for the tested cross sections. The percentage difference for cross section $BS15GV$ is given compared to $2TFGP$, while the percentage difference for cross sections $BS20GV$ and $BS30/BS30GV$ is given compared to cross section $BS15GV$. The values in parenthesis are the mode nr. for the respective frequency and analysis. Mode description V indicate a vertical mode while T indicate torsional modes.

Mode description	2TFGP	BS15GV		BS20GV		BS30/BS30GV	
	Natural frequency ω_i (rad/s)	ω_i	%	ω_i	%	ω_i	%
V	0.408 (3)	0.402 (4)	-1.45	0.402 (4)	0.12	0.404 (4)	0.42
V	0.492 (5)	0.500 (5)	1.50	0.498 (5)	-0.36	0.497 (6)	-0.24
V	0.686 (9)	0.719 (12)	4.79	0.714 (12)	-0.67	0.706 (12)	
T		0.659 (9)		0.663 (9)	0.74		
T	0.720 (10)	0.662 (10)	-8.07	0.664 (10)	026	0.628 (10)	-5.42
T		0.692 (11)		0.694 (11)	0.38		
V	0.727 (12)	0.734 (13)	1.02	0.727 (13)	-0.94	0.727 (15)	-0.03
T	0.814 (14)	0.802 (14)	-1.45	0.761 (14)	-5.16	0.713 (13)	-6.27
V	0.921 (15)	0.942 (17)	2.31	0.927 (17)	-1.64	0.924 (18)	-0.31
T	0.951 (16)	0.927 (16)	-2.47	0.830 (15)	-10.48	0.714 (14)	-14.04

7.3.3 Eigenvalue solutions for cross section BS20GV

Results obtained from the eigenvalue solution using cross section BS20GV are shown in Table 7.9 on page 84. Values in parenthesis are values extracted from the routine given in Appendix E.4.1. Shape-wise similarities for a collection of mode combinations are shown in Table 7.10 on page 84. The analysis is referred to as *Analysis* $BS20$. The total width of the cross section is $B = 27.96\ m$. The height and the width of one girder are the same as for cross section $BS15GV$, i.e. $D = 2.56\ m$ and $B^* = 7.5\ m$ respectively. As can be seen from Table 7.9 a mode combination of mode 5 and 14 gives a critical velocity close to the exact solution. Mode combination 4 and 15 increases the critical velocity by over 20 m/s even if the shape-wise similarity is higher for this combination, see Table 7.10. This may be due to the frequency ratio, which is about 1.5 for combination 5 and 14 while the ratio is about 2 for combination 4 and 15, see Table 7.8. When adding mode 11 to the calculation the critical velocity decreases with only about 1 m/s. When including 4 vertical and 5 torsional modes, the solution nearly converges to the exact value, indicating that this is a multimode-coupled flutter phenomenon but where one vertical and one torsional mode contributes significantly. Compared to *Analysis* $BS15$ the critical velocity increases with about 15 %. Investigating the frequencies, they are reduced compared to *Analysis* $BS15$, and the percentage reduction in torsional frequencies are higher then the reduction in vertical frequencies giving a lower frequency ratio. Neither does the shape-wise similarity change significantly between modes 5 and 14; actually it is increased in this analysis, from

0.84 to 0.88 for mode combination 5 and 14. These factors would indicate a lower critical velocity but this is not the case. One explanation is that the aerodynamic properties of this cross section are improved, since the distance between the box-girders is increased. This may be explained from Figures 7.5 on page 70 and 7.4 on page 68 where cross section $BS20GV$ shows higher negative values for derivatives H_1^* and A_2^* in the experimental range, which influence the stability limit by providing positive damping in vertical and torsional motion respectively.

The reduced critical velocity for this cross section is 29.3 when 30 modes are included, obviously much higher than the range of the experimental results. The polynomial values are therefore extrapolated also for this cross section, rendering uncertain results regarding the critical velocity. At a wind speed of 60 m/s the frequency of motion for this cross section is found to be 0.694 rad/s when including modes 5, 11 and 14 in the calculation. This gives a reduced critical velocity of about 11.5. This value is within the range of the experimental results given for the derivatives. From Figure 7.5 on page 70 it can be seen that for the most important derivatives the polynomials fit well to the experiments at a critical velocity equal to 11.5. The largest discrepancy is for A_1^* where the polynomial underestimates the value at this point. It can also be seen that the polynomial underestimate the aerodynamic stiffness associated with torsion by giving lower negative value of A_3^* at this point. The aerodynamic damping associated with torsion is also underestimated by providing lower value of A_2^* at this point. These remarks are on the safe side and strengthen the indication that this cross section provides a stability limit above the design critical velocity.

The development of the eigenvalue solution using mode 5, 11 and 14 is given in Figure 7.11 on page 85. As can be seen the damping of the vertical mode increases as the velocity increase, identified as the dark green curve in the lower plot. I.e. the critical frequency is on the torsional branch solution of mode 14 since an eigenvalue solution with only mode 5 and 14 provides almost the same critical velocity, see Table 7.9. The figure also illustrates a challenge in the numerical solution. It can be seen that the curves change colour because the eigenvalues doesn't necessarily come in the same order when solving the eigenvalue problem given in Section 4.4. The figure shows that this problem occur when the damped frequency curves intersect. This numerical challenge has been found to cause numerical instabilities in the solution routine created by the author, especially when several modes are included in the calculations.

7.3.4 Eigenvalue solutions for cross sections BS30/BS30GV

Results obtained from the eigenvalue solution using cross section $BS30$ are shown in Table 7.11 on page 86. Values in parenthesis are values extracted from the solution routines given in Appendix E.4.1 and E.2. As the results show this routine gives accurate results when few modes are included in the solution. Shape-wise similarities for a collection of mode combinations are shown in Table 7.12. The analysis is referred to as *Analysis* $BS30$. The total width of the cross section is $B = 37.96\ m$. The height and width of one girder are the same as for the other cross sections from $Brusymfonien$. From Table

Table 7.9
Eigenvalue solution using cross section BS20GV with a distance of $20m$ between each box-girder. The cross section has been tested with guide vanes. The values in parenthesis are found from the eigenvalue routine created by the author.

Mode combination	Critical Velocity V_{CR} (m/s)	Critical frequency ω_{CR} (rad/s)	Reduced velocity V_{red}
30 modes	137.6	0.626	29.3
20 modes	138.0	0.625	29.4
15 modes	137.9	0.625	29.4
	(116.8)	(0.623)	(25.0)
4 vert. + 5 torsional	137.9	0.625	29.4
4,5,11,14 and 15	139.3	0.633	29.3
5,11 and 14	139.3	0.633	29.3
	(139.3)	(0.633)	(29.3)
5 and 14	140.0	0.637	29.3
	(140.0)	(0.637)	(29.3)
4 and 15	163.9	0.655	33.4
	(163.9)	(0.655)	(33.4)

Table 7.10
Shape-wise similarity of modes for cross section $BS20GV$.

Mode combination	Shape-wise similarity $\psi_{z\theta}$
4 and 11	∼0
4 and 14	∼0
4 and 15	0.96
5 and 11	0.52
5 and 14	0.88
5 and 15	∼0

7.11 it can be seen that a mode combination of modes 6, 11 and 13 provides a critical velocity almost equal to the exact solution. This indicates a multimode-coupled flutter phenomenon where one vertical and two torsional modes contribute significantly to the critical velocity. The shape-wise similarity are almost identical for mode combinations 6, 11 and 6, 13 but the frequency ratio is lower for combination 6 and 11, providing a lower critical velocity then combination 6 and 13. Compared to the two previous analyses the critical velocity is reduced significantly. This may be due to reduction in natural frequencies. From Table 7.8 on page 82 it can be seen that the vertical frequencies are slightly reduced while the torsional frequencies are reduced by 5.4 % for mode 10 and 6.3 % for mode 13, where mode 13 corresponds to mode 14 in *Analysis* $BS15$ and $BS20$. In

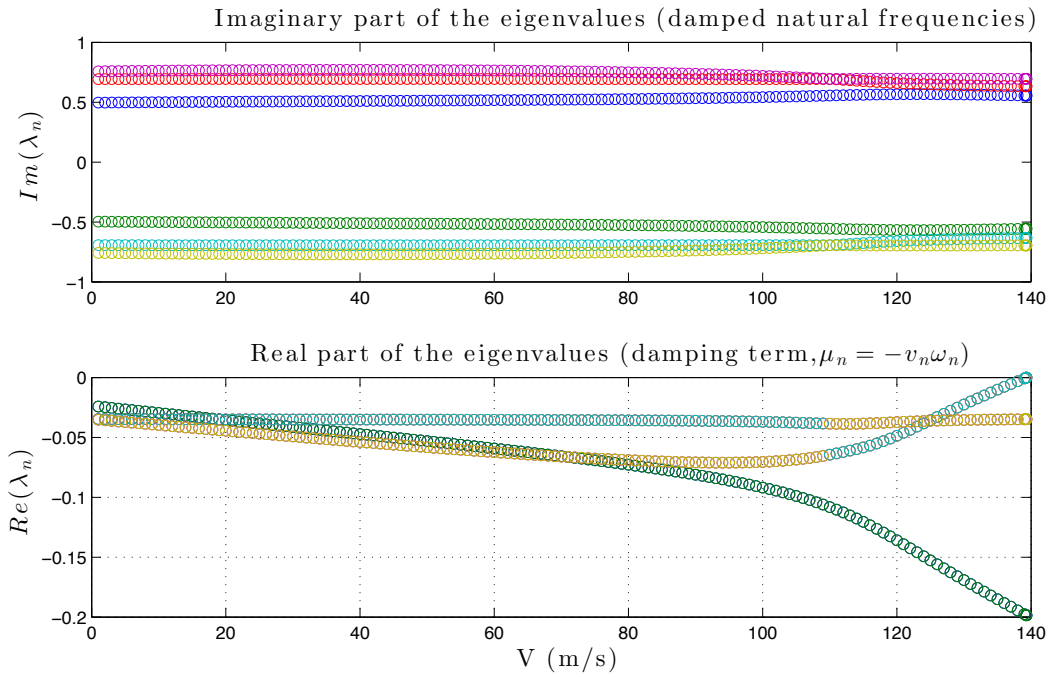

Figure 7.11: Development of the eigenvalue solution for cross section $BS20GV$ with mode combination 5, 11 and 14.

Appendix D.7 this is illustrated where it can be seen that the governing modes have a lower mode number. This reduces the frequency ratio of the modes responsible for flutter, and may provide a lower critical velocity. Since the distance between the cable planes has been increased by 10 m compared to *Analysis* $BS20$ one may expect that the critical velocity would increase since the stiffness provided by the cables increased, but this is not the case. This may be due to the increase in MOI which balance out the increase in torsional stiffness. But the main reason is probably due to the lack of guide vanes at the lower edges of the girders. In [11] this has been stated from experiments which show significant increase in critical velocity when guide vanes are mounted on the cross sections. One other reason may be due to the polynomial fitting for the derivative A_2^*. As can be seen from Figure 7.6 on page 71 the extrapolation of A_2^* seems to be unreasonable outside the experimental range, providing less aerodynamic damping associated with torsional motion. The reduced critical velocity for this cross section is 16.2, which is more than twice the maximum value extracted from experiments. This indicates that the value for A_2^* is positive at this reduced velocity, and may give unreasonable results. At least they are on the safe side. All the other derivatives are also extrapolated outside the experimental range and strengthen the uncertainties in the results.

The development of the eigenvalue solution using mode 6, 11 and 13 is given in Figure 7.12 on page 87. It can be seen that zero damping occurs for the vertical mode, indicating that the critical frequency is on the vertical branch solution. At a wind speed of 60 m/s the frequency of motion has been found to be about 0.7 when including modes 6, 11 and 13 in the calculations. This gives a reduced critical velocity of 11.4 which is just outside the

Table 7.11
Eigenvalue solution using cross section BS30 with a distance of $30m$ between each box-girder. The cross section has been tested without guide vanes. The values in parenthesis are found from the eigenvalue routine created by the author.

Mode combination	Critical Velocity V_{CR} (m/s)	Critical frequency ω_{CR} (rad/s)	Reduced velocity V_{red}
30 modes	82.2	0.675	16.2
20 modes	82.2	0.675	16.2
15 modes	82.2	0.676	16.2
	(37.0)	(0.934)	(5.3)
4.vert + 4 torsional	82.2	0.676	16.2
4,6,11,13 and 14	82.3	0.673	16.3
6,11 and 13	82.3	0.673	16.3
	(82.3)	(0.673)	(16.3)
6 and 11	84.7	0.669	16.9
	(84.7)	(0.669)	(16.9)
6 and 13	94.2	0.688	18.3
	(94.2)	(0.688)	(18.3)
11 and 13	94.7	0.768	16.4
11	104.6	0.746	18.3

experimental range for derivatives $H_n^*, A_n^*, n \in \{1, 4\}$, ranging up to about 10.1, see Table C.3. For the other derivatives, ranging to about 7, the extrapolations are more uncertain. It may be concluded that this cross section provides a stability limit above the design critical velocity based on the above arguments.

Table 7.12
Shape-wise similarity of modes for cross section $BS30/BS30GV$.

Mode combination	Shape-wise similarity $\psi_{z\theta}$
4 and 10	0.98
4 and 14	0.97
6 and 11	0.96
6 and 13	0.98
12 and 11	0.11
12 and 13	0.02
15 and 10	0.03
15 and 14	0.04

Results from the eigenvalue solution using cross section BS30GV are shown in Table 7.13. Values in parenthesis are extracted using the created routine given in Appendix E.4.1.

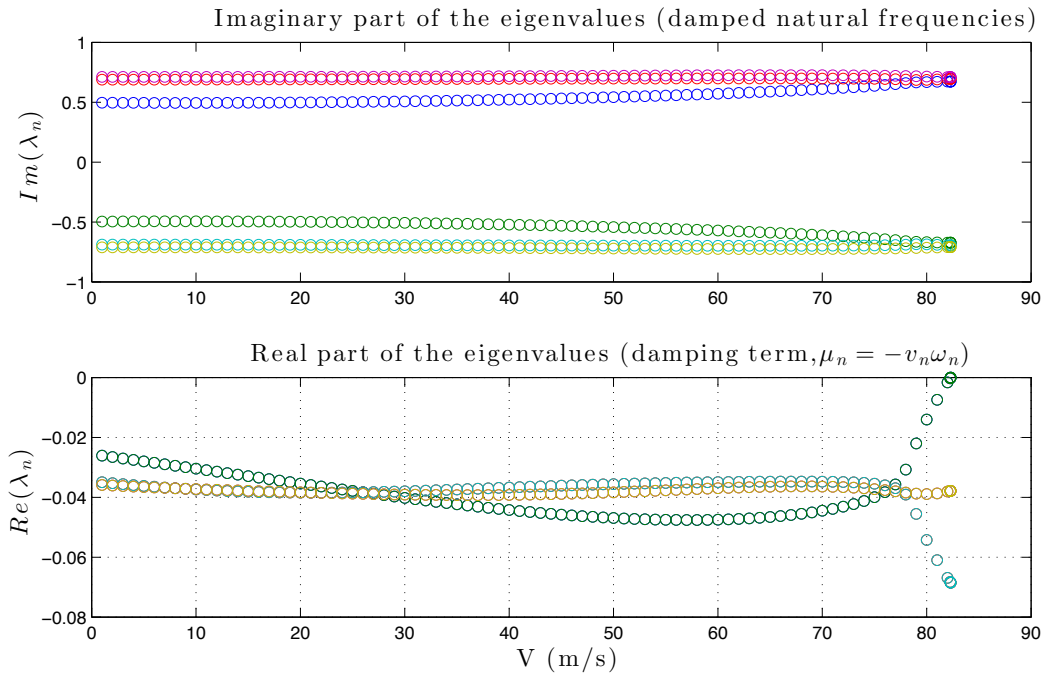

Figure 7.12: Development of the eigenvalue solution for cross section $BS30$ with mode combination 6, 11 and 13.

As can be seen the routine does not give same results for this configuration as for the provided eigenvalue routine. Improvements in the routine are needed. All dimensions are the same as for cross section $BS30$. In addition this cross section has guide vanes mounted to the top of the crossbeams. This analysis is referred to as *Analysis* $BS30GV$. As the table shows, mode 6, 11 and 13 contributes significantly to the critical velocity also in this analysis, but including modes 4 and 10 reduces the critical velocity from 194.6 m/s to 188.1 m/s and the solution converges. This is because of the shape-wise similarity of mode 4 and 10 according to Table 7.12 on the preceding page. When including 20 modes in the calculation the critical velocity shows a value higher than the exact value. This may be due to some dissimilar mode shapes, e.g. mode 12 and 11 which is weakly shape-wise similar, and where the vertical frequency exceeds the torsional frequency. These observations indicates that this is a multimode-coupled flutter phenomenon were several vertical and torsional modes contribute, but were mode 6, 11 and 13 contributes significantly. It can be seen that for this case including both mode 11 and 13 has a stabilizing effect since the stability limit increases. The opposite effect was shown for $BS30$.

The development of the eigenvalue solution using mode 4, 6, 11, 13 and 14 is given in Figure 7.13 on page 89. The critical frequency has been found to be 0.713 rad/s and from the figure, indications suggests that the critical frequency is on one of the vertical branches. This is confirmed as the damped frequencies of the vertical modes exceed the undamped frequencies of the torsional modes. The reduced critical velocity is high for this analysis, as high as 35.1 when 30 modes are considered. This is obviously to high for these results to be reliable. But this cross section can be said to at least give a higher

Table 7.13
Eigenvalue solution using cross section BS30GV with a distance of $30m$ between each box-girder. The cross section has been tested with guide vanes. The values in parenthesis are found from the eigenvalue routine created by the author.

Mode combination	Critical Velocity V_{CR} (m/s)	Critical frequency ω_{CR} (rad/s)	Reduced velocity V_{red}
30 modes	188.4	0.715	35.1
20 modes	190.1	0.720	35.2
15 modes	189.4	0.717	35.2
	(158.0)	(0.833)	(25.3)
4 vert. + 4 torsional	189.4	0.717	35.2
4,6,11,13 and 14	188.1	0.713	35.2
	(162.4)	(0.795)	(27.2)
4,6,10,11,13,14	187.0	0.710	35.1
6,11,13	194.6	0.792	32.8
6 and 13	180.6	0.744	32.4
6 and 11	185.3	0.761	32.5

critical velocity then the other cross sections. In the vicinity of the design critical velocity the frequency of motion is found to be about 0.7, giving a reduced critical velocity of 11.4. This is within the experimental range, and Figure 7.7 on page 72 shows that the polynomials fit well to the data at this reduced velocity. The biggest discrepancy is for A_2^* which underestimates the torsional damping, but this is on the safe side. This indicates that any stability problem due to strong wind below the design critical wind velocity is of no concern for this cross section.

7.4 Importance of aerodynamic derivatives

I the previous section the reliability of the results was discussed in relation with the aerodynamic derivatives. In order to get satisfactory and reliable results it is crucial to predict the self-exited forces as accurately as possible. Finding the most important derivatives is therefore an important task. This has been investigated for cross section $2TFGP$ and $BS15GV$ by following the procedure in Øiseth et al. [26]. Here the aerodynamic derivatives have been scaled separately by a factor ranging 0-1.6, and the change in stability limit has been studied. Figure 7.14 on page 90 shows the results when scaling the aerodynamic derivatives given for cross section $2TFGP$. The results are given when including modes 5, 11, 13 and 14. With an angle of incidence of 3^o, which was identified as giving a flutter phenomenon, the figure shows that the most important derivatives are A_1^*, A_3^*, H_3^* and to some extent H_1^*. It is noticeable that by scaling A_2^* no significant changes were observed, which was unexpected since this derivative provides aerodynamic damping associated with torsional motion. It can be seen from the figure that by scaling H_3^*

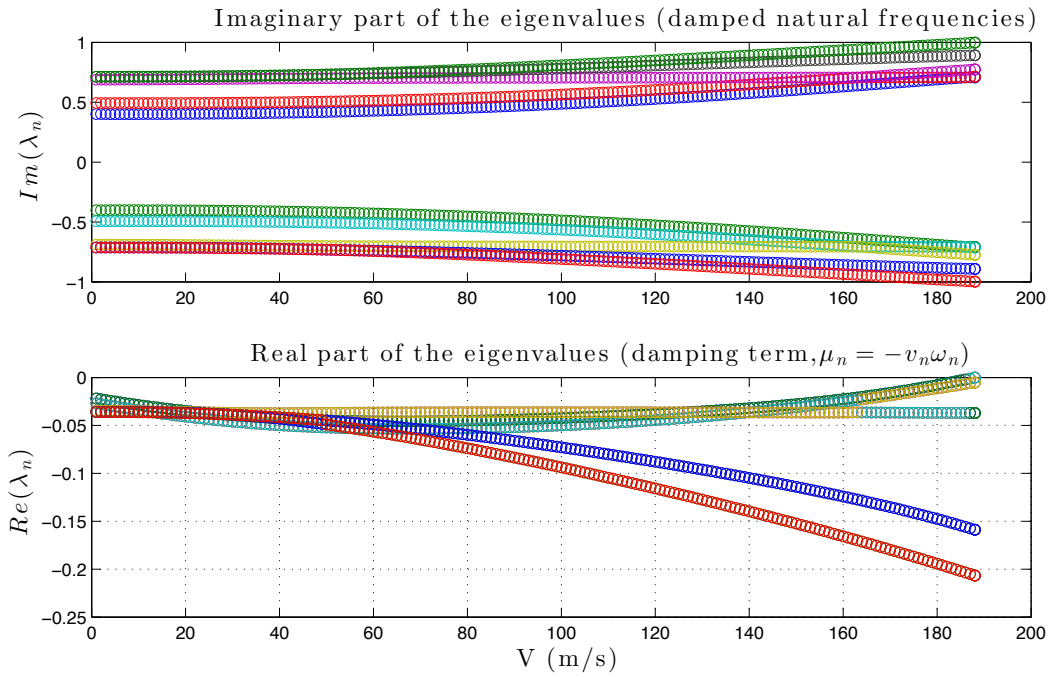

Figure 7.13: Development of the eigenvalue solution for cross section $BS30GV$ with mode combination 4, 6, 11, 13 and 14.

by a factor 0.2 the stability limit increases by over 60 %, this is because the values for H_3^* are positive (see Figure 7.1) and will provide negative aerodynamic forces when the forces are moved to the left side of the equation system as given in Equation 4.40 on page 33. When the angle of incidence is 0^o the cross section indicated a static divergence instability phenomenon. As this phenomenon is a static instability problem in torsion the importance of any aerodynamic derivative associated with torsional stiffness would be expected. As can be seen from Figure 7.14 this is confirmed from the curve given for A_3^*, indicated by the purple line. As can be seen the stability limit is increased by over 120 % when scaling the derivative by 0.2. This is because the value of A_3^* is positive, and will provide negative torsional stiffness to the system. Obviously this is not a reliable result since static divergence indicates a critical frequency equal to zero rendering a reduced critical velocity infinitely large, but the trend is clear.

Figure 7.15 on the following page shows the results when scaling the aerodynamic derivatives for cross section $BS15GV$. Results are given when including modes 5, 12 and 14. As can be seen the most important derivatives are A_1^*, A_2^*, H_3^*, H_1^* and to some extent A_3^*. Compared to $2TFGP$ the importance of A_2^* are significant and by eliminate this derivative in the calculation decreases the stability limit by 20 %, implying a reduction of the critical velocity from 121 m/s to about 97 m/s. From Figure 7.4 on page 68 it can be seen that for the most important derivatives found above the polynomials fit well to the data especially in the range of the data obtained in experiments. Outside this range the polynomials obviously gives uncertain results, as mentioned earlier.

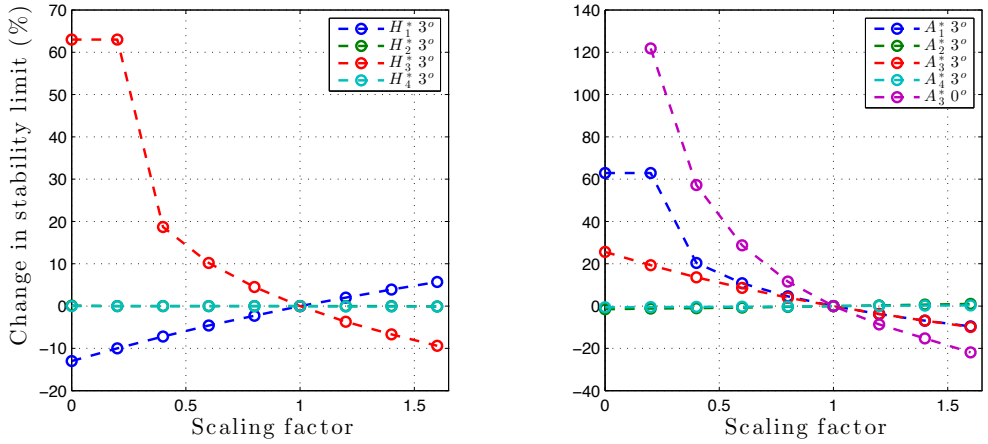

Figure 7.14: Change of stability limit when scaling aerodynamic derivatives separately for cross section $2TFGP$. The plot to the left shows results for derivatives $H_n^*, n \in \{1,2,3,4\}$ while the plot to the right shows results for derivatives $A_n^*, n \in \{1,2,3,4\}$. The purple line show the results from the 0^o wind case.

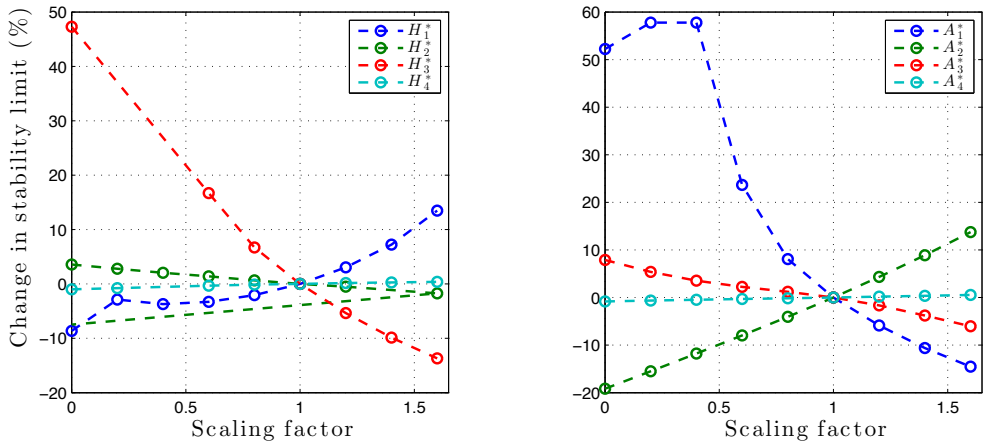

Figure 7.15: Change of stability limit when scaling aerodynamic derivatives separately for cross section $BS15GV$. The plot to the left shows results for derivatives $H_n^*, n \in \{1,2,3,4\}$ while the plot to the right show results for derivatives $A_n^*, n \in \{1,2,3,4\}$.

7.5 Flutter solution and comparative results

In section 7.3 the aeroelastic stability limit was found by solving the complex eigenvalue problem, an exact solution when all the vibration modes are included in the solution. For engineering purposes and as preliminary investigations, simplified solutions has been important in order to predict the stability limit, especially flutter. In the following a simplified solution is tested on the different cross sections presented in the previous sections, also called the flutter equations. They were derived in Section 4.3, and the solution routines for this problem is given in Appendix E.3 and E.4.2. As the eigenvalue solutions has shown the instability limit is highly dependent of the shape-wise similarity of the vertical

and torsional modes. In addition the frequency ratio between modes likely to cause flutter may be of great importance for which modes contributing the most. But this factor is not that clear from the solutions presented in Section 7.3. This is investigated further in the following. The flutter solutions are compared to the eigenvalue solution provided and the one presented in Appendix E.4.1, when using only two modes. Since the different solutions are developed from the same starting point they should provide approximately the same answer. When using the flutter equations it is necessary to find the modal equivalent distributed mass and mass moment of inertia. These parameters were estimated for cross section $2TFGP$ in Section 6.5. For the cross sections from $Brusymfonien$ the distributed mass and MOI was given and presented in Table 7.1 on page 67. As for cross section $2TFGP$ the modal equivalent distributed mass $\tilde{m}_z$ and MOI $\tilde{m}_\theta$ has been calculated in the centre of the sailing lane where the hangers are at their shortest and the cables are horizontal. The calculations are summarized in Table 7.14. The solution routines for solving the flutter equations are given in Appendix E.3 and E.4.2.

Table 7.14
Modal equivalent distributed mass and MOI for cross sections from $Brusymfonien$. MOI is found about the vertical centre in the crossbeams.

	Element	Distributed mass one plane (kg/m)	Radius of gyration d (m)	Mass moment of inertia (kgm^2/m)
BS15GV	Cables	12,330.8	11.48	1,625,081.1
	Hangers	208.8	11.48	27,517.8
	Girder & Crossbeam	9,940		741,600.0
	Total	$\tilde{m}_z$=22,480		$\tilde{m}_\theta$=2,394,200
BS20GV	Cables	12,330.8	13.98	2,409,936.5
	Hangers	208.8	13.98	40,808.0
	Girder & Crossbeam	10,040		938,000.0
	Total	$\tilde{m}_z$=22,580		$\tilde{m}_\theta$=3,433,700
BS30/ BS30GV	Cables	12,330.8	18.98	4,442,052.3
	Hangers	208.8	18.98	75,218.2
	Girder & Crossbeam	10,770		1,818,700.0
	Total	$\tilde{m}_z$=23,310		$\tilde{m}_\theta$=6,336,000

7.5.1 Cross section 2TFGP

In this section the cross section $2TFGP$ has been tested by the use of the flutter equations. The width of one girder is given as $B^* = 10\ m$, and the still-air structural properties in this analysis are assumed to be $\omega_z = 0.5$ rad/s, $\omega_\theta = \gamma\omega_z\ rad/s$, $\xi_z = 0.005$ and $\xi_\theta =$

0.005. The modal equivalent distributed mass and MOI are found from Section 6.5 as $\tilde{m}_z$ = 25,700 kg/m and $\tilde{m}_\theta$ = 2,840,000 kgm^2/m. The still-air vibration modes are assumed to be dominated by either a vertical component ϕ_z or a torsional component ϕ_θ, and are related by the shape-wise similarity $\psi_{z\theta}$. As the multimode eigenvalue solution indicated the stability phenomenon was static divergence for the 0^o wind case. This would indicate that the flutter equations would not give any solution at a frequency ratio of about 1.4 or below. This can be seen from Table 7.4 and Table 7.8 where mode 11 contributes to the static stability limit and has a frequency of about 0.7 rad/s, giving a frequency ratio of about 1.4 when using the vertical frequency of mode 5 (0.492 rad/s). Critical velocities when the eigenvalue solution is used, are presented in parenthesis in Table 7.15. The corresponding critical frequencies are given in table 7.16 on the facing page. Here the solutions are given as a function of the frequency ratio γ between the modes and the shape-wise similarity $\psi_{z\theta}$. As aspected the flutter equations gave no solution at a low frequency ratio of about 1.4, indicated by lines at the top of each cell. The flutter solution is illustrated in Figure 7.16 on page 94, and as can be seen the real root solution have two positive roots for each velocity iteration, and the imaginary root solution has only one positive root. No flutter will occur because no one of the real curves crosses the imaginary curve.

Table 7.15
Critical velocities for cross section $2TFGP$ at 0^o of incidence of the wind flow given as a function of the shape-wise similarity and the frequency ratio between the two modes. The values in parenthesis are obtained by using the eigenvalue solution with two modes. The values found by the flutter equations are given in top of each cell. Empty cells indicate that no solution was found from the flutter equations.

shapewise similarity $\psi_{z\theta}$	Frequency ratio γ							
	1.4	1.5	1.6	1.8	2.0	2.2	2.4	3.0
1.0	– (124.4)	117.7 (133.2)	124.6 (132.9)	143.3 (147.3)	162.7 (165.7)	181.9 (184.4)	200.9 (203.2)	256.8 (258.6)
0.9	– (124.3)	– (133.1)	– (141.9)	147.8 (156.6)	166.2 (170.9)	185.0 (188.7)	203.8 (206.9)	259.7 (262.0)
0.8	– (124.3)	– (133.1)	– (141.9)	– (159.5)	172.4 (177.1)	189.9 (194.6)	208.1 (212.2)	263.5 (264.9)
0.6	– (124.3)	– (133.1)	– (141.9)	– (159.4)	– (177.0)	– (194.6)	– (212.2)	283.9 (264.9)

As the tables show the stability limit increases when the frequency ratio increases. The interesting about these results is that the solutions indicate that the instability phenomenon changes character from static divergence to flutter when the frequency ratio reach a certain value. This is indicated from Table 7.16 where the critical frequency changes from zero to over 0.5 rad/s somewhere between a frequency ratio of 1.5 and 1.6 (1.4 and 1.5 for the flutter solution) for a shape-wise similarity equal to 1.0. The frequency ratio onset

Table 7.16
Critical frequencies for cross section 2TFGP at 0^o of incidence of the wind flow given as a function of the shape-wise similarity and the frequency ratio between the two modes. The values in parenthesis are obtained by using the eigenvalue solution with two modes. Empty cells indicate that no solution was found from the flutter equations.

shapewise similarity $\psi_{z\theta}$	Frequency ratio γ							
	1.4	1.5	1.6	1.8	2.0	2.2	2.4	3.0
1.0	– (0.0)	0.53 (0.0)	0.54 (0.54)	0.56 (0.55)	0.57 (0.57)	0.59 (0.59)	0.61 (0.61)	0.67 (0.66)
0.9	– (0.0)	– (0.0)	– (0.0)	0.55 (0.55)	0.57 (0.57)	0.59 (0.58)	0.60 (0.60)	0.66 (0.65)
0.8	– (0.0)	– (0.0)	– (0.0)	– (0.0)	0.56 (0.0)	0.58 (0.0)	0.60 (0.0)	0.65 (0.0)
0.6	– (0.0)	– (0.0)	– (0.0)	– (0.0)	– (0.0)	– (0.0)	– (0.0)	0.64 (0.0)

of this change in stability character also seems to increase as the shape-wise similarity decreases. No clear reason for this has not been found, and is left for further investigations. It is also seen that when the critical frequency equals zero the critical velocity doesn't change when reducing the shape-wise similarity, obviously because there is no coupling between the two modes and the stability limit is only dependent on the torsional mode and its frequency. I.e. a higher torsional frequency provides a higher critical velocity. Comparing the bimodal eigenvalue solution with the multimode solution given in Table 7.4 on page 75, it can be shown that the bimodal solution gives an estimate of the critical velocity well below the multimode solution, 124.4 m/s when assuming a torsional frequency of 0.7 rad/s ($\gamma = 1.4$) compared to 142 m/s from the multimodal solution. I.e. the bimodal approach provides a conservative result, at least when assuming a low frequency ratio. Although it must be mentioned that the critical velocity indicated by static divergence cannot be said to be a realistic value since the frequency approaches zero during the iteration process, meaning that the reduced velocity approaches infinity. But at least it can be stated that flutter will be no problem below this velocity.

7.5.2 Cross section BS15GV

The cross section referred to as $BS15GV$ has also been tested by the use of flutter equations. The width B^* of one girder is 7.5 m and the total width between the cable planes is 22.98 m. The still air properties are assumed to be $\omega_z = 0.5$ rad/s, $\omega_\theta = \gamma\omega_z$ rad/s, $\xi_z = 0.005$ and $\xi_\theta = 0.005$. The modal equivalent distributed mass and MOI are found from Table 7.14 as $\tilde{m}_z = 22{,}480$ kg/m and $\tilde{m}_\theta = 2{,}394{,}000$ kgm^2/m. This cross section has guide vanes mounted to the girders. As before the still-air vibration modes are assumed to be dominated by either a vertical component ϕ_z or a torsional component ϕ_θ,

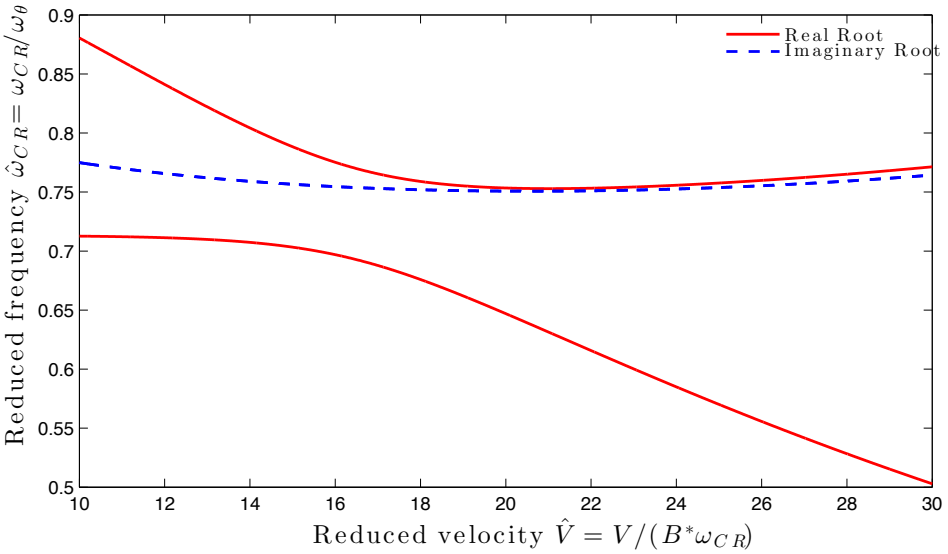

Figure 7.16: Development of the flutter solution for cross section $2TFGP$. Red curves represent the positive real roots of the flutter equations, while the blue dashed line represents the only positive imaginary root. Results are shown for a shape-wise similarity $\psi_{z\theta} = 1$, and a frequency ratio $\gamma = 1.4$.

and are related by the shape-wise similarity $\psi_{z\theta}$. The critical velocities and corresponding critical frequencies are presented in Table 7.17 on the next page and 7.18 on page 96 respectively. Here the solutions from the flutter equations are given at the top of each cell, while the eigenvalue solutions are given in parenthesis. The percentage difference between the flutter- and eigenvalue solution is given in the third row in each cell. The eigenvalue solutions using the routine given in Appendix E.4.1 are given at the bottom of each cell, and as can be seen this routine provides accurate results for a bimodal analysis when using this cross section.

As expected the critical velocity increases as the frequency ratio γ increases or when the shape-wise similarity $\psi_{z\theta}$ decreases. The flutter equations gives critical velocities that deviate insignificantly from the eigenvalue solution, and any discrepancy may be due to the fact that the solutions are iterative processes and convergence criteria's influence the final results. In Section 7.3.2 the eigenvalue solution gave a critical velocity of 114.9 m/s when including mode 5 and 14, identified as one vertical and one torsional mode with shape-wise similarity equal to 0.83 and frequency ratio of about 1.6. From Table 7.17 this would indicate a critical velocity of about 90 m/s from the flutter solution. I.e. the flutter solution underestimates the critical velocity by approximately 20 %, which is a conservative result. This may be due to differences in structural mass but also that the reduced velocities are different, rendering different values of the aerodynamic derivatives. In the flutter solution the mass has been assumed evenly distributed along the girders, which is an engineering approximation. The modal equivalent mass has been shown to be dependent on the mode shapes, and the degree of coupling between other directions and the cables. This is not accounted for in the flutter equations.

Table 7.17
Critical velocities for cross section $BS15GV$ given as a function of the shape-wise similarity and the frequency ratio between the two modes. The value at the top in each cell was found using the flutter equations. The values in parenthesis were found by using the eigenvalue solution, while the percentage difference between the flutter solution compared to the eigenvalue solution is given in the third row in each cell. The value at the bottom in each cell was found by using the eigenvalue routine created by the author.

shapewise similarity $\psi_{z\theta}$	Frequency ratio γ							
	1.4	1.5	1.6	1.8	2.0	2.2	2.4	3.0
1.0	70.7	78.8	86.6	101.5	115.9	129.9	143.8	184.4
	(70.9)	(79.0)	(86.8)	(101.7)	(116.2)	(130.3)	(144.1)	(184.7)
	-0.3%	-0.3%	-0.2%	-0.3%	-0.2%	-0.2%	-0.2%	-0.2%
	70.9	79.0	86.8	101.8	116.2	130.3	144.1	184.7
0.9	72.8	81.1	89.1	104.4	119.2	133.7	147.9	189.6
	(73.0)	(81.3)	(89.3)	(104.7)	(119.5)	(134.0)	(148.2)	(190.0)
	-0.3%	-0.3%	-0.3%	-0.3%	-0.2%	-0.2%	-0.2%	-0.2%
	73.0	81.3	89.3	104.7	119.5	134.0	148.3	190.1
0.8	75.2	83.7	91.9	107.7	123.0	137.9	152.6	195.7
	(75.4)	(83.9)	(92.2)	(108.0)	(123.3)	(138.3)	(152.9)	(196.0)
	-0.3%	-0.3%	-0.3%	-0.3%	-0.3%	-0.2%	-0.2%	-0.2%
	75.4	83.9	92.2	108.0	123.3	138.3	152.9	196.1

The development of the flutter solution is shown to the left in Figure 7.17 on the next page. The solution is plotted for a frequency ratio of 1.4 and a shape-wise similarity $\psi_{z\theta}$ equal to 1. The critical velocity is defined as the intersection point between the real and imaginary root curves that provides the lowest velocity value. The reduced critical velocity as a function of the frequency ratio γ is shown in the right plot of Figure 7.17. Here, the reduced velocity is given as a function of the frequency ω_θ ($\tilde{V}_{cr} = V_{cr}/B^*\omega_\theta$). As can be seen the reduced critical velocity increases as the frequency ratio increases.

7.5.3 Cross section BS20GV

The width of one girder is 7.5 m and the total width between the cable planes is 27.96 m. The structural properties are assumed to be $\omega_z = 0.5$ rad/s, $\omega_\theta = \gamma\omega_z\ rad/s$, $\xi_z = 0.005$ and $\xi_\theta = 0.005$. The modal equivalent distributed mass and MOI are found from Table 7.14 as $\tilde{m}_z$ = 22,580 kg/m and $\tilde{m}_\theta$ = 3,433,700 kgm^2/m. This cross section has guide vanes mounted to the cross section. The still-air vibration modes are assumed to be dominated by either a vertical component ϕ_z or a torsional component ϕ_θ, and are related by the shape-wise similarity $\psi_{z\theta}$. Table 7.19 on page 97 shows the critical velocities found for cross section $BS20GV$ using the flutter equations. Here, the flutter solutions are given at the top of each cell and the eigenvalue solution is given in parenthesis. The percentage

Table 7.18
Critical frequencies for cross section $BS15GV$ given as a function of the shape-wise similarity and the frequency ratio between the two modes. The value at the top in each cell was found using the flutter equations. The values in parenthesis were found by using the eigenvalue solution, while the percentage difference between the flutter solutions compared to the eigenvalue solution is given in the third row in each cell. The value at the bottom in each cell was found by using the eigenvalue routine created by the author.

shapewise similarity $\psi_{z\theta}$	Frequency ratio γ							
	1.4	1.5	1.6	1.8	2.0	2.2	2.4	3.0
1.0	0.66 (0.66) 0.0% 0.66	0.70 (0.70) 0.0% 0.70	0.75 (0.75) 0.1% 0.75	0.83 (0.83) 0.1% 0.83	0.91 (0.91) 0.1% 0.91	1.00 (1.00) 0.1% 1.00	1.08 (1.08) 0.1% 1.08	1.34 (1.34) 0.1% 1.34
0.9	0.66 (0.66) 0.0% 0.66	0.70 (0.70) 0.1% 0.70	0.74 (0.74) 0.1% 0.74	0.82 (0.82) 0.1% 0.82	0.90 (0.90) 0.1% 0.90	0.99 (0.99) 0.1% 0.99	1.07 (1.07) 0.1% 1.07	1.33 (1.32) 0.1% 1.32
0.8	0.66 (0.66) 0.1% 0.66	0.70 (0.70) 0.1% 0.70	0.74 (0.73) 0.1% 0.73	0.82 (0.81) 0.1% 0.81	0.90 (0.90) 0.1% 0.90	0.98 (0.98) 0.1% 0.98	1.06 (1.06) 0.1% 1.06	1.31 (1.31) 0.1% 1.31

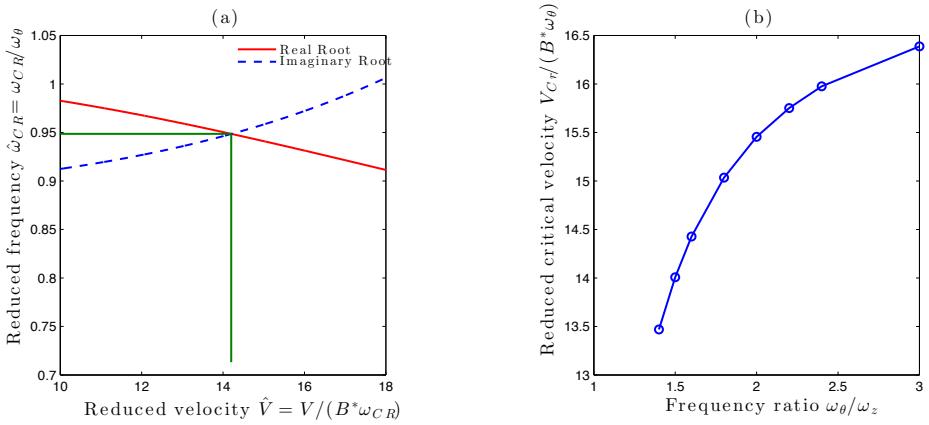

Figure 7.17: Development of the flutter solution given for cross section $BS15GV$. Shape-wise similarity is equal to $\psi_{z\theta} = 1$: (a) Development of the real and imaginary part of the solution at a frequency ratio of $\gamma = 1.4$. The critical values are identified where the two curves intersect, indicated by green lines. (b) Reduced critical velocity ($\tilde{V}_{cr} = V_{cr}/B^*\omega_\theta$) as a function of the frequency ratio between the torsional and vertical mode.

between the flutter solution and the eigenvalue solution is given in the third row in each cell. The eigenvalue solutions using the solution routine presented in Appendix E.4.1 is

given at the bottom in each cell. The corresponding critical frequencies are given in the same manner in Table 7.20 on the next page.

Table 7.19
Critical velocities for cross section $BS20GV$ given as a function of the shape-wise similarity and the frequency ratio between the two modes.

shapewise similarity $\psi_{z\theta}$	Frequency ratio γ							
	1.4	1.5	1.6	1.8	2.0	2.2	2.4	3.0
1.0	110.5 (110.5) 0.0% 110.5	120.9 (120.9) 0.0% 120.9	131.3 (131.3) -0.1% 131.3	151.8 (151.9) -0.1% 151.9	171.9 (172.0) -0.1% 172.0	191.7 (191.9) -0.1% 191.9	211.3 (211.5) -0.1% 211.5	269.2 (269.4) -0.1% 269.9
0.8	114.2 (111.7) 2.3% 114.3	124.8 (122.1) 2.2% 124.8	135.4 (132.6) 2.1% 135.5	156.4 (153.3) 2.0% 156.5	177.1 (173.6) 2.0% 177.2	197.5 (193.6) 2.0% 197.6	217.6 (213.4) 2.0% 218.0	277.2 (271.8) 2.0% 277.4

As the tables show the critical velocity increases as the frequency ratio between the vertical and torsional mode increases, and increases as the shape-wise similarity decreases. The percentage error of critical velocities between the flutter solution and the eigenvalue solution are insignificant, but increase as $\psi_{z\theta}$ decreases. This may be due to the procedure used for calculating the modal matrices from the bimodal eigenvalue approach. How the mode shapes are assumed in order to get a shape-wise similarity equal to those in the tables influence the values of the mode shape integrals and thereby the values in the modal matrices. In Section 7.3.3 the eigenvalue solution gave a critical velocity of 140 m/s when including mode 5 and 14 in the calculations, which was close to the exact solution. The shape-wise similarity and frequency ratio between these two modes has been found to be approximately $\psi_{z\theta} = 0.88$ and $\gamma = 1.5$ from Tables 7.8 and 7.10 respectively. From this, Table 7.19 indicates a critical velocity between 121 m/s and 125 m/s, i.e. an underestimation of about 10-13 %. As mentioned earlier this may have to do with differences in mass properties and the values for the aerodynamic derivatives at different values of the reduced velocity.

7.5.4 Cross section BS30/BS30GV

These two cross sections are identical regarding cross sectional shape, stiffness and mass properties. The only difference is that $BS30$ doesn't have guide vanes mounted to the cross section. The width of one girder is 7.5 m and the total width between the cable planes is 37.96 m. The structural properties are assumed to be $\omega_z = 0.5$ rad/s, $\omega_\theta = \gamma\omega_z$ rad/s, $\xi_z = 0.005$ and $\xi_\theta = 0.005$. The modal equivalent distributed mass and MOI are found from Table 7.14 as $\tilde{m}_z = 23{,}310$ kg/m and $\tilde{m}_\theta = 6{,}336{,}000$ kgm^2/m. The still-air vibration modes are assumed to be dominated by either a vertical component ϕ_z or a

Table 7.20
Critical frequencies for cross section $BS20GV$ given as a function of the shape-wise similarity and the frequency ratio between the two modes.

shapewise similarity $\psi_{z\theta}$	Frequency ratio γ							
	1.4	1.5	1.6	1.8	2.0	2.2	2.4	3.0
1.0	0.62	0.65	0.68	0.75	0.82	0.89	0.96	1.17
	(0.62)	(0.65)	(0.68)	(0.75)	(0.82)	(0.88)	(0.95)	(1.17)
	0.1%	0.1%	0.1%	0.1%	0.1%	0.2%	0.2%	0.2%
	0.62	0.65	0.68	0.75	0.82	0.88	0.95	1.17
0.8	0.61	0.64	0.68	0.74	0.80	0.87	0.94	1.14
	(0.62)	(0.65)	(0.68)	(0.75)	(0.81)	(0.88)	(0.95)	(1.16)
	-0.6%	-0.7%	-0.8%	-0.9%	-1.0%	-1.1%	-1.1%	-1.3%
	0.61	0.64	0.67	0.74	0.80	0.87	0.94	1.14

torsional component ϕ_θ, and are related by the shape-wise similarity $\psi_{z\theta}$.

Table 7.21
Critical velocities for cross section $BS30$ given as a function of the shape-wise similarity and the frequency ratio between the two modes. The value at the top in each cell was found using the flutter equations. The values in parenthesis were found by using the eigenvalue solution. The value at the bottom was found by using the eigenvalue routine created by the author.

shapewise similarity $\psi_{z\theta}$	Frequency ratio γ							
	1.4	1.5	1.6	1.8	2.0	2.2	2.4	3.0
1.0	78.3	88.1	97.6	97.8	102.2	109.8	118.1	144.6
	(78.3)	(88.2)	(97.7)	(96.0)	(101.4)	(109.1)	(117.5)	(144.1)
	-0.1%	-0.1%	-0.1%	1.9%	0.8%	0.6%	0.6%	0.4%
	78.1	87.9	97.4	96.0	101.0	109.1	117.5	144.1
0.8	77.4	78.1	80.2	87.1	95.0	103.5	112.1	138.6
	(76.4)	(77.2)	(79.6)	(86.6)	(94.6)	(103.0)	(111.7)	(138.2)
	1.3%	1.1%	0.8%	0.6%	0.4%	0.4%	0.4%	0.3%
	76.5	77.2	79.6	86.6	94.6	103.1	111.7	138.2
0.6	(67.2)	(70.5)	(74.3)	(82.3)	(90.6)	(99.2)	(107.8)	(133.9)
0.4	(63.2)	(67.0)	(71.1)	(79.3)	(87.7)	(96.2)	(104.8)	(130.5)

Table 7.21 shows the critical velocities given for cross section $BS30$ as a function of the frequency ratio and the shape-wise similarity. The flutter solution is given at the top in each cell while the eigenvalue solutions are given in parenthesis. The percentage difference between the solutions is given in the third row in each cell. The eigenvalue results obtained from the routine presented in Appendix E.4.1 is given at the bottom

Table 7.22
Critical velocities when different derivatives are scaled by a factor zero: Cross section $BS30$. Values in parenthesis are the values from the eigenvalue solution without any scaling.

shapewise similarity $\psi_{z\theta}$	$H_2^* = 0$		$H_3^* = 0$		$A_1^* = 0$		$A_4^* = 0$		$H_2^* = H_4^* = 0$	
	Frequency ratio γ									
	1.4	1.5	1.4	1.5	1.4	1.5	1.4	1.5	1.4	1.5
1.0	78.3 (78.3)	88.0 (88.2)	57.9	62.1	57.1	61.4	80.2	89.0	77.4	78.4
0.8	81.2 (76.4)	86.8 (77.2)	58.0	62.2	57.3	61.6	85.3	94.9	69.3	72.6

in each cell. The corresponding critical frequencies are given in the same manner in Table 7.23 on the next page. As can be seen from Table 7.21 the solutions gave some unexpected results. While the previous cross sections showed increasing critical velocities as the shape-wise similarity decreased, this cross section shows the opposite. This may have to do with the shapes of the aerodynamic derivatives. From the contents of the impedance matrix, see Equations 4.28 on page 30 to 4.31 on page 31, it can be seen that the terms dependent on the shape-wise similarity are the off-diagonal terms associated with aerodynamic derivatives H_2^*, H_3^*, A_1^* and A_4^*. Some of these terms are suspected to have a stabilizing effect on the stability limit since reducing their values decreases the critical velocity. A study has been carried out to find the reason for this problem. In Table 7.22 the derivatives mentioned above has been scaled individually by a factor zero. This was done to see which derivatives that increased or decreased the stability limit. As can be seen, H_3^* and A_1^* reduce the stability limit when comparing these values with those in Table 7.21. When H_3^* and A_1^* are zero the stability limit doesn't change when $\psi_{z\theta}$ is reduced, implying that H_2^* and A_4^* have no influence in this reduced velocity range. Since the stability limit doesn't change when either H_3^* or A_1^* are zero, one analysis is carried out when neither of them is scaled. The result is shown in the two last columns. As can be seen the results gives reduced critical velocity when $\psi_{z\theta}$ is reduced. This implies that the unexpected results may be caused by a combination of the values for H_3^* and A_1^*. The strange results are also suspected to have a connection with the polynomial fit for A_2^*. A simple study confirms this possibility. By scaling A_2^* by zero the results will change to giving increased velocity when $\psi_{z\theta}$ is reduced. From about 77 m/s to about 81 m/s when $\psi_{z\theta}$ is reduced from 1.0 to 0.8, using the eigenvalue solution with $\gamma = 1.4$. The flutter solution gave the same results. Since a value of zero for A_2^* is conservative according to Figure 7.6 on page 71, it may be concluded that a bad polynomial fit for A_2^* is the main factor responsible for the unexpected results shown in Table 7.21. This is illustrated in Figure 7.18, where the different derivatives has been scaled separately. It can be seen that by scaling A_2^* by a factor less than 1, the stability limit will increase. This is an opposite effect compared to cross section $BS15GV$, see Figure 7.15 on page 90. As mentioned

this is because A_2^* shows positive values at high reduced velocities, which is shown to be unreasonable. It is concluded that the extrapolation for A_2^* provides overly conservative results when a second order polynomial is fitted to the experimental data.

Table 7.23
Critical frequencies for cross section $BS30$ given as a function of the shape-wise similarity and the frequency ratio between the two modes. The value at the top in each cell was found using the flutter equations. The values in parenthesis were found by using the eigenvalue solution. The value at the bottom was found by using the eigenvalue routine created by the author.

shapewise similarity $\psi_{z\theta}$	Frequency ratio γ							
	1.4	1.5	1.6	1.8	2.0	2.2	2.4	3.0
1.0	0.68 (0.68) -0.2% 0.68	0.72 (0.73) -0.3% 0.72	0.77 (0.77) -0.4% 0.77	0.94 (0.94) 0.0% 0.94	1.04 (1.04) 0.0% 1.04	1.15 (1.15) 0.0% 1.15	1.25 (1.25) 0.0% 1.25	1.56 (1.56) 0.0% 1.56
0.8	0.72 (0.72) -0.3% 0.72	0.78 (0.78) 0.0% 0.78	0.83 (0.83) 0.0% 0.83	0.94 (0.94) 0.0% 0.94	1.04 (1.04) 0.0% 1.04	1.15 (1.15) 0.0% 1.15	1.25 (1.25) 0.0% 1.25	1.56 (1.56) 0.0% 1.56

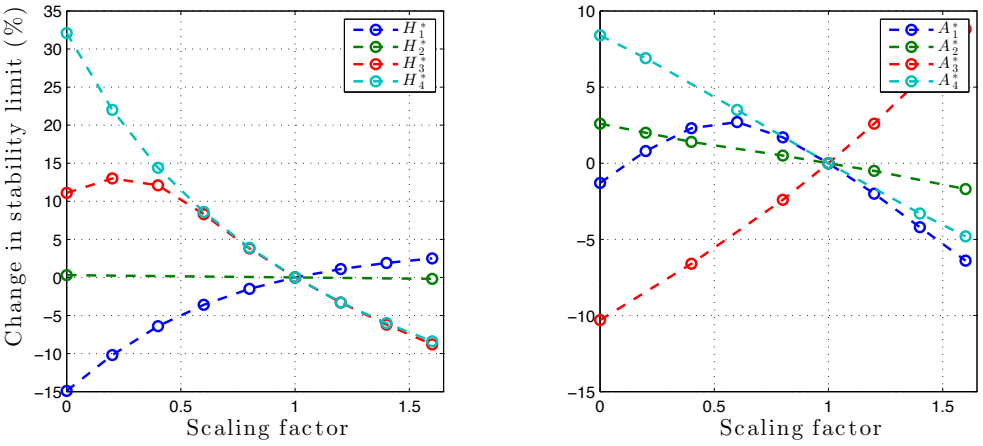

Figure 7.18: Change of stability limit when scaling aerodynamic derivatives separately for cross section $BS30$. The plot to the left shows results for derivatives $H_n^*, n \in \{1,2,3,4\}$ while the plot to the right show results for derivatives $A_n^*, n \in \{1,2,3,4\}$.

The critical velocities and corresponding critical frequencies obtained when using cross section $BS30GV$ are given in Tables 7.24 on the next page and 7.25 on the facing page respectively. The results are given in the same manner as for the previous cross sections but the eigenvalue provided in Appendix E.4.1 has not been presented as this solution showed some numerical instabilities. As can be seen the critical velocity increases with

increasing frequency ratio γ and when the shape-wise similarity $\psi_{z\theta}$ decreases. The lowest eigenvalue solution in Table 7.13 on page 88 were found to be 180.6 m/s using mode 6 and 13 with a shape-wise similarity $\psi_{z\theta} = 0.98$, and a frequency ratio between the modes of about $\gamma = 1.4$. From Table 7.24 this would indicate a critical velocity close to 162 m/s using the eigenvalue solution. This is a conservative result when the mode shapes, modal equivalent distributed mass and MOI has been approximated.

Table 7.24
Critical velocities for cross section $BS30GV$ given as a function of the shape-wise similarity and the frequency ratio between the two modes.

shapewise similarity $\psi_{z\theta}$	Frequency ratio γ							
	1.4	1.5	1.6	1.8	2.0	2.2	2.4	3.0
1.0	160.6 (161.5) -0.6%	172.3 (173.4) -0.6%	183.4 (184.7) -0.7%	204.2 (205.8) -0.8%	223.4 (225.4) -0.8%	241.5 (243.7) -0.9%	258.6 (260.9) -0.9%	317.1 (306.7) 3.4%
0.8	174.1 (175.2) -0.6%	185.6 (187.0) -0.8%	196.6 (198.2) -0.8%	217.2 (219.0) -0.8%	235.8 (238.1) -0.9%	253.1 (255.6) -1.0%	269.1 (271.8) -1.0%	309.1 (313.1) -1.3 %

Table 7.25
Critical frequencies for cross section $BS30GV$ given as a function of the shape-wise similarity and the frequency ratio between the two modes.

shapewise similarity $\psi_{z\theta}$	Frequency ratio γ							
	1.4	1.5	1.6	1.8	2.0	2.2	2.4	3.0
1.0	0.71 (0.71) -0.4%	0.74 (0.74) -0.4%	0.76 (0.77) -0.5%	0.82 (0.82) -0.6%	0.87 (0.88) -0.7%	0.92 (0.93) -0.8%	0.96 (0.97) -0.8%	1.11 (1.10) 1.2%
0.8	0.74 (0.74) -0.4%	0.76 (0.77) -0.6%	0.79 (0.80) -0.6%	0.85 (0.85) -0.7%	0.89 (0.90) -0.8%	0.94 (0.95) -0.8%	0.98 (0.99) -0.9%	1.08 (1.10) -1.2%

7.6 Including quasi-steady theory

In the previous analyses the self-exited forces related to the lateral motion were not included in the calculations, since the aerodynamic derivatives associated with this direction have not been experimentally obtained. For the cross sections from $Brusymfonien$ some of the static coefficients have been obtained during experiments [11]. A simple study has been carried out where these coefficients are introduced in the eigenvalue solution. I.e. the aerodynamic derivatives $H_n^*, A_n^*, n \in \{5, 6\}$ and $P_n^*, n \in \{1, 2..., 6\}$ are

replaced by quasi-steady aerodynamic derivatives. They were derived in Equation 4.15 on page 28 and repeated below for convenience. It can be seen that the derivatives $P_2^* = P_4^* = P_6^* = H_6^* = A_6^* = 0$. The coefficient C'_D is zero.

$$P_1^* = -2\bar{C}_D \frac{D}{B}\left(\frac{1}{K}\right) \quad P_5^* = \left(\bar{C}_L - C'_D \frac{D}{B}\right)\left(\frac{1}{K}\right) \quad P_3^* = C'_D \frac{D}{B}\left(\frac{1}{K}\right)^2$$
$$H_5^* = -2\bar{C}_L\left(\frac{1}{K}\right) \quad A_5^* = -2\bar{C}_M\left(\frac{1}{K}\right) \quad P_2^* = P_4^* = P_6^* = H_6^* = A_6^* = 0 \tag{7.8}$$

The static force coefficients are given in Table 7.26 for the different cross sections. The results when including the static force coefficients are given in Table 7.27 and compared to the results obtained in Section 7.3.2 to 7.3.4. To save computational time the governing modes that contributed significantly to the stability limit has been included in the solutions. As can be seen from Figure 7.27 the change in critical velocity are insignificant. For all cross sections accept $BS30GV$, results shows a small increase in stability limit.

Table 7.26
Static load coefficients for cross sections from $Brusymfonien$ [11]. Coefficient C'_D is zero.

Section	Drag (C_D)	Lift (C_L)	Moment C_M	C'_L	C'_M
$BS15GV$	1.523	-0.145	0.134	5.46	0.04
$BS20GV$	1.754	0.118	0.185	6.37	-0.80
$BS30$	1.784	-0.218	0.222	5.31	-2.97
$BS30GV$	1.819	-0.200	0.194	6.96	-3.24

Table 7.27
Critical velocities and frequencies for cross sections from $Brusymfonien$. Results are shown when the quasi-steady coefficients are used, and compared to the solution without. QST: quasi-steady theory.

Section	Mode combination	Critical Velocity V_{CR} (m/s)		Critical frequency ω_{CR} (rad/s)	
		QST	Without QST	QST	Without QST
$BS15GV$	5,12,14	122.2	121.6	0.746	0.745
$BS20GV$	5,11,14	140.1	139.3	0.632	0.633
$BS30$	6,11,13	82.4	82.3	0.672	0.673
$BS30GV$	4,6,11,13,14	187.6	188.1	0.709	0.713

Chapter 8

Conclusion

The stability limit of a long-span suspension bridge crossing the Sognefjord has been assessed by using several cross sectional configurations, and by changing boundary conditions and backstay geometry. It is concluded that by changing the boundary conditions the stability limit changes insignificantly. This is because the vertical and torsional frequencies for the governing modes doesn't change significantly, compared to the horizontal modes where the frequencies are reduced by 3-8 % for the first three symmetric and asymmetric modes. Since the lateral deformations are not considered in this thesis, this effect is left for further investigations. On the other hand it is concluded that by changing the backstay/main span ratio from 0.1 to 0.2 the critical velocities are reduced with about 3.4-4.4 % depending on the projected height of the backstay cable. Two different technics are used for modelling the stiffening girder. One by lumping all the mass and specifying rotary inertia every 20 m, and the other by only lumping the additional mass. It is concluded that the two modelling technics are equivalent and provides the same stability limit.
The bridge has been tested with different cross sectional configurations for the stiffening girder, consisting of separate box-girders. One cross sectional configuration has shown a static instability phenomenon in torsion called static divergence when the angle of incidence of the wind flow is $\alpha = 0^o$. The stability limit has been found to be about 140 m/s. The same cross section gave a flutter stability limit of about 100 m/s when the angle of incidence is changed to $\alpha = 3^o$. The validity of this result is considered questionable since the values of the aerodynamic derivatives at 3^o are found in a turbulent wind flow where the buffeting forces are no longer negligible. When flutter occurs for this cross-section, several torsional modes together with one vertical mode contribute significantly to the stability limit. I.e. the instability is described as a multimode-coupled flutter phenomenon. It has been shown that the torsional mode that provides the largest shape-wise similarity and lowest frequency ratio together with the vertical mode does not necessarily provide the lowest flutter stability limit. It may be concluded that other factors contributes to the stability limit. It is suspected that the degree of coupling to the horizontal motion and the cables may influence the results to some extent.
A study has been carried out on several cross sectional configurations where the distances between the box-girders have been varied. The stability limit varied from about 80 m/s to over 180 m/s for a cross section with distance 30 m between the girders. It is concluded that the lack of guide vanes will reduce the stability significantly. It is also concluded that the critical velocity is higher when the distance between the box-girders is increased, because of improved aerodynamics All cross-sections show that the governing instability phenomenon is multimode flutter, but the degree of contribution from different modes

differs. The multimode phenomenon has shown to give both stabilizing and destabilizing effects. With a distance 15 m between the girders two vertical and one torsional mode contributes significant to the stability limit. Here, one vertical and one torsional mode showed a small degree of shape-wise similarity, and contributed as a stabilizing set of modes. For the remaining cross sections one vertical and one or more torsional modes contributed significantly to the stability limit. The shape-wise similarity indicates whether the multimodal effects are stabilizing or destabilizing. If one vertical mode shows the same magnitude of shape-wise similarity to two or more torsional modes, the multimode effect is most likely to give reduced critical velocity. One exception was shown for a cross section with 30 m between the girders with guide vanes. Here the opposite effect indicated that a vertical mode, shape-wise similar to two torsional modes by the same magnitude gave a stabilizing effect. The reliability of this result has been considered reduced since the reduced velocities are very high for this cross section.
The self-exited forces has been modelled using the aerodynamic derivatives obtain in wind tunnel tests. Since the wind tunnel tests are limited to vertical and rotational motion the derivatives associated with the horizontal motion has been disregarded. For some of the cross sections the static load coefficients have been obtained and the derivatives associated with the lateral motion have been replaced by the quasi-steady aerodynamic derivatives. Some of the results are recalculated using the static coefficients, and it is concluded that the results show no significant changes in the critical velocities.
The importance of the aerodynamic derivatives has also been assessed by scaling their values separately and recalculated the critical velocities for two cross sectional configurations. It is found that the most important aerodynamic derivatives are A_1^*, A_1^*, A_3^*, H_1^* and H_3^*. The critical velocities found for the different analysis has shown reduced velocities above those obtained from wind tunnel tests. The values for the derivatives have therefore been extrapolated, and the reliability of the results has been assessed. It has been found that it is crucial to represent the derivatives as accurately as possible. In the vicinity of the critical velocities the values for the derivatives has shown to give uncertain results. But it may be concluded that in the vicinity of the design critical velocity the derivatives render values of sufficient accuracy. By this it may be concluded that any instability due to strong wind are of no concern for this bridge when using the presented cross sections.
The solution routine for solving the complex eigenvalue problem, created by the author, has shown good results when few modes are included in the calculations. When several modes are included, the solution indicates numerical instabilities. I.e. the solution routine needs further modifications.
The critical flutter velocities have been found when using the different cross sectional configurations. The solutions have been found using the well-known flutter equations for a bimodal system with one vertical and one torsional mode. It is concluded that the shape-wise similarity and the frequency ratio are two important factors when assessing the flutter stability limit. A high shape-wise similarity combined with a low frequency ratio will provide the lowest critical velocity. The flutter solution has shown to provide critical velocities below those found with the multimode solution. It may be concluded that the flutter solution serves as an engineering approximation by providing conservative results for the cross sections tested herein.

Chapter 9

Further recommodations

In this thesis the aeroelastic stability limit due to strong wind has been assessed. Only the self-exited forces related to vertical and rotational motion has been used since aerodynamic derivatives associated with the lateral motion are not experimentally obtained for the cross-sectional configurations presented herein. As suspension bridges becomes longer the lateral deflections will increase, and the lateral contribution to the stability limit may be of importance. This can be investigated further by performing wind tunnel experiments where all three degree of freedoms is accounted for.

It has been shown in this thesis that an increase of the backstay/main span ratio will give reduced velocities. It would be interesting to see how other aeroelastic configurations may influence the stability limit. This may include different cable configurations, e.g. a mono cable with inclined hangers or several cables. The pylons have not been modelled in this thesis. The pylons probably have an influence on the natural frequencies and mode shapes, and this can be investigated further.

In this thesis all calculations were done in the frequency domain. It would be interesting to see if response calculations in the time domain would give the same critical velocities. Vortex shedding is a phenomenon that has not been discussed in this thesis. This phenomenon is important in the design process of suspension bridges, and may cause vibrations of unwanted magnitude, but they will not cause structural failure since they are self-destructive. In a serviceability state such oscillations may become too large and are unwanted. This phenomenon can therefore be investigated further for the actual bridge.

It was found that one cross-section gave static divergence. When the bimodal approach was used to asses the flutter velocity for this cross-section, it was found that the frequency onset of flutter increased as the shape-wise similarity decreased. If this has to do with the extrapolation of the aerodynamic derivatives or is caused by other factors, would be interesting to find out.

An attempt of solving the complex eigenvalue problem was carried out in this thesis. The solution routine provided result in agreement with the provided solution routine, especially when few modes were included in the calculation. When including several modes, the routine showed some numerical instability. Further investigation of these problems will improve the solution routine.

Appendix A

Calculations

A.1 Design wind speed

In order to calculate the structural loads due to wind, the statistical properties of the mean wind velocity are required. The mean wind velocity, $v_{m,10}$, is based on numerous meteorological observations recorded over several years, and averaged over a period of 10 min. In the European Standard [4] the mean wind velocity at an arbitrary distance above ground is given by the following equation;

$$v_{m,10}(z) = c_r(z) \cdot v_b \tag{A.1}$$

Here, v_b refers to a mean wind velocity at a distance $10m$ above ground and the definition is given as;

$$v_b = c_{dir} \cdot c_{season} \cdot c_{alt} \cdot c_{prob} \cdot v_{b,0} \tag{A.2}$$

Definition of the different symbols is as follows;

- c_{dir}: Direction factor. Can be chosen equal to 1.0 for all directions
- c_{alt}: Level factor. Can be set equal to 1.0
- c_{prob}: Probability factor used when a return period other than 50 years is used. Otherwise it can be set equal to 1.0
- c_{season}: Season factor. Can be set equal to 1.0
- $v_{b,0}$: Reference velocity dependent on location and geography. For the local government of Høyanger this value is equal to 26 m/s

With all factors equal to 1.0, v_b will be equal to the reference velocity. The roughness factor, $c_r(z)$, is given as;

$$c_r(z) = k_r \cdot ln\left(\frac{z_f}{z_0}\right) \tag{A.3}$$

Here, k_r is the terrain roughness factor, while z_0 is usually called the roughness length. The design wind velocity has in this thesis been calculated at a height of $z = 77\ m$ when assuming a sailing clearance of 75 m and a height of the bridge girder equal to 2 m. The following factors have been used;

- $z_0 = 0.01$
- $k_r = 0.17$

This gives a roughness factor equal to $c_r(z) = 1.52$, which leads to a value for the mean wind velocity at a height 77 m above ground as;

$$v_m(77) = 1.52 \cdot 26m/s = 39.6m/s \tag{A.4}$$

Multiplying the mean wind velocity with a safety factor of 1.6 [20], corresponding to a return period of 500 years, gives a critical design wind speed. From a stability analysis the lowest critical velocity must therefore be higher than;

$$V_{CR} > 1.6 \cdot v_m(77) = 63.3m/s \tag{A.5}$$

A.2 Geometry

The elevation of the girder is calculated by the use of a sector with a radius equal to the bridge-girder curvature, see figure below.

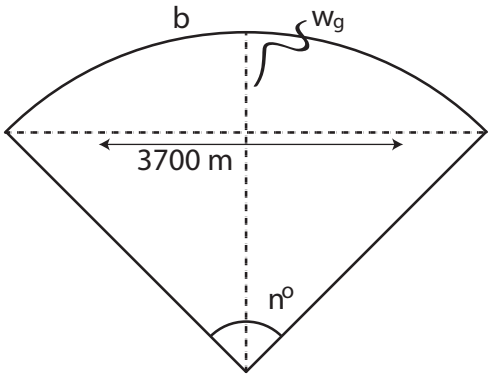

Figure A.1: Curvature of the bridge girder.

$$w_g = 56500 - \sqrt{56500^2 - (3700/2)^2} = 30.3m$$

The length of the curved girder can be found by calculatingthe length of the circular sector. The length of a circular sector is given by:

$$L = 2\pi R \frac{n^\circ}{360^\circ}$$

n° is the angle of the sector.

$$n^\circ = 2\arcsin(\frac{3700/2}{56500}) = 3.75278^\circ$$

$$b = 2\pi 56500 * \frac{3.75278^\circ}{360^\circ} = 3700.66m$$

A.3 Choice of stiffening girder dimensions

Free width of roadway according to $HB017$ [17];

Free width = 1 x 3 + 3 m = 6 m

For one driving lane this value is set to 6.5 m according to $HB185$ [20].

- Driving lane width

Driving lane width is based on an assumption that the Annual Daily Traffic volume is between 8000-12000 with speed limit 90 km/t.

$\Longrightarrow$ 3.75 m lane width

$\Longrightarrow$ Width of shoulders = (6.5-3.75)/2 = 1.38 m

- Walking and cycling path

$\Longrightarrow$ Width of minimum 3 m [17]

- Free space between bearing constructions and traffic profile should be at least 0.5 m [20].

Total width and height of each of each box-girder is then, when the height is given as 1/5 of the width B^*;

$\Longrightarrow B^*$ = 6.5 m + 3 m + 0.5 m = 10 m

$\Longrightarrow$ D = $B^*/5$ = 2 m

Width of air gap = $0.5 * B^*$ = 5 m, and the width B = 25 m.

A.4 Area of longitudinal stiffeners

Area of stiffener type A:
Upper width: $b_{Au} = 200mm$
Lower width: $b_{Al} = 400mm$
Thickness: $t = 6mm$
Hight of the trapeze: $h_A = 270mm$

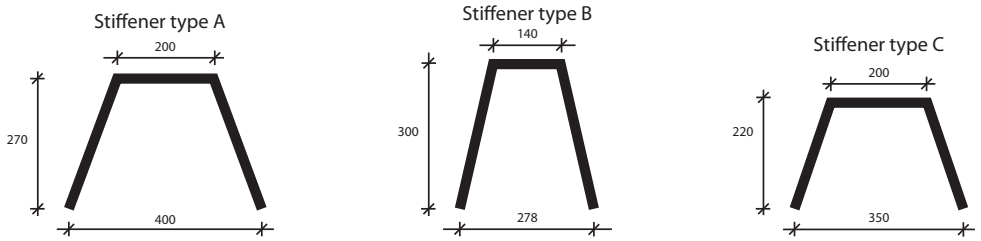

Figure A.2: Stiffeners used in the box-girders.

Length of the inclined plates:

$$l_{inc} = \sqrt{{h_A}^2 + (\frac{b_{Al} - b_{Au}}{2})^2} = \sqrt{270^2 + (\frac{400 - 200}{2})^2} = 287,9mm$$

$$A_A = t(2l_{inc} + b_{Au}) = 6(2 * 287,9 + 200) = 4655,1mm^2 = 0,00466m^2$$

Area of stiffener type B:
Upper width: $b_{Bu} = 140mm$
Lower width: $b_{Bl} = 278mm$
Thickness: $t = 6mm$
Hight of the trapeze: $h_B = 300mm$
Length of the inclined plates:

$$l_{inc} = \sqrt{{h_B}^2 + (\frac{b_{Bl} - b_{Bu}}{2})^2} = \sqrt{300^2 + (\frac{278 - 140}{2})^2} = 307,8mm$$

$$A_B = t(2l_{inc} + b_{Au}) = 6(2 * 287,9 + 140) = 4534mm^2 = 0,00453m^2$$

Area of stiffener type C:
Upper width: $b_{Cu} = 200mm$
Lower width: $b_{Cl} = 350mm$
Thickness: $t = 6mm$
Hight of the trapeze: $h_C = 220mm$
Length of the inclined plates:

$$l_{inc} = \sqrt{{h_C}^2 + (\frac{b_{Cl} - b_{Cu}}{2})^2} = \sqrt{220^2 + (\frac{350 - 200}{2})^2} = 232,4mm$$

$$A_C = t(2l_{inc} + b_{Cu}) = 6(2 * 232,4 + 200) = 3989,2mm^2 = 0,0040m^2$$

A.5 Mass moment of inertia

The mass moment of inertia of the box-girder is calculated about the cross sectional shear centre. The calculations are made by dividing the cross sections into minor parts, and summing up the contribution from each part. The calculations are based on the drawings made in CrossX (see Appendix B). From calculation in CrossX, origin is chosen at the left lower corner of the bottom plate. S marks the position of the shear centre. Mark that the coordinate system is calculated such that the Y-axis represents the strong axis, while the Z-axis represents the weak axis, see Figure A.3. As can bee seen from the tables below the mass moment of inertia of the stiffeners through its own N.A. is neglected. In the calculations different symbols has been used;

- l = Length of the part
- m = Mass of the part
- A= Area of part
- t = Thickness of part
- r = Distance from the part´s centre of gravity to the axis of rotation (shear centre)
- z = Horizontal distance from origin to the part´s centre of gravity
- y = Vertical distance from origin to the part´s centre of gravity
- z_{os} = Horizontal distance from origin to shear centre
- y_{os} = Vertical distance from origin to shear centre
- I = Mass moment of inertia of the part about the shear centre
- I_G = Mass moment of inertia of the part about it´s centre of gravity
- I_2 = Mass moment of inertia of the point mass m about the shear centre

$I = I_G + I_2 = \frac{1}{12}ml^2 + mr^2$

$r_2 = \sqrt{(z - z_{os})^2 + (y - y_{os})^2}$

From CrossX the following values for the shear centre were obtained;

- $z_{os} = 1078.0mm$
- $y_{os} = 4619.3mm$

Table A.1
Mass moment of inertia of steel girder.

z_os	4,6193 m
y_os	1,078 m
Material density	7850 kg/m^3

Longitudinal plates	**l [m]**	**t [m]**	**y' [m]**	**z' [m]**	**r [m]**	**A [m^2]**	**m [kg/m]**	**my [kgm/m]**	**mz [kgm/m]**	**I_G [kgm^2/m]**	**I_2 [kgm^2/m]**	**I [kgm^2/m]**
Plate 1	10	0,014	5,000	2,000	0,998	0,140	1099,0	5495,0	2198,0	9158	1094	10252
Plate 2	10	0,012	5,000	0,000	1,143	0,120	942,0	4710,0	0,0	7850	1231	9081
Plate 3	2	0,016	5,000	1,000	0,389	0,032	251,2	1256,0	251,2	84	38	122
Plate 4	2	0,016	10,000	1,000	5,381	0,032	251,2	2512,0	251,2	84	7274	7358
Plate 5	2,0000	0,016	0,000	1,000	4,620	0,032	251,2	0,0	251,2	84	5362	5445
Plate 6	1,4142	0,012	-0,500	1,750	5,163	0,017	133,2	-66,6	233,1	22	3551	3574
Plate 7	1,4142	0,012	-0,500	1,750	5,163	0,017	133,2	-66,6	233,1	22	3551	3574
Longitudinal stiffeners												
S_A1			0,925	0,169	3,804	0,005	36,5	33,8	6,2	0	529	529
S_A2			1,975	0,169	2,796	0,005	36,5	72,2	6,2	0	286	286
S_A3			3,025	0,169	1,835	0,005	36,5	110,5	6,2	0	123	123
S_A4			4,075	0,169	1,059	0,005	36,5	148,9	6,2	0	41	41
S_A5			5,925	0,169	1,591	0,005	36,5	216,5	6,2	0	92	92
S_A6			6,975	0,169	2,525	0,005	36,5	254,9	6,2	0	233	233
S_A7			8,025	0,169	3,525	0,005	36,5	293,3	6,2	0	454	454
S_A8			9,075	0,169	4,547	0,005	36,5	331,6	6,2	0	756	756
S_B1			0,505	1,823	4,181	0,005	35,6	18,0	64,9	0	622	622
S_B2			1,075	1,823	3,622	0,005	35,6	38,3	64,9	0	467	467
S_B3			1,645	1,823	3,066	0,005	35,6	58,5	64,9	0	335	335
S_B4			2,215	1,823	2,517	0,005	35,6	78,8	64,9	0	225	225
S_B5			2,785	1,823	1,980	0,005	35,6	99,1	64,9	0	139	139
S_B6			3,355	1,823	1,467	0,005	35,6	119,4	64,9	0	77	77
S_B7			3,925	1,823	1,018	0,005	35,6	139,7	64,9	0	37	37
S_B8			4,495	1,823	0,755	0,005	35,6	160,0	64,9	0	20	20
S_B9			5,505	1,823	1,157	0,005	35,6	195,9	64,9	0	48	48
S_B10			6,075	1,823	1,635	0,005	35,6	216,2	64,9	0	95	95
S_B11			6,645	1,823	2,158	0,005	35,6	236,5	64,9	0	166	166
S_B12			7,215	1,823	2,700	0,005	35,6	256,8	64,9	0	260	260
S_B13			7,785	1,823	3,252	0,005	35,6	277,1	64,9	0	376	376
S_B14			8,355	1,823	3,809	0,005	35,6	297,4	64,9	0	516	516
S_B15			8,925	1,823	4,370	0,005	35,6	317,7	64,9	0	680	680
S_B16			9,495	1,823	4,932	0,005	35,6	337,9	64,9	0	866	866
S_C1			-0,399	0,601	5,041	0,004	31,3	-12,5	18,8	0	796	796
S_C2			-0,399	1,399	5,029	0,004	31,3	-12,5	43,8	0	792	792
S_C3			0,142	1,375	4,487	0,004	31,3	4,5	43,1	0	630	630
S_C4			0,142	0,625	4,500	0,004	31,3	4,5	19,6	0	634	634
S_C5			5,142	1,375	0,601	0,004	31,3	161,0	43,1	0	11	11
S_C6			5,142	0,625	0,692	0,004	31,3	161,0	19,6	0	15	15
S_C7			9,858	1,375	5,247	0,004	31,3	308,7	43,1	0	862	862
S_C8			9,858	0,625	5,258	0,004	31,3	308,7	19,6	0	866	866
Sum:							4173,4	19072,2	4755,8			51454,9

Table A.2
Mass moment of inertia of additional elements.

Transverse Bulkheads	**l [m]**	**t [m]**	**y' [m]**	**z' [m]**	**r [m]**	**A [m^2]**	**m [kg/m]**	**my [kgm/m]**	**mz [kgm/m]**	**I_G [kgm^2/m]**	**I_2 [kgm^2/m]**	**I [kgm^2/m]**
Rectangular plate			5	1	0,389	20	471	2355	471	4082,0	71,1	4153,1
Triangle			-0,3333333	1	4,953	1	23,55	-7,85	23,55	436,1	577,8	1013,9
Sum:						21	494,55	2347,15	494,55			5167,0

Coating	**l [m]**	**t [m]**	**y' [m]**	**z' [m]**	**r [m]**	**A [m^2]**	**m [kg/m]**	**my [kgm/m]**	**mz [kgm/m]**	**I_G [kgm^2/m]**	**I_2 [kgm^2/m]**	**I [kgm^2/m]**
Asphalt traffic road	6,5		6,75	2,04	2,338		1325	8943,75	2703	4665,1	7241,6	11906,7
Asphalt pedestrian	3		2	2,02	2,784		306	612	618,12	229,5	2370,9	2600,4
Sum:							1631	9555,75	3321,12			14507,1

Railing	**l [m]**	**t [m]**	**y' [m]**	**z' [m]**	**r [m]**	**A [m^2]**	**m [kg/m]**	**my [kgm/m]**	**mz [kgm/m]**	**I_G [kgm^2/m]**	**I_2 [kgm^2/m]**	**I [kgm^2/m]**
Inner railing	1,2		6,75	2,6	2,618		51	344,25	132,6	0	349,7	349,7
Mid railing	1,2		3,5	2,6	1,889		51	178,5	132,6	0	182,0	182,0
Outher railing	1,2		0,5	2,6	4,391		51	25,5	132,6	0	983,5	983,5
Sum:							153	548,25	397,8			1515,3

Lower hanger attachment	**l [m]**	**t [m]**	**y' [m]**	**z' [m]**	**r [m]**	**A [m^2]**	**m [kg/m]**	**my [kgm/m]**	**mz [kgm/m]**	**I_G [kgm^2/m]**	**I_2 [kgm^2/m]**	**I [kgm^2/m]**
			0	2	4,710		43	0	86	0	954,1	954,1
Sum:							43	0	86		954,1	954,1

Table A.3
Calculation for stiffeners.

Stiffener	A	B	C
b_u [mm]	200	140	200
b_l [mm]	400	278	350
h [mm]	270	300	220
t [mm]	6	6	6
l_inc [mm]	287,9	307,8	232,4
A [mm^2]	4655,1	4534,0	3989,2
A [m^2]	0,0	0,0	0,0
Au [mm^2]	1200	840	1200
Ainc [mm^2]	1727,5	1847,0	1394,6
yu' [mm]	267	297	217
yinc' [mm]	135	150	110
zu' [mm]	0	0	0
zinc1 [mm]	150	104,5	137,5
zinc2 [mm]	150	104,5	137,5
y'_c [mm]	169,0	177,2	142,2
z'_c [mm]	0	0	0

z_os	4619,3 [mm]
y_os	1078 [mm]

Stiffener	z'_s	y'_s	z'_0	z'	y'	r
S_A1				169,0	925,0	3804,5
S_A2				169,0	1975,0	2796,2
S_A3				169,0	3025,0	1835,2
S_A4				169,0	4075,0	1059,5
S_A5				169,0	5925,0	1590,9
S_A6				169,0	6975,0	2525,0
S_A7				169,0	8025,0	3524,9
S_A8				169,0	9075,0	4547,5
S_B1				1822,8	505,0	4181,2
S_B2				1822,8	1075,0	3621,7
S_B3				1822,8	1645,0	3066,1
S_B4				1822,8	2215,0	2517,0
S_B5				1822,8	2785,0	1979,7
S_B6				1822,8	3355,0	1467,4
S_B7				1822,8	3925,0	1018,2
S_B8				1822,8	4495,0	755,1
S_B9				1822,8	5505,0	1157,2
S_B10				1822,8	6075,0	1635,2
S_B11				1822,8	6645,0	2158,3
S_B12				1822,8	7215,0	2700,4
S_B13				1822,8	7785,0	3252,1
S_B14				1822,8	8355,0	3809,2
S_B15				1822,8	8925,0	4369,6
S_B16				1822,8	9495,0	4932,3
S_C1	100,541362	100,541362	500	600,5	-399,5	5041,4
S_C2	100,541362	100,541362	1500	1399,5	-399,5	5029,0
S_C3				1375,0	142,2	4487,0
S_C4				625,0	142,2	4500,0
S_C5				1375,0	5142,2	601,3
S_C6				625,0	5142,2	691,8
S_C7				1375,0	9857,8	5246,9
S_C8				625,0	9857,8	5258,1

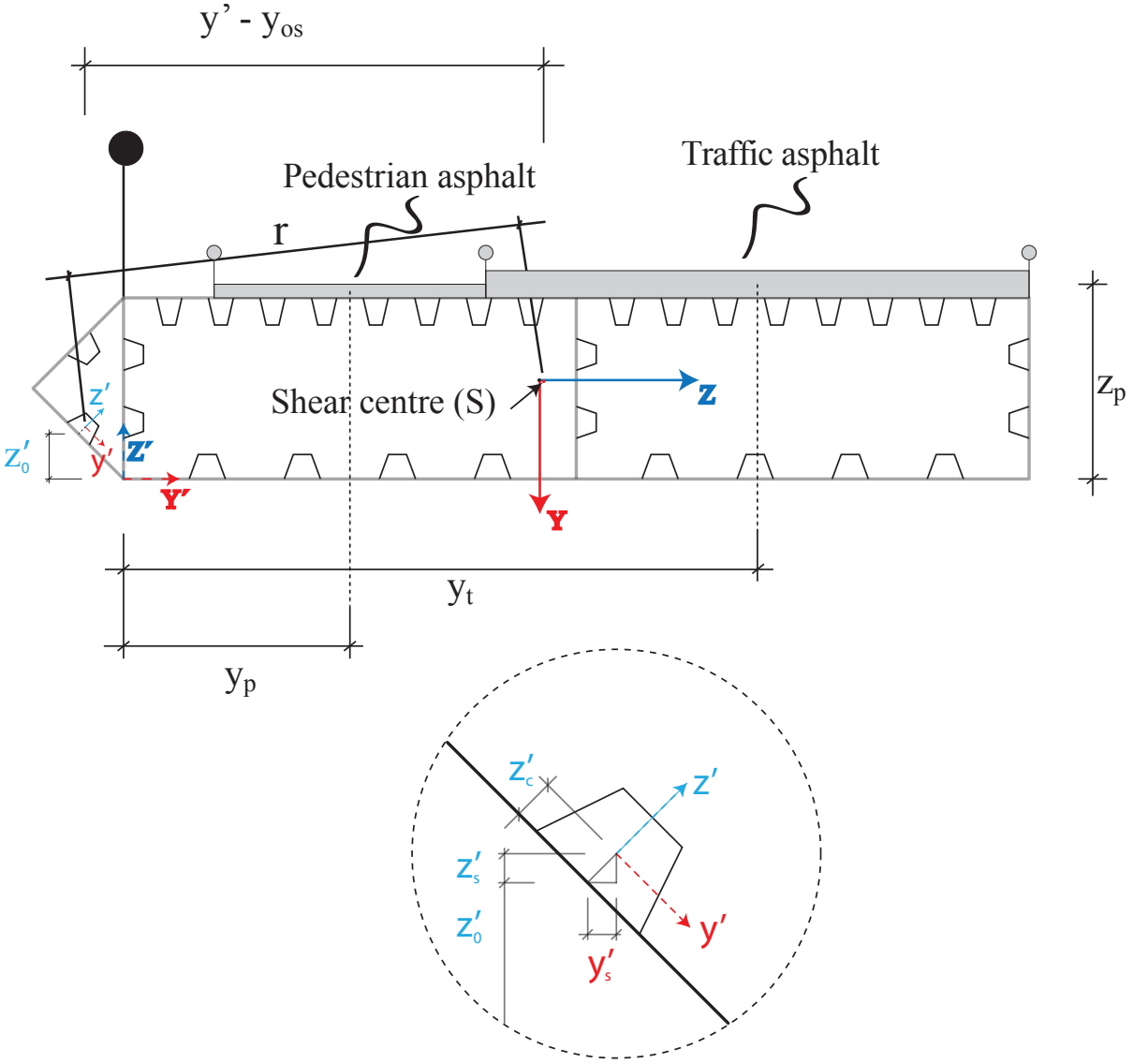

Figure A.3: Overview of dimensions when calculating the mass moment of inertia.

A.6 Eigenvalue problem

To solve the eigenvalue problem presented in Section 4.4 on page 32, it's necessary to solve Equation 4.40. Starting from Equation 4.38 given as;

$$\ddot{\boldsymbol{\eta}} + \tilde{\boldsymbol{M}}_0^{-1}(\tilde{\boldsymbol{C}}_0 - \tilde{\boldsymbol{C}}_{ae})\dot{\boldsymbol{\eta}} + \tilde{\boldsymbol{M}}_0^{-1}(\tilde{\boldsymbol{K}}_0 - \tilde{\boldsymbol{K}}_{ae}) \cdot \boldsymbol{\eta} = 0 \tag{A.6}$$

and introducing the vector $\boldsymbol{\psi} = [\dot{\boldsymbol{\eta}}^T \quad \boldsymbol{\eta}^T]^T$ and $\dot{\boldsymbol{\psi}} = [\ddot{\boldsymbol{\eta}}^T \quad \dot{\boldsymbol{\eta}}^T]^T$, gives the following equation;

$$\begin{aligned} \dot{\boldsymbol{\psi}} = \begin{Bmatrix} \ddot{\boldsymbol{\eta}}^T \\ \dot{\boldsymbol{\eta}}^T \end{Bmatrix} &= \begin{bmatrix} -\tilde{\boldsymbol{M}}_0^{-1}(\tilde{\boldsymbol{C}}_0 - \tilde{\boldsymbol{C}}_{ae}) & -\tilde{\boldsymbol{M}}_0^{-1}(\tilde{\boldsymbol{K}}_0 - \tilde{\boldsymbol{K}}_{ae}) \\ \boldsymbol{I} & \boldsymbol{0} \end{bmatrix} \begin{Bmatrix} \dot{\boldsymbol{\eta}}^T \\ \boldsymbol{\eta}^T \end{Bmatrix} \\ \implies \quad \dot{\boldsymbol{\psi}} &= \boldsymbol{A}\boldsymbol{\psi} \end{aligned} \tag{A.7}$$

Introducing the characteristic solution $\boldsymbol{\eta} = \hat{\boldsymbol{\eta}} e^{\lambda_n t}$ and its first and second derivatives; $\dot{\boldsymbol{\eta}} = \lambda_n \hat{\boldsymbol{\eta}} e^{\lambda_n t}$ and $\ddot{\boldsymbol{\eta}} = \lambda_n^2 \hat{\boldsymbol{\eta}} e^{\lambda_n t}$, which gives the following relations;

$$\boldsymbol{\psi} = \begin{Bmatrix} \lambda_n \hat{\boldsymbol{\eta}} \\ \hat{\boldsymbol{\eta}} \end{Bmatrix} e^{\lambda_n t} = \hat{\boldsymbol{\psi}} e^{\lambda_n t}; \quad \dot{\boldsymbol{\psi}} = \begin{Bmatrix} \lambda_n^2 \hat{\boldsymbol{\eta}} \\ \lambda_n \hat{\boldsymbol{\eta}} \end{Bmatrix} e^{\lambda_n t} = \lambda_n \hat{\boldsymbol{\psi}} e^{\lambda_n t} \tag{A.8}$$

Introducing these relations into Equation A.7 gives the following equation;

$$\hat{\boldsymbol{\psi}} \lambda_n e^{\lambda_n t} = \boldsymbol{A} \hat{\boldsymbol{\psi}} e^{\lambda_n t} \tag{A.9}$$

Then the final eigenvalue problem can be written as;

$$\hat{\boldsymbol{\psi}}(\boldsymbol{A} - \lambda \boldsymbol{I}) = \boldsymbol{0} \tag{A.10}$$

A.7 Effective mass

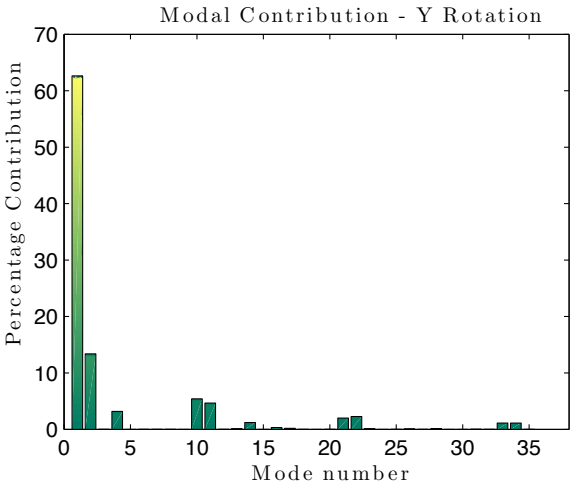

Figure A.4: Modal effective mass for rotation about the vertical axis. The percentage modal effective mass contribution of each mode to the total effective mass for rotation about the vertical y-axis is shown. The modes with the highest peaks are identified as horizontal, torsional or a coupling motion between them.

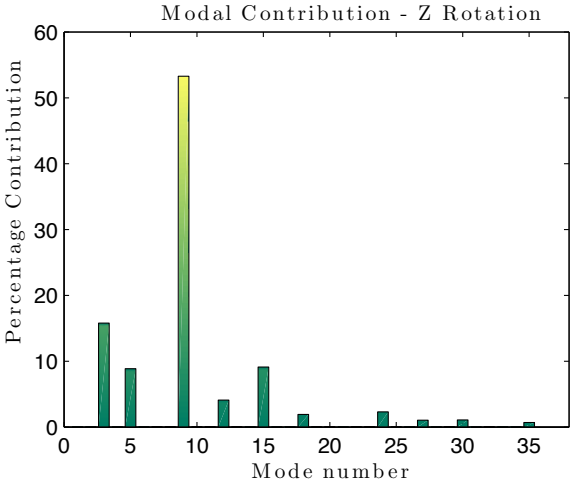

Figure A.5: Modal effective mass for rotation about the lateral axis. The percentage modal effective mass contribution of each mode to the total effective mass for rotation about the lateral z-axis is shown. The modes with the highest peaks are identified as vertical modes. The modes with highest peaks are identified as both symmetric and asymmetric modes. The six first peaks are the modes in class 2 presented in Section 6.2.1.

Appendix B

Elements modelled in CrossX

B.1 Box-Girder

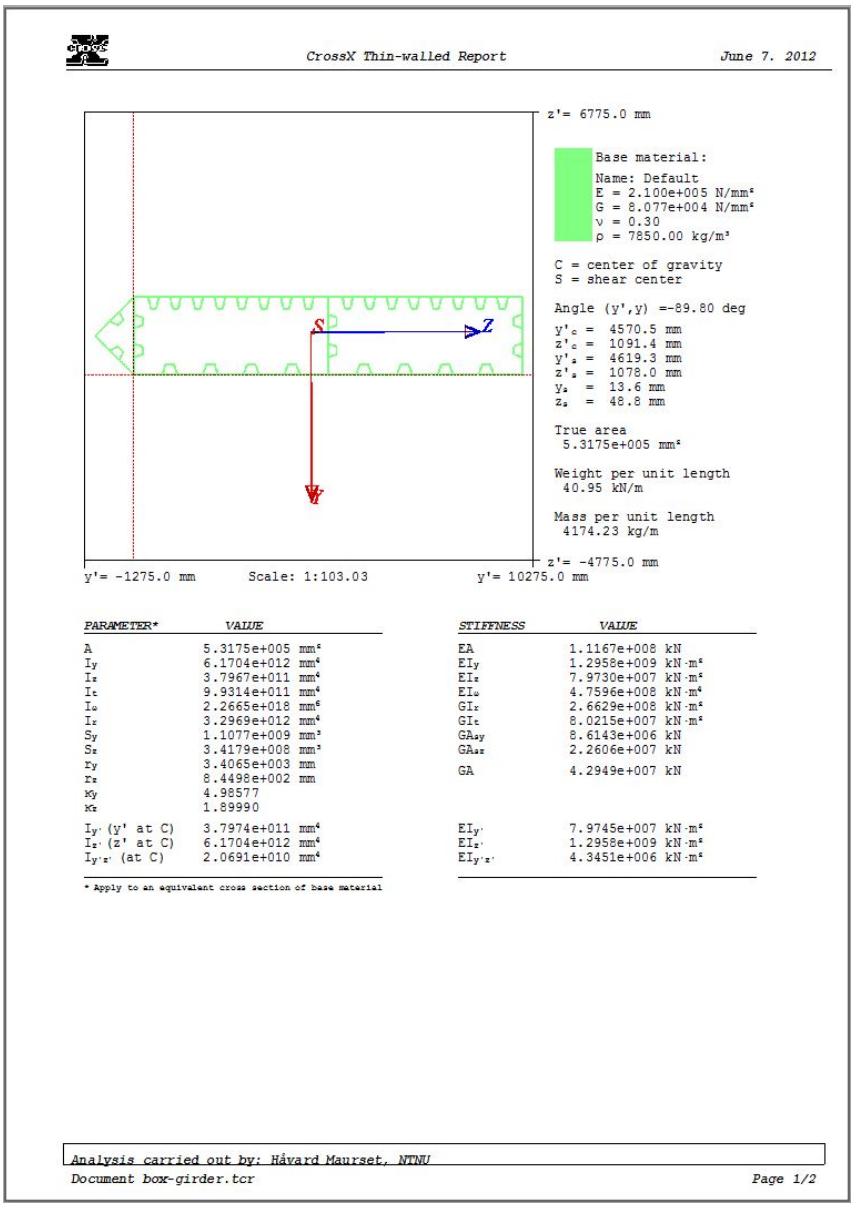

CrossX Thin-walled Report — June 7. 2012

z'= 6775.0 mm

Base material:
Name: Default
E = 2.100e+005 N/mm²
G = 8.077e+004 N/mm²
ν = 0.30
ρ = 7850.00 kg/m³

C = center of gravity
S = shear center

Angle (y',y) =-89.80 deg

y'c = 4570.5 mm
z'c = 1091.4 mm
y's = 4619.3 mm
z's = 1078.0 mm
ys = 13.6 mm
zs = 48.8 mm

True area
5.3175e+005 mm²

Weight per unit length
40.95 kN/m

Mass per unit length
4174.23 kg/m

y'= -1275.0 mm Scale: 1:103.03 y'= 10275.0 mm

z'= -4775.0 mm

PARAMETER*	VALUE	
A	5.3175e+005	mm²
Iy	6.1704e+012	mm⁴
Iz	3.7967e+011	mm⁴
It	9.9314e+011	mm⁴
Iω	2.2665e+018	mm⁶
Ir	3.2969e+012	mm⁴
Sy	1.1077e+009	mm³
Sz	3.4179e+008	mm³
ry	3.4065e+003	mm
rz	8.4498e+002	mm
Ky	4.98577	
Kz	1.89990	
Iy' (y' at C)	3.7974e+011	mm⁴
Iz' (z' at C)	6.1704e+012	mm⁴
Iy'z' (at C)	2.0691e+010	mm⁴

* Apply to an equivalent cross section of base material

STIFFNESS	VALUE	
EA	1.1167e+008	kN
EIy	1.2958e+009	kN·m²
EIz	7.9730e+007	kN·m²
EIω	4.7596e+008	kN·m⁴
GIr	2.6629e+008	kN·m²
GIt	8.0215e+007	kN·m²
GAsy	8.6143e+006	kN
GAsz	2.2606e+007	kN
GA	4.2949e+007	kN
EIy'	7.9745e+007	kN·m²
EIz'	1.2958e+009	kN·m²
EIy'z'	4.3451e+006	kN·m²

Analysis carried out by: Håvard Maurset, NTNU

Document box-girder.tcr Page 1/2

Figure B.1: Box-girder modelled in *CrossX*.

B.2 Cross beam

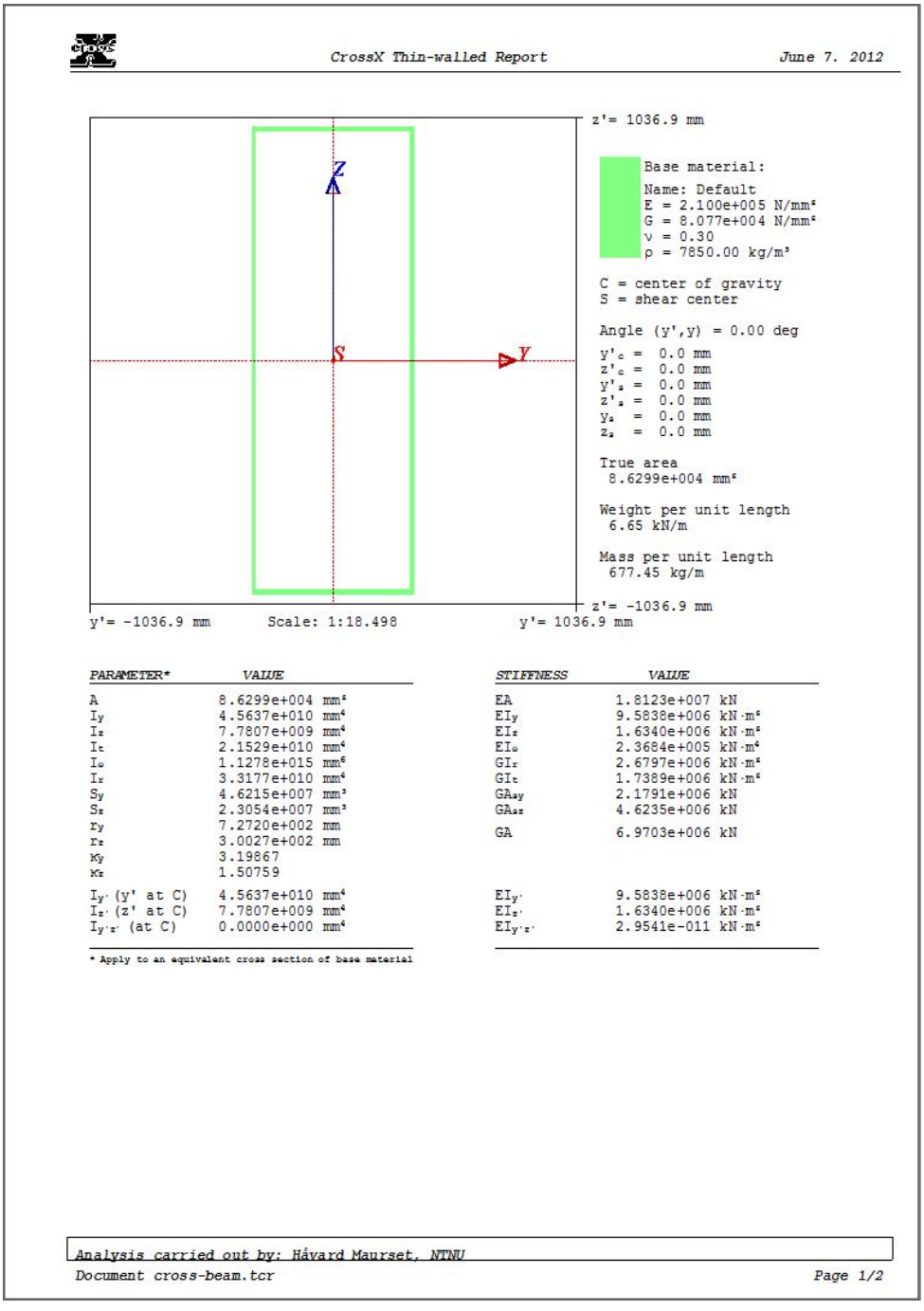

CrossX Thin-walled Report June 7. 2012

z'= 1036.9 mm

Base material:
Name: Default
E = 2.100e+005 N/mm²
G = 8.077e+004 N/mm²
ν = 0.30
ρ = 7850.00 kg/m³

C = center of gravity
S = shear center

Angle (y',y) = 0.00 deg

y'_c = 0.0 mm
z'_c = 0.0 mm
y'_s = 0.0 mm
z'_s = 0.0 mm
y_s = 0.0 mm
z_s = 0.0 mm

True area
8.6299e+004 mm²

Weight per unit length
6.65 kN/m

Mass per unit length
677.45 kg/m

z'= -1036.9 mm

y'= -1036.9 mm Scale: 1:18.498 y'= 1036.9 mm

PARAMETER*	VALUE	
A	8.6299e+004	mm²
I_y	4.5637e+010	mm⁴
I_z	7.7807e+009	mm⁴
I_t	2.1529e+010	mm⁴
I_ω	1.1278e+015	mm⁶
I_x	3.3177e+010	mm⁴
S_y	4.6215e+007	mm³
S_z	2.3054e+007	mm³
r_y	7.2720e+002	mm
r_z	3.0027e+002	mm
k_y	3.19867	
k_z	1.50759	
$I_{y'}$ (y' at C)	4.5637e+010	mm⁴
$I_{z'}$ (z' at C)	7.7807e+009	mm⁴
$I_{y'z'}$ (at C)	0.0000e+000	mm⁴

* Apply to an equivalent cross section of base material

STIFFNESS	VALUE	
EA	1.8123e+007	kN
EI_y	9.5838e+006	kN·m²
EI_z	1.6340e+006	kN·m²
EI_ω	2.3684e+005	kN·m⁴
GI_x	2.6797e+006	kN·m²
GI_t	1.7389e+006	kN·m²
GA_{sy}	2.1791e+006	kN
GA_{sz}	4.6235e+006	kN
GA	6.9703e+006	kN
$EI_{y'}$	9.5838e+006	kN·m²
$EI_{z'}$	1.6340e+006	kN·m²
$EI_{y'z'}$	2.9541e-011	kN·m²

Analysis carried out by: Håvard Maurset, NTNU

Document cross-beam.tcr Page 1/2

Figure B.2: Crossbeam modelled in *CrossX*.

Appendix C

Aerodynamic derivatives

C.1 Section 2TFGP

Table C.1
Aerodynamic derivatives: Experimental results obtained for Cross section 2TFGP with $25m$ between the two box girders. Angle of incidence 0^o. The width of one girder is in this thesis referred to as B^*.

$V/(nB^*)$	Derivatives 0^o							
	H_1^*	H_2^*	H_3^*	H_4^*	A_1^*	A_2^*	A_3^*	A_4^*
0	0	0	0	0	0.0	0.0	0.0	0.0
1.8	-0.9	-2.3	-1.7	-0.5	-0.1	-0.3	-0.8	0.0
3.1	-2.1	-5.5	-3.3	0	0.4	-1.5	-0.8	0.3
4.4	-2.6	-6.9	-8.3	0.3	1.0	-2.8	0.0	0.3
5.7	-3.0	-9.7	-10.0	0.7	1.5	-3.7	1.6	0.3
7.2	-3.3	-13.8	-12.5	0.9	2.3	-4.6	3.9	0.4
8.8	-3.5	-18.0	-13.3	1.1	2.5	-6.1	7.0	0.4
10.1	-3.7	-19.4	-14.2	1.2	2.8	-7.7	11.6	0.4
11.4	-3.9	-25.4	-16.7	1.1	3.5	-9.2	15.5	0.4
14.5	-4.4	-30.0	-20.8	1.5	4.4	-13.2	26.4	0.4
17.6	-4.7	-41.5	-25.0	1.3	5.4	-17.5	36.5	0.3
20.3	-5.3	-53.0	-33.3	1.3	6.3	-23.0	46.6	0.3
23.1	-6.1	-62.3	-50.0	1.6	7.5	-29.1	65.9	0.4
26.2	-7.4	-71.5	-66.7	1.4	8.2	-36.8	89.2	0.4
29.0	-7.9	-83.0	-83.3	1.3	8.9	-46.0	112.5	0.4
$\mathbf{c_2}$	0	0	-0.0771	-0.0030	0.0011	-0.0437	0.1495	0
$\mathbf{c_1}$	-0.2890	-2.5765	-0.4587	0.1339	0.2830	-0.2784	-0.5250	0.0188
$\mathbf{c_0}$	0	0	0	0	0	0	0	0

Polynimial fit:

$P(V_{red}) = c_2 V_{red}^2 + c_1 V_{red} + c_0 \qquad V_{red} = V/(nB^*)$

Table C.2
Aerodynamic derivatives: Experimental results obtained for Cross section 2TFGP with $25m$ between the two box girders. Angle of incidence 3^o. The width of one girder is in this thesis referred to as B^*.

$V/(nB^*)$	Derivatives 3^o							
	H_1^*	H_2^*	H_3^*	H_4^*	A_1^*	A_2^*	A_3^*	A_4^*
0	0,0	0,0	0,0	0,0	0,0	0,0	0,0	0,0
1,8	-0,9	-2,3	1,7	-0,7	-0,1	-0,3	-2,3	0,0
3,1	-3,5	0,0	5,0	-0,5	0,4	-1,5	-2,3	0,5
4,4	-4,4	2,3	8,3	0,8	1,0	-2,8	-1,6	0,8
5,7	-4,4	3,7	10,0	1,3	1,3	-3,7	-0,8	0,9
7,2	-4,6	4,6	13,3	1,4	1,9	-4,3	0,0	1,1
8,8	-5,6	3,7	16,7	1,1	2,8	-5,8	3,9	1,1
10,1	-5,6	2,3	21,7	0,9	2,8	-6,4	7,8	1,0
11,4	-6,1	4,2	25,0	0,5	4,0	-7,7	9,3	1,2
14,5	-7,9	4,6	41,7	0,0	5,2	-10,7	17,1	1,2
17,6	-9,6	4,6	58,3	0,6	5,9	-12,3	25,6	0,5
20,3	-11,4	4,2	73,3	0,0	7,0	-14,1	38,8	0,5
23,1	-13,1	6,9	93,3	0,9	8,2	-16,9	48,1	0,8
26,2	-15,8	4,6	116,7	2,2	9,5	-19,9	64,4	2,1
29,0	-17,5	2,3	150,0	1,3	11,0	-23,0	83,8	1,6
$\mathbf{c_2}$	0	0	0.1526	-0.0007	0.0040	-0.0071	0.1204	0
$\mathbf{c_1}$	-0.5858	0.2174	0.5944	0.0652	0.2641	-0.5780	-0.6353	0.0611
$\mathbf{c_0}$	0	0	0	0	0	0	0	0

Polynimial fit:

$P(V_{red}) = c_2 V_{red}^2 + c_1 V_{red} + c_0 \qquad V_{red} = V/(nB^*)$

C.2 Section BS30

Table C.3
Cross section BS30 with $30m$ between the two box girders [11]. Angle of incidence 0^o. The frequency ratio between the vertical and torsional motion was 1.4 during the experiments. Guide vanes were not included. The width of one girder is in this thesis referred to as B^*.

$V/(n_z B^*)$	$V/(\omega_z B^*)$	$V/(n_\theta B^*)$	$V/(\omega_\theta B^*)$	H_1^*	H_2^*	H_3^*	H_4^*	A_1^*	A_2^*	A_3^*	A_4^*
11.43	1.82	8.26	1.31	-26.26	7.39	27.56	-16.73	-5.64	-19.14	-8.34	-9.81
20.51	3.26	14.36	2.29	-27.01	7.23	51.36	5,01	8.97	-48.59	1.48	17.93
27.45	4.37	19.79	3.15	-20.21	3.24	73.19	-14.40	-14.70	-62.70	5.71	13.78
36.20	5.76	2489	3.96	-25.12	33.99	114.31	3.91	2.93	-73.57	-36.51	6.79
42.31	6.73	29.82	4.75	-31.99	32.45	172.37	-18.72	-0.31	-34.36	-61.36	-2.14
48.69	7.75	35.12	5.59	-45.90	19.57	179.89	-32.67	13.37	-77.52	-37.66	13.13
58.48	9.31	38.92	6.19	-42.48	55.36	255.77	8.19	7.20	-57.33	-91.59	24.10
63.60	10.12	43.17	6.87	-57.80	36.00	317.34	-34.36	17.01	-61.86	-130.53	18.94
			$\mathbf{c_2}$	-0.0008	-0.0028	0.0821	-0.0263	0.0152	0.0690	-0.0555	-0.0148
			$\mathbf{c_1}$	-0.7569	0.9665	2.6497	0.6965	-0.5853	-4.1702	0.2825	0.7755
			$\mathbf{c_0}$	-2.0256	-2.3074	-1.9305	-0.7328	1.9937	-1.7069	3.6506	1.9764

Polynimial fit:

$P(V_{red}) = c_2 V_{red}^2 + c_1 V_{red} + c_0 \qquad V_{red} = V/(nB^*)$

C.3 Section BS30GV

Table C.4
Cross section BS30GV with $30m$ between the two box girders [11]. Angle of incidence 0^o. The frequency ration between the vertical and torsional motion was 1.3 during the experiments. Guide vanes were included. The width of one girder is in this thesis referred to as B^*.

$V/(n_z B^*)$	$V/(\omega_z B^*)$	$V/(n_\theta B^*)$	$V/(\omega_\theta B^*)$	H_1^*	H_2^*	H_3^*	H_4^*	A_1^*	A_2^*	A_3^*	A_4^*
17.61	2.80	13.91	2.21	-28.99	11.79	72.02	8.04	-15.28	-33.57	-5.34	6.41
33.02	5.26	24.66	3.92	-44.62	11.69	15.03	22.56	7.28	-44.43	-24.62	15.14
45.05	7.17	32.49	5.17	-61.19	49.14	263.46	5.20	18.04	-17.20	-119.27	25.60
55.63	8.85	40.42	6.43	-74.55	10.58	353.02	-23.34	12.15	-51.44	-79.37	46.54
65.12	10.36	47.57	7.57	-63.40	84.68	460.77	-30.95	16.27	-91.31	-207.26	9.54
80.49	12.81	56.42	8.98	-61.44	119.22	537.97	-36.38	17.88	-69.93	-184.31	34.70
90.01	14.33	61.89	9.85	-8.97	148.06	647.03	-47.58	25.17	-83.66	-236.88	34.50
99.74	15.87	65.13	10.37	-98.14	188.41	768.39	-52.37	23.72	-182.19	-359.06	23.93
105.30	16.76	74.57	11.87	-117.17	58.70	1023.70	-61.89	21.28	-255.54	-269.55	8.96
			$\mathbf{c_2}$	0.0056	0.0635	0.1096	-0.0081	-0.0005	-0.0343	-0.0749	-0.0054
			$\mathbf{c_1}$	-1.3998	-1.4858	4.0865	0.1358	0.2937	0.2520	0.1815	0.8218
			$\mathbf{c_0}$	-3.0938	3.9778	-0.6063	7.2128	0.1443	-5.8488	-1.3881	-0.8680

Polynimial fit:

$P(V_{red}) = c_2 V_{red}^2 + c_1 V_{red} + c_0 \qquad V_{red} = V/(nB^*)$

C.4 Section BS20GV

Table C.5
Cross section BS20GV with $20m$ between the two box girders [11]. Angle of incidence 0^o. The frequency ration between the vertical and torsional motion was 1.3 during the experiments. Guide vanes were included. The width of one girder is in this thesis referred to as B^*.

$V/(n_z B^*)$	$V/(\omega_z B^*)$	$V/(n_\theta B^*)$	$V/(\omega_\theta B^*)$	H_1^*	H_2^*	H_3^*	H_4^*	A_1^*	A_2^*	A_3^*	A_4^*
16.56	2.64	12.41	1.98	-16.34	22.24	43.98	-4.71	-5.30	-22.35	-26.52	2.86
29.44	4.69	21.81	3.47	-18.88	33.25	92.37	-3.10	-1.39	-26.07	-34.87	3.97
40.30	6.41	30.84	4.91	-28.05	21.44	171.60	-28.15	-4.21	-25.84	-26.73	9.88
50.11	7.98	38.6	6.14	-41.14	56.52	210.68	-31.37	1.49	-47.89	-45.89	1.28
61.02	9.71	46.59	7.42	-65.46	35.05	403.16	-43.58	5.57	-46.33	-32.52	10.59
72.01	11.46	53.96	8.59	-52.47	201.51	447.87	-34.25	2.69	-138.31	-80.83	0.78
79.60	12.67	62.61	9.96	-78.10	76.32	798.82	-40.75	-2.90	-156.30	-49.76	-0.52
87.58	13.94	73.97	11.77	-80.99	40.13	816.83	-51.29	-5.45	-158.52	-33.74	-3.75
101.98	16.23	84.17	13.40	-83.54	120.71	940.17	-58.25	-2.34	-112.58	48.01	3.16
			$\mathbf{c_2}$	0.0003	-0.0128	0.0896	0.0004	-0.0010	0.0030	0.0392	-0.0020
			$\mathbf{c_1}$	-0.9396	2.3909	4.8589	-0.6300	0.0861	-2.2708	-3.2142	0.1722
			$\mathbf{c_0}$	3.5081	-9.8447	-35.0403	2.5589	-1.3091	16.8237	12.1639	1.1391

Polynimial fit:

$P(V_{red}) = c_2 V_{red}^2 + c_1 V_{red} + c_0 \qquad V_{red} = V/(nB^*)$

C.5 Section BS15GV

Table C.6
Cross section BS15GV with $15m$ between the two box girders [11]. Angle of incidence 0^o. The frequency ration between the vertical and torsional motion was 1.3 during the experiments. Guide vanes were included. The width of one girder is in this thesis referred to as B^*.

$V/(n_z B^*)$	$V/(\omega_z B^*)$	$V/(n_\theta B^*)$	$V/(\omega_\theta B^*)$	H_1^*	H_2^*	H_3^*	H_4^*	A_1^*	A_2^*	A_3^*	A_4^*
18.07	2.88	13.54	2.15	-20.17	5.70	46.04	1.04	-2.11	-4.37	-6.30	0.71
31.00	4.93	22.85	3.64	-16.06	17.47	108.05	10.79	-0.58	-3.88	-12.34	-3.99
40.52	6.45	30.62	4.87	-14.73	96.46	159.19	-18.25	-2.21	-18.21	-13.73	5.37
51.07	8.13	39.72	6.32	-35.20	51.44	231.56	-24.16	-9.70	-31.38	2.70	1.17
63.16	10.05	49.04	7.80	-36.38	60.80	414.43	-12.92	-7.97	-29.03	17.94	0.08
			$\mathbf{c_2}$	-0.0043	-0.0344	0.1638	-0.0039	-0.0028	-0.0074	0.0385	-0.0002
			$\mathbf{c_1}$	-0.3443	3.0294	0.0040	-0.1118	0.0208	-0.3430	-1.5172	0.0392
			$\mathbf{c_0}$	0.1591	-3.4781	4.2271	2.3987	0.3247	1.3018	0.1633	-0.5460

Polynimial fit:

$P(V_{red}) = c_2 V_{red}^2 + c_1 V_{red} + c_0 \qquad V_{red} = V/(nB^*)$

Appendix D

Mode shapes

This chapter shows the mode shapes from the different classes presented from *Analysis* 1. The first 5 vertical and torsional modes for sections used in the stability analysis and the comparative analysis are also shown. The torsional and horizontal modes may show amplitudes less then 1 because of coupling.

D.1 Horizontal modes from *Analysis* 1

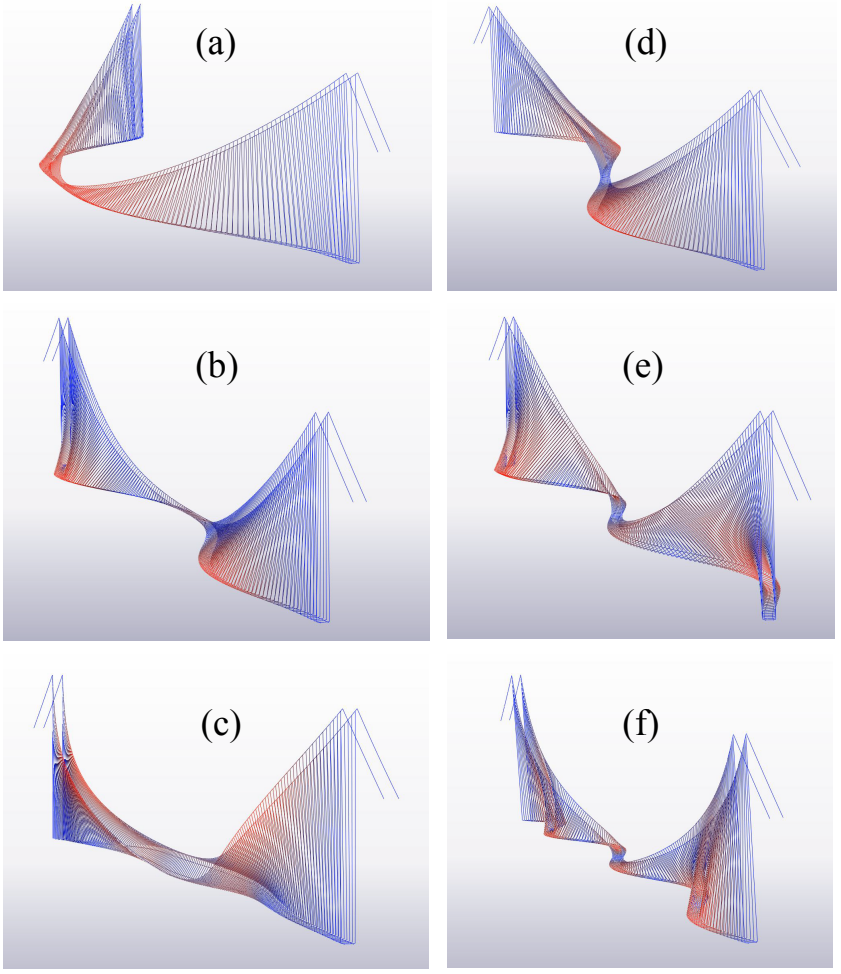

Figure D.1: Horizontal symmetric and asymmetric modes: (a) 1stHS(1) (b) 2ndHS(4) (c) 3rdHS(11) (d) 1stHA(2) (e) 2ndHA(6) (f) 3rdHA(17). Red color indicates large amplitudes.

D.2 Vertical modes from *Analysis* 1

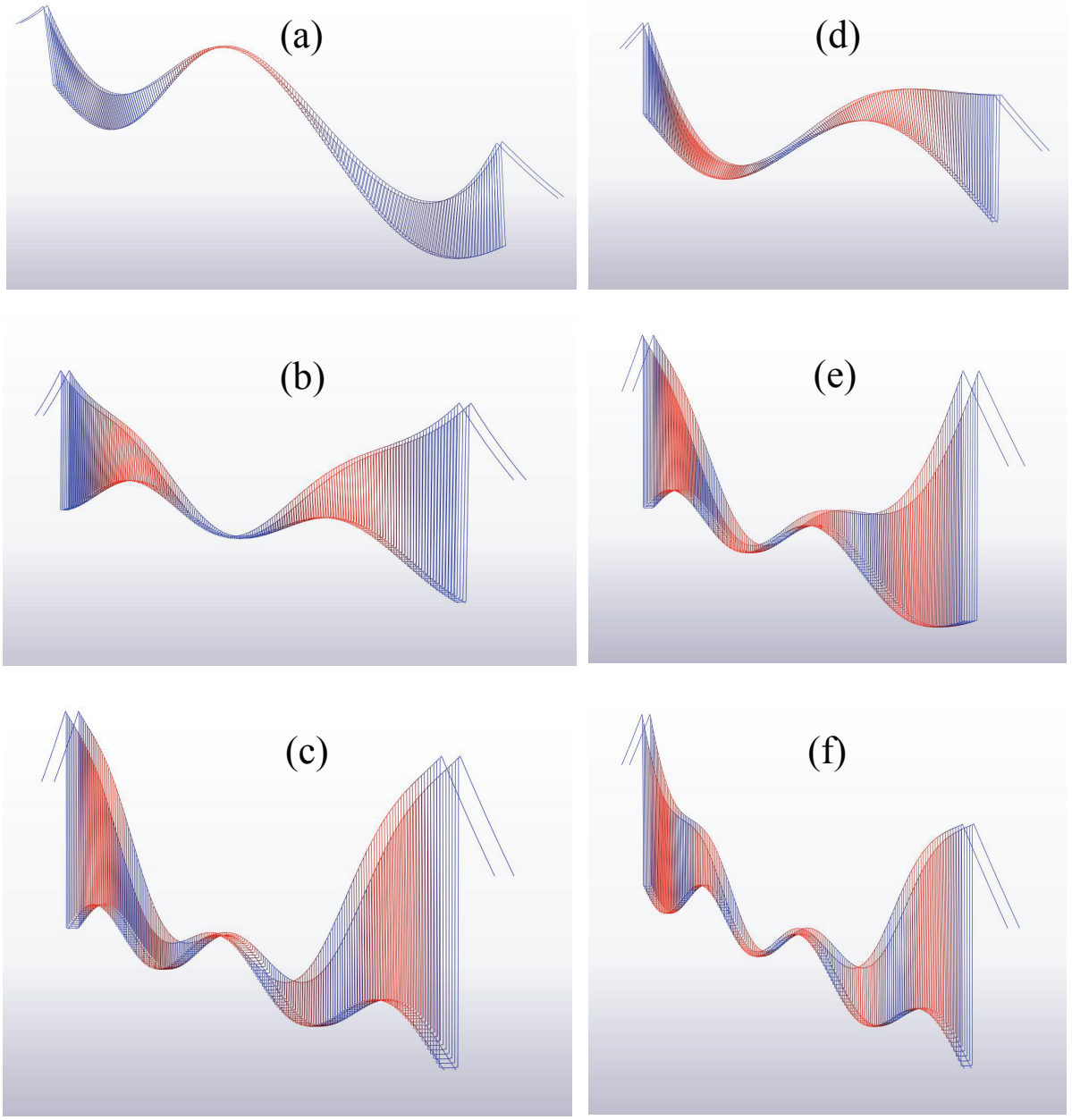

Figure D.2: Vertical symmetric and asymmetric modes: (a) 1stVS(5) (b) 2ndVS(9) (c) 3rdVS(15) (d) 1stVA(3) (e) 2ndVA(12) (f) 3rdVA(18). Red color indicates large amplitudes.

D.3 Torsional modes from *Analysis* 1

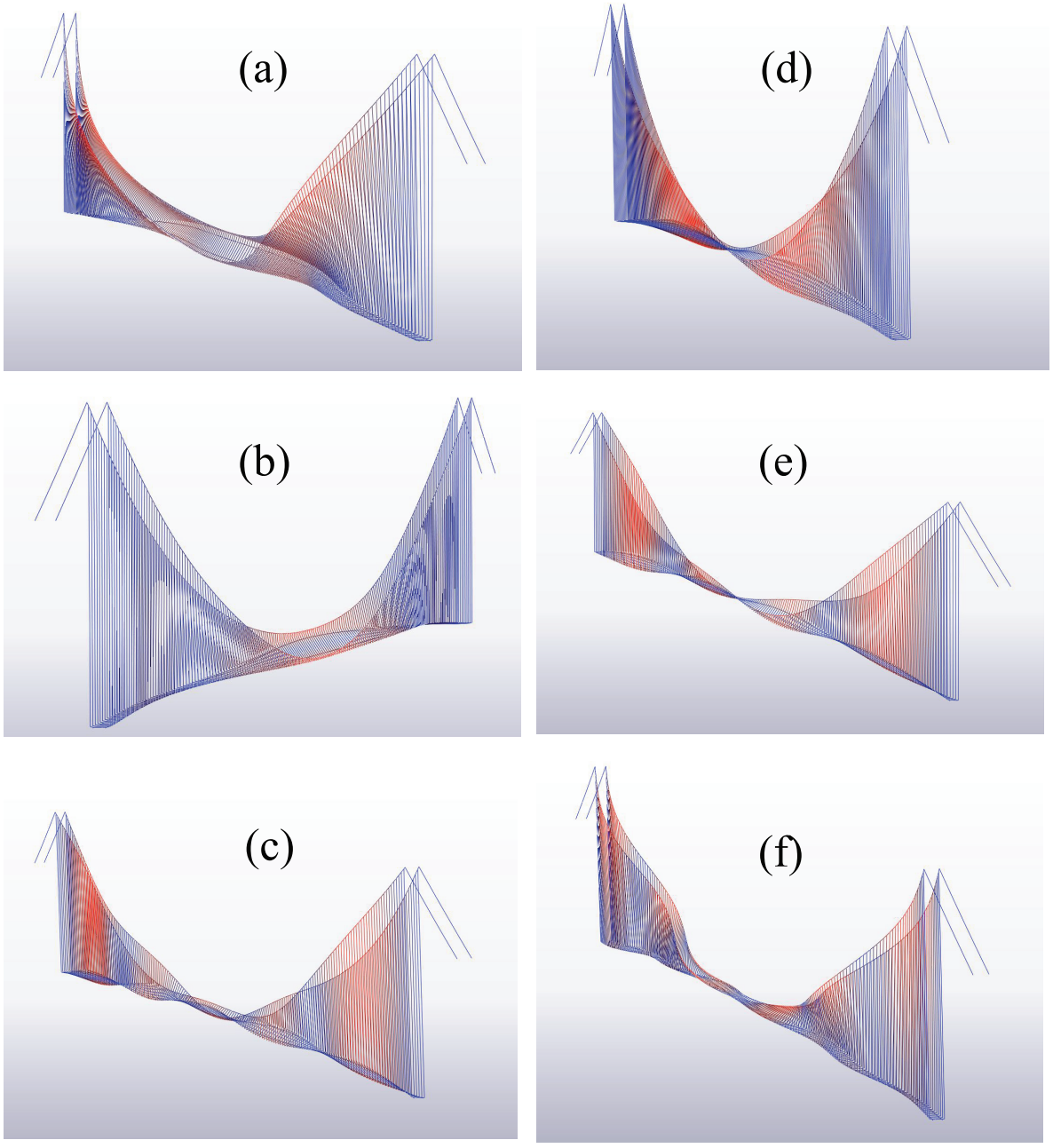

Figure D.3: Torsional symmetric and asymmetric modes: (a) 1stTS(11) (b) 2ndTS(14) (c) 3rdTS(31) (d) 1stTA(16) (e) 2ndTA(26) (f) 3rdTA(33). Red color indicates large amplitudes.

D.4 Section 2TFGP

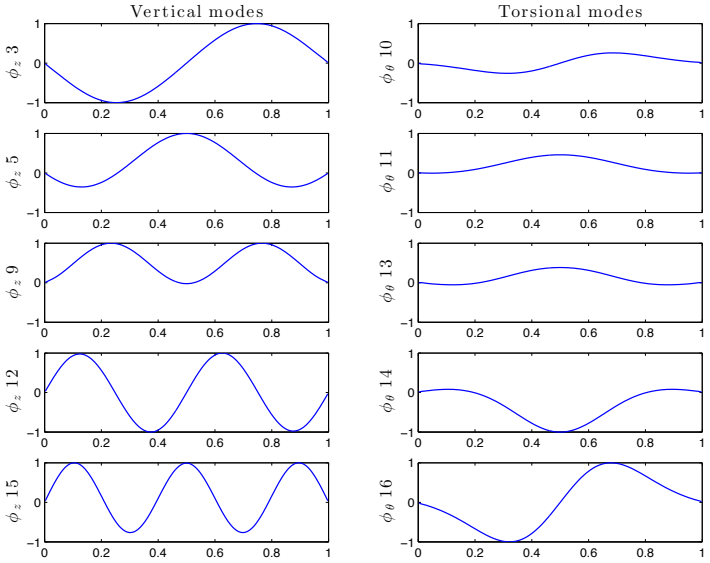

Figure D.4: First 5 vertical and torsional modes for cross section $2TFGP$.

D.5 Section BS15GV

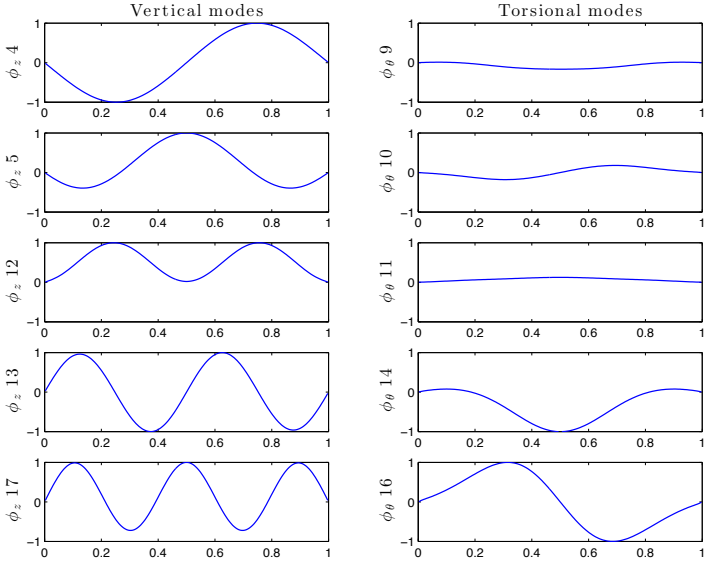

Figure D.5: First 5 vertical and torsional modes for cross section $BS15GV$.

D.6 Section BS20GV

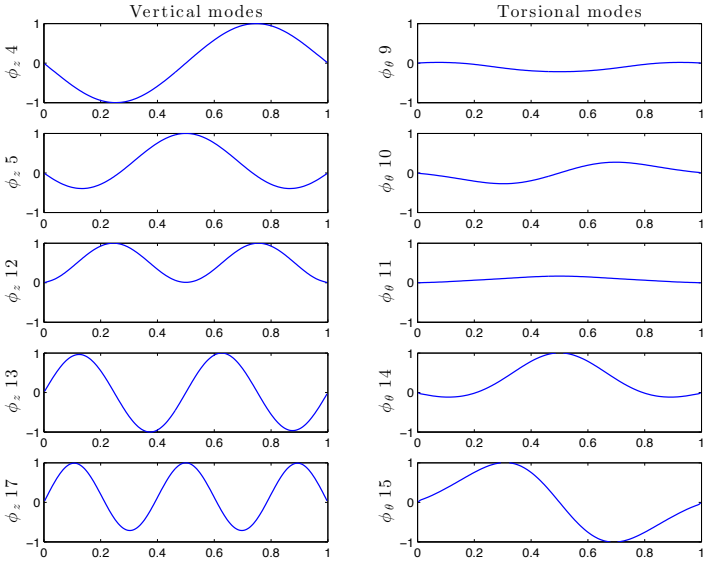

Figure D.6: First 5 vertical and torsional modes for cross section $BS20GV$.

D.7 Section BS30/BS30GV

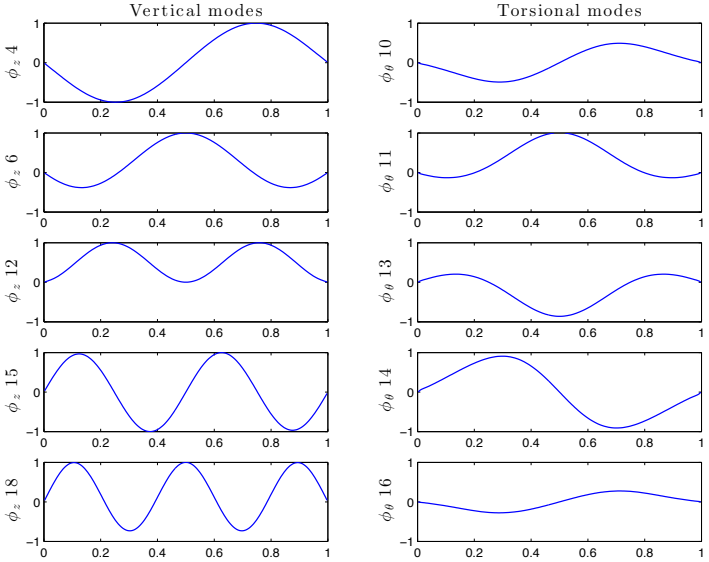

Figure D.7: First 5 vertical and torsional modes for cross section $BS30/BS30GV$.

Appendix E

MATLAB calculations

The *MATLAB* routines presented below uses the $*.dat$ files from *ABAQUS* as input files to a function that calculates the stability limit by solving the complex eigenvalue problem or the flutter equations.

E.1 Eigenvalue solution1

This *MATLAB* routine calculates the stability limit by calling the function *aerostab_Havard.m* provided by Øiseth [25] .

```
%% Description
% This script calculates the aeroelastic stability limit based on
% the general eigenvalue problem where several modes is chosen to described
% the problem. The script import the data from the *.dat file from ABAQUS
% by the function read_ABAQUS_dat.m created by Ole Andre Oiseth, and
% slightly modified by the author to include Cable displacements. The
% function aeroestab_Havard.m is used to perform the iteration process.
% Date: 10.06.2012  Haavard Maurset
clc
clear all
close all
%%
tic
VALGT=[];               % Modes to be included in the calculations
Nodes=185;              % Number of nodes along the girder where displacements
                        % are extracted
CNodes=187;             % Nodes along the cable for extracting displacements
L=3700;                 % Length of girder
%% Importing the data from ABAQUS
[Eigenvectors,Eigenvalues,CableEigenvec]...
    =read_ABAQUS_dat('filename.dat',Nodes,CNodes);
omegaomega=(Eigenvalues(VALGT,3));
Modalmass=Eigenvalues(VALGT,5);

%% Defining the modes and sort the table by the x-coordinate (along bridge)
Coordinates=Eigenvectors(:,2:4);
[~, b]=sort(Coordinates(:,1));

%% Calculating the modeintegrals
% Importing the modes from ABAQUS. The first component of a mode is the
% vertical, second horizontal(lateral) and the third torsional
% displacements

phiphi=zeros(3,size(Eigenvectors,1),length(omegaomega));
teller=1;%min(VALGT);
```

```
for n=1:length(omegaomega)
    phiphi(2,:,teller)=Eigenvectors(b,6,VALGT(n))';%n+min(VALGT)-1)';
    phiphi(1,:,teller)=Eigenvectors(b,7,VALGT(n))';%n+min(VALGT)-1)';
    phiphi(3,:,teller)=Eigenvectors(b,8,VALGT(n))';%n+min(VALGT)-1)';
    teller=teller+1;
end

moderInt=zeros(3,3,size(phiphi,3),size(phiphi,3));
for i=1:size(phiphi,3)
    for j=1:size(phiphi,3)
        for n=1:3
            for m=1:3
                integrand(1,:)=phiphi(n,:,i).*phiphi(m,:,j);
                moderInt(n,m,i,j)=trapz(integrand)*L/Nodes;
            end
        end
    end
end

%% Structural properties
M=diag(Modalmass);                                  % Modal mass matrix

% Natural frequencies and damping ratios
omega=omegaomega;
zeta=diag(0.05*ones(1,length(omegaomega)));
% Modal matrices
K=diag(omega).^2*M;                                 % Modal stiffness matrix
C=2.*zeta.*M*diag(omega);                           % Modal damping matrix
% Constants
ro=1.25;                                            % Density of air
B=7.5;                                              % Width of one girder


%% Eigenvalue solution
maxfit=200;                     % Max number of frequency and velocity
maxVit=1000;                    % iterations

V=1;                            % Initial mean wind velocity
dV=1;                           % Velocity increment

A=[];
[Vvec,imS,reS,VCR,OmegaCR]=aerostab_Havard(@aerodynamicderivativesBS15GV,M,
    C,K,omega,moderInt,ro,B,maxfit,maxVit,V,dV,A);



%% Results
figure(1)
set(gcf,'Name','Solution of the eigenvalue problem','Numbertitle','off')
plot(subplot(2,1,1),Vvec,imS,'o')
ylabel('$Im(\lambda_n)$','interpreter','latex')
title('Imaginary part of the eigenvalues (damped natural frequencies)',...
    'interpreter','latex')
```

```
88
89 plot(subplot(2,1,2),Vvec,reS,'o'),grid on
90 xlabel('V (m/s)','interpreter','latex')
91 ylabel('$Re(\lambda_n)$','interpreter','latex')
92 title('Real part of the eigenvalues (damping term,$\mu_n= -v_{n}\omega_n$)'
       ,'interpreter','latex')
93
94 disp(['The aeroelastic stability limit is ', num2str(VCR), ' m/s'])
95 disp(['The critical frequency is ' ,num2str(OmegaCR), ' rad/s'])
96
97 CPUtime=toc;
98 disp(['Computationaltime:',num2str(floor(CPUtime/60)),'min' ,...
99      num2str(floor((CPUtime/60-floor(CPUtime/60))*60)),'sek'])
```

E.2 Eigenvalue solution 2

This *MATLAB* routine calculates the stability limit by calling the function *aeroelasticstab.m* created by the author and given in Appendix E.4.1 . This routine has mainly been used for comparison with the *aerostab_Havard* function provided by Øiseth [25] since this routine is not fully developed. The routine has shown to give good results when few modes are included in the solution, but need further modifications.

```
1 %% Description
2 % This script calculates the aeroelastic stability limit based on
3 % the general eigenvalue problem where several modes is chosen to described
4 % the problem. The script import the data from the *.dat file from ABAQUS
5 % by the function read_ABAQUS_dat.m created by Ole Andre Oiseth, and
6 % slightly modified by the author to include cabledisplacements.
7 % The function aeroelasticstab.m is used to perform the iteration process.
8 % Date: 10.06.2012  Haavard Maurset
9 clc
10 clear all
11 close all
12 %%
13 tic
14 VALGT=[];              % Number of modes to be included
15 Nodes=185;             % Number of nodes along the girder where displacements
16                        % are extracted
17 CNodes=187;            % Nodes along the cable for extracting displacements
18 L=3700;                % Length of girder
19 %% Importing the data from ABAQUS
20 [Eigenvectors,Eigenvalues,CableEigenvec]...
21      =read_ABAQUS_dat('filename.dat',Nodes,CNodes);
22 omegaomega=(Eigenvalues(VALGT,3));
23 Modalmass=Eigenvalues(VALGT,5);
24
25 %% Defining the modes and sort the table by the x-coordinate (along bridge)
26 Coordinates=Eigenvectors(:,2:4);
27 [~, b]=sort(Coordinates(:,1));
28
29 %% Calculating the modeintegrals
30 % Importing the modes from ABAQUS. The first component of a mode is the
```

```
% horizontal(lateral), second vertical and the third torsional
% displacement

phiphi=zeros(3,size(Eigenvectors,1),length(omegaomega));
teller=1;%min(VALGT);
for n=1:length(omegaomega)
    phiphi(2,:,teller)=Eigenvectors(b,6,VALGT(n))';%n+min(VALGT)-1)';
    phiphi(1,:,teller)=Eigenvectors(b,7,VALGT(n))';%n+min(VALGT)-1)';
    phiphi(3,:,teller)=Eigenvectors(b,8,VALGT(n))';%n+min(VALGT)-1)';
    teller=teller+1;
end

moderInt=zeros(3,3,size(phiphi,3),size(phiphi,3));
for i=1:size(phiphi,3)
    for j=1:size(phiphi,3)
        for n=1:3
            for m=1:3
                integrand(1,:)=phiphi(n,:,i).*phiphi(m,:,j);
                moderInt(n,m,i,j)=trapz(integrand)*L/Nodes;
            end
        end
    end
end

%% Structural properties

M=diag(Modalmass);                              % Modal mass matrix

% Natural frequencies and damping ratios
omega0=diag(omegaomega);
zeta=diag(0.05*ones(1,length(omegaomega)));
% Modal matrices
K=omega0.^2*M;                                  % Modal stiffness matrix
C=2.*zeta.*M*omega0;                            % Modal damping matrix
% Constants
ro=1.25;                                        % Density of air
B=7.5;                                          % Width of one girder


%% Eigenvalue solution
maxfit=200;                 % Max number of frequency and velocity
maxVit=1000;                % iterations

V0=0;                       % Initial mean wind velocity
dV=1;                       % Velocity increment
omg0=1;                     % Initial assumption of critical frequency

[Omega,v_n,omega_n,omega,Vvec,ImLambda,ReLambda,Vcr,OmegaCr]=
    aeroelasticstab(@aerodynamicderivativesBS15GV,M,C,K,omg0,moderInt,ro,B,
    maxVit,maxfit,V0,dV,phiphi);


```

```
82 %% Results
83 figure(1)
84 set(gcf,'Name','Solution of the eigenvalue problem','Numbertitle','off')
85 plot(subplot(2,1,1),Vvec,ImLambda,'o')
86 ylabel('Im($\lambda_n$)','interpreter','latex')
87 title('Imaginary part of the eigenvalues (damped natural frequencies)','
       interpreter','latex')
88
89 plot(subplot(2,1,2),Vvec,ReLambda,'o'),grid on
90 xlabel('V (m/s)','interpreter','latex')
91 ylabel('Re($\lambda_n$)','interpreter','latex')
92 title('Real part of the eigenvalues (damping term,$\mu_n= -v_{n}\omega_n$)'
       ,'interpreter','latex')
93
94 disp(['The aeroelastic stability limit is ', num2str(Vcr), ' m/s'])
95 disp(['The critical frequency is ' ,num2str(OmegaCr), ' rad/s'])
96
97 CPUtime=toc;
```

E.3 Flutter stability

This *MATLAB* routine calculates the stability limit by calling the function *flutterstab.m* given in Appendixc E.4.2. The routine calculates the flutter stability limit when two modes, one vertical and one torsional, are assumed to give any instability.

```
1  %% Description
2  % This script calculates the flutter stability limit for coupling of one
3  % horizontal and one torsional mode by using the flutter equations. The
4  % function flutterstab.m is used to solve the equation system.
5  % Date: 10.06.2012    Haavard Maurset
6  clc
7  clear all
8  close all
9  %% Structural properties
10
11 % Modal equivalent distributed masses and MOI, choose one.
12 % M0=[25700 0 0;0 25700 0;0 0 2840000];                % 2TFGP
13 % M0=[22480 0 0;0 22480 0;0 0 2394200];                % BS15GV
14 % M0=[22580 0 0;0 22580 0;0 0 3433700];                % BS20GV
15 % M0=[23310 0 0;0 23310 0;0 0 6336000];                % BS30/BS30GV
16
17 m_z=M0(2,2);
18 m_theta=M0(3,3);
19
20 % Natural frequencies and damping ratiosf
21 omega_z=0.5;
22 omega_theta=2;
23 gamma=[1.4 1.5 1.6 1.8 2.0 2.2 2.4 3.0];
24 omega_theta2=gamma.*omega_z;                          % Frequency ratio vector
25 zeta=[0.005 0.005];                                   % zeta=[zeta_z zeta_theta]
26
27 % Constants
```

```
ro=1.25;                                                % Density of air
B='value here';                                         % Width of one girder

beta_z=ro*B^2/m_z;                                      % Coefficients used for
beta_theta=ro*B^4/m_theta;                              % simplifications in the
                                                        % Flutter equations

% Specifying the shapewise similarity of the two modes
psi='value her';
%% Flutter solution

Vred='value her';                       % Creating reduced velocity vector
RAD=1;

[ImaginaryRoot,RealRoot,ReRoot,OmgRedIm,OmgRedRe,Vcr,OmegaCr,VredCr,
    OmgRedCr,Vred_omega]=flutterstab(@aerodynamicderivativesBS15GV,
    omega_theta,omega_theta2,beta_z,beta_theta,zeta,psi,gamma,Vred,RAD,B);


%% Plotting the results
n=1;            % Defining for which frequency ratio results will be plotted
hold on
figure(1)
plot(Vred,OmgRedRe(n,:),'r',Vred,OmgRedIm(n,:),'--b')
set(legend('Real Root','Imaginary Root'),'interpreter','latex'), legend('
    boxoff')
%ylim([0.8*min(OmgRedIm(n,:)) 1.2*max(OmgRedIm(n,:))])
xlabel('Reduced velocity $\hat{V}=V/(B^*\omega_{CR})$','interpreter','latex
    ')
ylabel('Reduced frequency $\hat{\omega}_{CR}=\omega_{CR}/\omega_{\theta}$',
    'interpreter','latex')
%title('Development of the real and imaginary roots ','interpreter','latex
    ')
line([1 1]*VredCr(n),[0.8*min(OmgRedRe(n,:)) OmgRedCr(n)],'Color',[0 0.5
    0])
line([min(Vred) VredCr(n)],[1 1]*OmgRedCr(n),'Color',[0 0.5 0])

figure(2)
plot(gamma,Vred_omega,'-ob')
xlabel('Frequency ratio $\omega_{\theta}/\omega_z$','interpreter','latex')
ylabel('Reduced critical velocity $V_{Cr}/(B^*\omega_{\theta})$','
    interpreter','latex')

disp(['The flutter stability limit is ', num2str(Vcr(n)), ' m/s'])
disp(['The critical frequency is ' ,num2str(OmegaCr(n)), ' rad/s'])
```

E.4 MATLAB functions

E.4.1 MATLAB function: *aeroelasticstab.m*

```
%% Description
% This script calculates the aeroelastic stability in terms of the critical
% velocity and the critical frequency. The input to the function is given
% in the m-file eigenvalue.m
% Date: 10.06.2012    Haavard Maurset
%% Creating the function

function [Omega,v_n,omega_n,omega,Vvec,ImLambda,ReLambda,Vcr,OmegaCr]=
    aeroelasticstab(aerodynamicderivatives,M,C,K,omg0,moderInt,ro,B,maxVit,
    maxfit,V0,dV,phiphi)
%% Calculating properties
% I and zerosM are the matrices in matrix A given in Equation 4.42 in
% Section 4.4. IM is the identity matrix

I=diag(ones(1,size(phiphi,3)));
zerosM=zeros(size(phiphi,3),size(phiphi,3));
IM=diag(ones(1,2*size(phiphi,3)));
%% Eigenvalue solution with an iterative process
V(1)=V0;
                                        % Initial assumptions of frequency
vn_min=0.5;                             % and damping including aerodynamic
omega(1)=omg0;                          % damping as well as structural damping

i=2;                                    % Next step, starting with i=2

while vn_min > 0 && i <= maxVit
V(i)=V(i-1)+dV;                         % Increasing the velocity by increment
                                        % dV
Vvec(i-1)=V(i);                         % Creating velocity vector starting
                                        % at velocity V0+dV

Vred=V(i)/(omega(i-1)*B);

% Importing the aerodynamic derivatives
% AD=[P1* P2* P3* P4* P5* P6* H1* H2* H3* H4* H5* H6* A1* A2* A3* A4* A5*
    A6*]^T
AD=aerodynamicderivatives(Vred,omega(i-1));

% Aerodynamic damping matrix
Cae_h=ro*B^2/2*omega(i-1)*[AD(1) AD(5) B*AD(2);...
                           AD(11) AD(7) B*AD(8);...
                           B*AD(17) B*AD(13) B^2*AD(14)];

% Aerodynamic stiffness matrix
Kae_h=ro*B^2/2*omega(i-1)^2*[AD(4) AD(6) B*AD(3);...
                             AD(12) AD(10) B*AD(9);...
                             B*AD(18) B*AD(16) B^2*AD(15)];

```

```
46      Cae=zeros(size(phiphi,3),size(phiphi,3));
47      Kae=zeros(size(phiphi,3),size(phiphi,3));
48      for k=1:size(phiphi,3)
49          for l=1:size(phiphi,3)
50              for n=1:3
51                  for m=1:3
52  Cae(k,l)=Cae(k,l)+moderInt(n,m,k,l).*Cae_h(n,m);      % Modal aerodynamic
53  Kae(k,l)=Kae(k,l)+moderInt(n,m,k,l).*Kae_h(n,m);      % stiffness and damping
54                                                        % matrices
55                                                        % N_mod x N_mod
56                  end
57              end
58          end
59      end
60
61
62  A=[-M\(C-Cae) -M\(K-Kae);I zerosM];
63  lambda(:,i-1)=eig(A,IM);
64  ReLambda(:,i-1)=real(lambda(:,i-1));
65  ImLambda(:,i-1)=imag(lambda(:,i-1));
66  omega_n(:,i-1)=abs(lambda(:,i-1));
67  v_n(:,i-1)=-real(lambda(:,i-1))./omega_n(:,i-1);
68  [vn_min,Pos]=min(v_n(:,i-1));                 % Finding the mode with the lowest
69  Omega(1,i-1) = omega_n(Pos,i-1);              % damping value
70
71  j=1;                                          % Resetting iterativ counter after
72                                                % incrementing the velocity
73      % Frequency iterations
74      while abs(Omega(j,i-1)-omega(i-1)) > 0.0000001  && j <= maxfit
75          omega(i-1)=Omega(j,i-1);
76          j=j+1;                                % Update iteration counter
77
78          % Updating the aerodynamic derivatives for the new iterativ
79          % frequency, and also the aerodynamic matrices
80          AD=aerodynamicderivatives(Vred,omega(i-1));
81
82          Cae_h=ro*B^2/2*omega(i-1)*[AD(1) AD(5) B*AD(2);...
83                                     AD(11) AD(7) B*AD(8);...
84                                     B*AD(17) B*AD(13) B^2*AD(14)];
85
86          Kae_h=ro*B^2/2*omega(i-1)^2*[AD(4) AD(6) B*AD(3);...
87                                       AD(12) AD(10) B*AD(9);...
88                                       B*AD(18) B*AD(16) B^2*AD(15)];
89
90          Cae=zeros(size(phiphi,3),size(phiphi,3));
91          Kae=zeros(size(phiphi,3),size(phiphi,3));
92              for k=1:size(phiphi,3)
93                  for l=1:size(phiphi,3)
94                      for n=1:3
95                          for m=1:3
96                          Cae(k,l)=Cae(k,l)+moderInt(n,m,k,l).*Cae_h(n,m);
97                          Kae(k,l)=Kae(k,l)+moderInt(n,m,k,l).*Kae_h(n,m);
98
```

```
                        end
                    end
                end
            end

        A=[-M\(C-Cae) -M\(K-Kae);I zerosM];
        lambda(:,i-1)=eig(A,IM);
        ReLambda(:,i-1)=real(lambda(:,i-1));
        ImLambda(:,i-1)=imag(lambda(:,i-1));
        omega_n(:,i-1)=abs(lambda(:,i-1));
        v_n(:,i-1)=-real(lambda(:,i-1))./omega_n(:,i-1);
        [vn_min,Pos]=min(v_n(:,i-1));
        Omega(j,i-1) = omega_n(Pos,i-1);

    end
 % When the velocity becomes close to the critical the increment is reduced
 % to improve accuracy. Must be adjusted.
    if min(abs(ReLambda(:,i-1))) < 0.005 % && V(i) > 100
        dV=0.5*dV;
        if dV <=0.01
            dV=0.01;
        end
    end

    omega(i)=Omega(j,i-1);  % Updating the frequency vector in element i
    i=i+1;                  % Updating the velocity increment counter


end

Vcr=Vvec(length(Vvec));             % Defining the critical velocity and
OmegaCr=omega(length(omega));       % frequency as the values in the last
                                    % element of the vectors
```

E.4.2 MATLAB function: *flutterstab.m*

```
%% Description
% This script calculates the flutter stability in terms of the critical
% velocity and the critical frequency. The input to the function is given
% in the m-file fluttersolution.m
% Date: 10.06.2012    Haavard Maurset
%% Creating the function
function [ImaginaryRoot,RealRoot,ReRoot,OmgRedIm,OmgRedRe,Vcr,OmegaCr,
    VredCr,OmgRedCr,Vred_omega]=flutterstab(aerodynamicderivatives,
    omega_theta,omega_theta2,beta_z,beta_theta,zeta,psi,gamma,Vred,RAD,B)
%% Flutter solution
for j=1:length(gamma)
     for i = 1:length(Vred)

     AD=aerodynamicderivatives(Vred(1,i),RAD);

% CALCULATING THE REAL ROOTS OF THE FLUTTER EQUATIONS
R4=gamma(j)^2*(1 + 0.5*beta_z*AD(10) + 0.5*beta_theta*AD(15) + 0.25*beta_z*
    beta_theta*(AD(13)*AD(8)*psi - AD(14)*AD(7) + AD(15)*AD(10) - AD(16)*AD
    (9)*psi));
R3=gamma(j)*(zeta(2)*beta_z*gamma(j)*AD(7) + zeta(1)*beta_theta*AD(14));
R2=-(1 + gamma(j)^2 +4*gamma(j)*zeta(1)*zeta(2) + 0.5*beta_z*gamma(j)^2*AD
    (10) + 0.5*beta_theta*AD(15));
R1=0;
R0=1;

     Realpar=[R4 R3 R2 R1 R0];
     RealRoot(:,i,j)=real(roots(Realpar));
     RRoot=RealRoot(:,i,j);
     m=1;
          for k=1:4
               if RRoot(k,1)>=0
               ReRoot(m,1)=RRoot(k,1);
               m=m+1;
               end
          end
     OmgRedRe(j,i)=max(ReRoot(:,1)); %Must be changed dependent on the roots
     ReRoot=[];
     RRoot=[];

% CALCULATING THE IMAGINARY ROOTS OF THE FLUTTER EQUATIONS

I3=gamma(j)^2*((1/8)*beta_z*beta_theta*( AD(7)*AD(15) - AD(8)*AD(16)*psi -
    AD(9)*AD(13)*psi + AD(10)*AD(14)) + 0.25*(beta_z*AD(7) + beta_theta*AD
    (14)));
I2=-(zeta(1)*(0.5*beta_theta*AD(15) + gamma(j)) + zeta(2)*gamma(j)^2*(0.5*
    beta_z*AD(10) + 1) );
I1=-0.25*(beta_z*gamma(j)^2*AD(7) + beta_theta*AD(14));
I0=zeta(1)*gamma(j) + zeta(2);

     ImaginaryPar=[I3 I2 I1 I0];
     ImaginaryRoot(:,i,j)=real(roots(ImaginaryPar));
```

```
44      IRoot=ImaginaryRoot(:,i,j);
45      n=1;
46          for k=1:3
47              if IRoot(k,1)>=0
48              ImRoot(n,1)=IRoot(k,1);
49              n=n+1;
50              end
51          end
52      OmgRedIm(j,i)=max(ImRoot(:,1)); %Must be changed dependent on the roots
53      ImRoot=[];
54      IRoot=[];
55
56      end
57  end
58
59  %% Finding the critical values
60
61  % Calculating the difference in frequency for the real and imaginary
62  % solutions for the same reduced velocity
63  for m = 1:length(gamma)
64      for k = 1:length(Vred)
65      diffOmgRed(m,k)=abs(OmgRedRe(m,k)-OmgRedIm(m,k));
66      end
67
68      % Finding the positions where the difference is the smallest
69      [min_diffOmgRed,Pos]=min(diffOmgRed(m,:));
70
71      VredCr(m)=Vred(Pos);
72      OmgRedCr(m)=OmgRedRe(m,Pos);
73      OmegaCr(m)=OmgRedCr(m)*omega_theta2(m);
74      Vcr(m)=omega_theta2(m)*B*VredCr(m)*OmgRedCr(m);
75      Vred_omega(m)=VredCr(m)*OmgRedCr(m);
76
77  end
```

Bibliography

[1] Agar, T. J. A. (1988). The analysis of aerodynamic flutter of suspension bridges. *Computers & Structures*, 30(3):593–600.

[2] Agar, T. J. A. (1989). Aerodynamic flutter analysis of suspension bridges by a modal technique. *Engineering Structures*, 11(2):75–82.

[3] Bell, K., Bleie, O. V., and Wollebæk, L. (2000). *CrossX-User's manual*, version 1.0 edition.

[4] CEN (2005). *NS-EN 1991-1-4:2005+NA:2009: Eurocode 1: Actions on structures, Part 1-4: General actions/wind actions*. Standard Norway.

[5] Chen, A., He, X., and Xiang, H. (2002). Identification of 18 flutter derivatives of bridge decks. *Journal of Wind Engineering and Industrial Aerodynamics*, 90(12-15):2007–2022.

[6] Chopra, A. K. (2007). *Dynamics of structures : theory and applications to earthquake engineering*. Pearson Prentice Hall, Upper Saddle River, N.J.

[7] Darholm, T., Lundh, L., Ronnebrant, R., Karoumi, R., and Blaschko, M. (2007). *Technical book about the Svinesund Bridge*. Swedish Road Administration.

[8] Dyrbye, C. and Hansen, S. O. (1997). *Wind loads on structures*. Wiley, Chichester.

[9] Ge, Y. J. and Tanaka, H. (2000). Aerodynamic flutter analysis of cable-supported bridges by multi-mode and full-mode approaches. *Journal of Wind Engineering and Industrial Aerodynamics*, 86(2-3):123–153.

[10] Gimsing, N. J. (1997). *Cable supported bridges : concept and design*. Wiley, Chichester.

[11] Hansen, S. O., Lollesgaard, M., Jakobsen, J. B., and Hjorth-Hansen, E. (2005). Brusymfonien: Static and dynamic wind tunnel tests with a section model. Technical report, Svend Ole Hanse ApS.

[12] Hibbeler, R. C. and Fan, S. C. (2004). *Engineering mechanics : statics*. Prentice Hall, Singapore, si ed., 10th edition.

[13] Irvine, H. M. (1981). *Cable structures*. The MIT Press, Cambridge, Mass.

[14] Matsumoto, M., Shijo, R., Eguchi, A., Hikida, T., Tamaki, H., and Mizuno, K. (2004). On the flutter characteristics of separated two box girders. *Wind and Structures, An International Journal*, 7(4):281–291. Cited By (since 1996): 10 Export Date: 26 January 2012 Source: Scopus.

[15] Mishra, S. S., Kumar, K., and Krishna, P. (2008). Multimode flutter of long-span cable-stayed bridge based on 18 experimental aeroelastic derivatives. *Journal of Wind Engineering and Industrial Aerodynamics*, 96(1):83–102.

[16] Miyata, T. (2002). Significance of aero-elastic relationship in wind-resistant design of long-span bridges. *Journal of Wind Engineering and Industrial Aerodynamics*, 90(12-15):1479–1492.

[17] NPRA (2008a). *Handbook 017 Veg- og gateutforming*. The Norwegian Public Road Administration.

[18] NPRA (2008b). *Handbook 122 Kabler til hengebruer*. The Norwegian Public Road Administration.

[19] NPRA (2008c). Hardangerbrua-beregninger. Technical report, Teknologiavdelingen, The Norwegian Public Road Administration.

[20] NPRA (2009). *Handbook 185 Bruprosjektering*. The Norwegian Public Road Administration.

[21] NPRA (2011a). *Handbook 185 Bruprosjektering, Eurocode edition*. The Norwegian Public Road Administration.

[22] NPRA (2011b). Hardangerbrua-tegninger. Technical report, Bruseksjonen, The Norwegian Public Road Administration.

[23] NPRA (2011c). Mulighetsstudie: Kryssing av sognefjorden. Technical report, Prosjektavdelingen, The Norwegian Public Road Administration.

[24] Ogawa, K., Shimodoi, H., and Oryu, T. (2002). Aerodynamic characteristics of a 2-box girder section adaptable for a super-long span suspension bridge. *Journal of Wind Engineering and Industrial Aerodynamics*, 90(12-15):2033–2043. Cited By (since 1996): 5 Export Date: 20 January 2012 Source: Scopus.

[25] Øiseth, O. A. (2012). Solution of the complex eigenvalue problem.

[26] Øiseth, O. A., Rönnquist, A., and Sigbjörnsson, R. (2010). Simplified prediction of wind-induced response and stability limit of slender long-span suspension bridges, based on modified quasi-steady theory: A case study. *Journal of Wind Engineering and Industrial Aerodynamics*, 98(12):730–741.

[27] Øiseth, O. A. and Sigbjörnsson, R. (2011). An alternative analytical approach to prediction of flutter stability limits of cable supported bridges. *Journal of Sound and Vibration*, 330(12):2784–2800.

[28] Salvatori, L. and Borri, C. (2007). Frequency- and time-domain methods for the numerical modeling of full-bridge aeroelasticity. *Computers & Structures*, 85(11-14):675–687.

[29] Sarkar, P. P., Jones, N. P., and Scanlan, R. H. (1994). Identification of aeroelastic parameters of flexible bridges. *Journal of Engineering Mechanics*, 120(8):1718–1742. Cited By (since 1996): 75 Export Date: 20 January 2012 Source: Scopus.

[30] Sato, H., Hirahara, N., Fumoto, K., Hirano, S., and Kusuhara, S. (2002). Full aeroelastic model test of a super long-span bridge with slotted box girder. *Journal of Wind Engineering and Industrial Aerodynamics*, 90(12-15):2023–2032.

[31] Sato, H., Kusuhara, S., Ogi, K.-i., and Matsufuji, H. (2000). Aerodynamic characteristics of super long-span bridges with slotted box girder. *Journal of Wind Engineering and Industrial Aerodynamics*, 88(2-3):297–306.

[32] Selberg, A. and of Western Ontario. Faculty of Engineering Science, U. (1960). *Oscillation and Aerodynamic Stability of Suspension Bridges*. Civil engineering and building construction series. Norges Teknisk-Naturvitenskapelige Forskningsrad.

[33] Simiu, E. and Scanlan, R. H. (1996). *Wind effects on structures : fundamentals and applications to design*. Wiley, New York.

[34] SIMULIA (2009). *ABAQUS version 6.9 documentation*.

[35] Strømmen, E. N. (2010). *Theory of bridge aerodynamics*. Springer, Berlin.

[36] The MathWorks, I. (2010). Matlab.

[37] Toshio, M. (2002). Significance of aero,aeroelastic relationship in wind-resistant design of long-span bridges. *Journal of Wind Engineering and Industrial Aerodynamics*, 90(12-15):1479–1492.

[38] Wikipedia.org (2012). The hardanger bridge.